Growth, structure and lattice dynamics of epitaxial rare earth films and nanostructures

Zur Erlangung des akademischen Grades eines
DOKTORS DER NATURWISSENSCHAFTEN
von der Fakultät für Physik des
Karlsruher Instituts für Technologie (KIT)

genehmigte

DISSERTATION

von

Dipl. Phys. Olga Waller (geb. Bauder)
aus Oktjabrskij/Kasachstan

Tag der Mündlichen Prüfung: 06.02.2015

Referent: Prof. Dr. rer. nat. T. Baumbach
Korreferent: Prof. Dr. rer. nat. W. Wulfhekel
zusätzlicher Referent: Dr. rer. nat. S. Stankov

Contents

1. Motivation and introduction

Lattice dynamics is a branch of condensed matter physics that deals with periodic oscillations of atoms about their equilibrium positions in the crystal lattice. These atomic vibrations are described by quasiparticles (phonons) that are fully characterized by the phonon dispersion relations or by the spectrum of atomic vibrations that is the phonon density of states (DOS). Many thermodynamic and elastic properties of materials such as lattice specific heat, vibrational entropy, mean atomic displacement, speed of sound, mean force constants, Debye temperature, etc. are obtained from the phonon DOS. Knowledge of these quantities is not only important for a characterization of the materials, but it also can be used to verify various theoretical models used in solid state (*ab initio*) calculations. Due to the electron-phonon and phonon-phonon interactions the thermal lattice excitations play an important role in a variety of physical phenomena in condensed matter such as thermoelectricity, superconductivity, propagation of sound and heat and many others.

The downscaling of the characteristic material dimensions to the nano- and sub-nanometer length scale leads to drastic changes of almost all physical properties in comparison to the bulk counterparts. In particular, the spatial confinement of atomic vibrations has a pronounced influence on the phonon dispersion relations in thin and ultra-thin films, multilayers and nanostructures, modifying the phonon DOS, and consequently all relevant thermo-elastic properties as well as electron-phonon and phonon-phonon interactions. Therefore, nanostructuring of materials and their suitable combination could be a powerful tool to control the propagation of heat and sound, manipulate and even tailor these properties by *phonon engineering* [1]. For such applications, however, a comprehensive understanding of the dependence of the phonon dispersion relations and/or the phonon DOS on the nanomaterials sizes, their shape, oxidation state, epitaxial strain, the presence of defects, amount of grain boundaries and interfaces is indispensable.

The determination of the complete lattice dynamics of a material requires a precise measurement of either the phonon dispersion relations or the phonon DOS and their comparison with results derived from theoretical models, or from *first-principles* calculations. However, the measurement of phonon excitations in nanoscale materials such as ultra-thin films and nanostructures is among the most challenging tasks in the experimental condensed matter physics because neither inelastic neutron scattering nor inelastic X-ray scattering are applicable to samples on the nano- and sub-nanometer length scale. The experiments are additionally complicated by the need for dedicated sample environments that often require ultra-high vacuum

conditions. In general, surface phonon dispersion curves are probed by helium atom scattering or electron energy loss spectroscopy. Partial information about the surface atomic vibrations can also be obtained by inelastic light scattering methods such as Brillouin and surface enhanced Raman scattering, as well as by surface enhanced infrared spectroscopy. However, the limited penetration depth of the former and the finite momentum transfer of the latter are severe limitations prohibiting the determination of the full lattice dynamics. The development of 3^{rd} generation synchrotron radiation sources made phonon spectroscopy on nanostructures and thin layers *in situ*, i.e., under ultra-high vacuum, feasible using nuclear inelastic scattering (NIS) [2]. This experimental technique is based on the Mössbauer effect, which is the resonant absorption/emission of gamma quanta from the nuclei of isotopes of certain elements. This method provides direct access to the partial, direction projected phonon DOS. Partial means that only atoms of the resonant isotope contribute to the measured signal and direction projected implies that the contributions of various branches are weighted by the projection of the phonon polarization vector to the incident direction of the photons. In addition, applied at grazing-incidence geometry, it is sensitive to phonons with polarization vectors oriented in the plane of the investigated surface. Thanks to the resonant nature of the Mössbauer effect, nuclear inelastic scattering is sensitive to very small amounts of materials, while the high penetration depth of X-rays ensures the bulk sensitivity of the method. Therefore, this method is particularly suitable for the investigation of samples with dimensions on the nano- and sub-nanometer length scale.

The rare earth elements (lanthanides) include 15 metals with atomic numbers from 57 to 71, which are characterized by the filling up of the $4f$ electron shell. Scandium ($Z = 21$) and yttrium ($Z = 39$) are often considered as part of the lanthanide family because of their very similar physical and chemical properties.
Technological applications of rare earth metals are continuously increasing, spanning fields such as medicine (high magnetic field sources for medical imaging devices, robot-assisted surgeries, cochlear implants, cancer-treating drugs, etc.), clean energy sources (wind turbines, electric car batteries, LED lighting and fiber optics, magnetic refrigeration, etc.), nanoelectronics (color displays, in-ear headphones, microphones, loudspeakers, optical fibers, smartphones, tablet computers, etc.), automobile industry (electric motors and batteries of hybrid cars, catalytic converters) and nuclear power reactors (thermal neutron absorbers). The wide field of applications requires a comprehensive investigation and fundamental understanding of all physical and chemical properties of the lanthanides.

The lattice dynamics of most elements has been systematically investigated after the establishing of inelastic neutron scattering as a standard tool for probing the phonon dispersion relations in solids. In such a way the lattice dynamics of the lanthanides La [3, 4, 5, 6], Ce [7, 8], Tb [9] and Ho [10] has been determined. The large absorption cross section for thermal neutrons exhibited by some of the lanthanides (Eu, Sm, Gd) prohibited their systematic study by this technique. Therefore, the phonon properties of some of the bulk lanthanides remain unknown

until today. Additional experimental difficulties arise from the limited availability of single crystals with high purity and quality and from the tendency of most lanthanides to oxidize once exposed to air. A very successful approach to overcome these obstacles is to grow thick high-quality single crystalline films by molecular beam epitaxy and to perform the experiments *in situ*, i.e., under ultra-high vacuum conditions.

The comprehensive understanding of the lattice dynamics of materials requires a comparison of experimental results with results from theoretical models, or *first-principles* calculations. The calculations of phonon dispersion relations are challenging due to the difficulty of a correct treatment of the $4f$ electrons, exhibiting strong correlations, complex magnetic ordering and, in some cases, large spin-orbit interactions. The lattice dynamics of La [11], Gd [12], Dy [13], and Er [14] has been theoretically investigated with semiempirical models. Attempts for systematic studies of the rare earths have also been made [15, 16] resulting, however, in a poor agreement with the available experimental data.

A combination of *in situ* NIS on ^{151}Eu and *first-principles* calculations has been successfully employed for the complete determination of the lattice dynamics and thermo-elastic properties of metallic europium [17]. The agreement between experiment and calculations demonstrated that this is a successful approach for the determination of the lattices dynamics of bulk lanthanides.

The aim of this thesis is the determination of the lattice dynamics and the thermo-elastic properties of bulk-like rare earth elements Sm and Nd, which were partially unknown up to now, and the investigation of the changes of the lattice dynamics in epitaxial nanostructures in comparison to the bulk material.
For the investigation of the bulk like properties thick (500 nm - 1000 nm) single crystalline films of Nd and Sm should be grown and characterized. Sm should be investigated in its native $9R$ structure (*Sm-type*) and in the *dhcp* lattice, characteristic for light lanthanides. The lattice dynamics should be determined by *in situ* nuclear inelastic scattering on ^{149}Sm, inelastic X-ray scattering and *first-principles* calculations (calculations performed by a collaboration partner).
Eu should be utilized for the investigation of the lattice dynamics of rare earth nanostructures because it was reported to form different nanostructures when deposited on transition metal surfaces (Nb [18], Ta [19], V [20], W [21]). ^{151}Eu is a Mössbauer active isotope that can be investigated with NIS, a method capable of the determination of the phonon spectrum of samples with material coverages in the nano and subnanometer length scale. The growth procedures for Eu nanoislands, 2D films and wire-like structures should be developed and applied, and the structures characterized. The changes in the lattice dynamics of nanostructures in comparison to the reported [17] bulk-like properties should be investigated and understood.

The thesis is structured as follows: after the general introduction to the topic in this

chapter, the theoretical description of the lattice dynamics is outlined in chapter 2. Nuclear resonant scattering methods used for the investigation of lattice dynamics and hyperfine interactions are based on the Mössbauer effect. Therefore, a basic description of this effect as well as of inelastic X-ray scattering is given in the same chapter. The instrumentation that is essential for experiments with these methods is also briefly outlined. Chapter 3 describes the method used for the sample growth and *in situ* laboratory methods used for characterization.
The experimental results are grouped in chapters 4 and 5. The lattice dynamics and thermo-elastic properties of thick rare earth films ($9R$ samarium, *dhcp* samarium and *dhcp* neodymium) are described in chapter 4. The growth conditions are presented for each material prior to the results on the lattice dynamics. The first part of chapter 5 contains the results from the growth and structural investigation of Eu films and nanostructures (nanoislands and wire-like structures). The second part contains the determination of the lattice dynamics and thermodynamic properties of *fcc* Eu islands and wire-like Eu structures.
A complete and comprehensive determination of the lattice dynamics is not possible without complementing/comparing the experiment with theory. Most of the experimental results presented in this thesis are compared and interpreted with the help of the results from *first-principles* calculations performed by Dr. habil. Przemysław Piekarz from the Institute of Nuclear Physics, Polish Academy of Sciences, Krakow, Poland.

Part I.

Background: Theory and experimental methods

2. Theoretical background and experimental methods

This chapter gives an introduction into the lattice dynamics of solids and methods for its determination used in this thesis. The Mössbauer effect based X-ray scattering techniques nuclear forward scattering and nuclear inelastic scattering are introduced. The former is used for the investigation of electronic and magnetic properties, the latter for the determination of the phonon DOS. The main advantage of this methods among the others is the possibility to investigate nanostructures consisting of a sub-monolayer coverage of the studied material. The phonon dispersion relations of bulk-like epitaxial films were mapped by inelastic X-ray scattering, therefore this method is also described.

2.1. Lattice dynamics

Lattice dynamics describes properties of solids that arise from the motion of atoms around their equilibrium position. The investigation of the lattice dynamics is of major importance in solid state physics for the determination of material properties.

In the adiabatic approximation [22], the motion of the nuclei and the valence electrons are treated separately. In this approximation, the wave function $\Psi(\vec{r},\vec{R})$ of a crystal consisting of nuclei and electrons, is expressed as [22]:

$$\Psi(\vec{r},\vec{R}) = \psi(\vec{r},\vec{R})\chi(\vec{R}). \tag{2.1}$$

$\psi(\vec{r},\vec{R})$ is the wave function of the entire system of electrons at positions of nuclei $\vec{R}$ and electrons $\vec{r}$. $\chi(\vec{R})$ is the wave function of the entire system of nuclei. The interaction term between the electron and the nucleus in the Hamiltonian of the whole system is neglected [23], reducing the Schrödinger equation of the nuclei to:

$$\left[\underbrace{\sum_l \frac{-\hbar^2}{2M_l}\nabla^2_{R_l}}_{T(\vec{R}_l)} + V(\vec{R}_l)\right]\chi(\vec{R}_l) = \epsilon\chi(\vec{R}_l), \tag{2.2}$$

with M_l the mass of the nuclei at the position $\vec{l}$, the reduced Planck constant $\hbar$ and the Laplace operator ∇^2, ϵ is the energy corresponding to the Hamiltonian. The actual position of an atom is defined by $\vec{R}_l = \vec{l} + \vec{u}(\vec{l})$ with $\vec{l}$ the equilibrium position

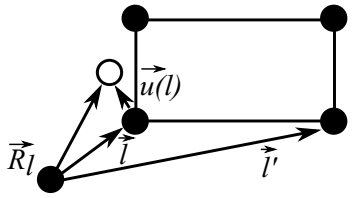

Figure 2.1.: The lth atom deviates from the equilibrium position by $\vec{u}(\vec{l})$, having the actual position $\vec{R}_l = \vec{l} + \vec{u}(\vec{l})$ [24].

of atom l and $\vec{u}(\vec{l})$ the displacement or deviation from $\vec{l}$ (see Fig.2.1).

The bracket denotes the Hamilton operator with contributions from terms corresponding to the kinetic energy $T(\vec{R}_l)$ and an effective potential energy as a function of the instantaneous positions of all atoms, $V(\vec{R}_l) = V_{nn}(\vec{R}_l) + E_e(\vec{R}_l)$, with $V_{nn}(\vec{R}_l)$ the inter atomic potential and $E_e(\vec{R}_l)$ the mean contribution from the electrons. It is possible to calculate Eqn.(2.2) if a phenomenological potential is assumed for $V(\vec{R}_l)$ [25, 26, 27, 28].

The first term in the Hamiltonian (Eqn.(2.2)) $T(\vec{R}_l)$ is the total kinetic energy of the crystal and can be expressed as a sum over the product of the mass of the atom M_l at the position $\vec{l}$ and the time derivative of the components $\alpha = x, y, z$ of the displacements $u_\alpha(\vec{l})$ from the equilibrium positions:

$$T(\vec{R}_l) = \frac{1}{2} \sum_{\alpha,l} M \dot{u}_\alpha^2(\vec{l}). \tag{2.3}$$

Both terms, $T(\vec{R}_l)$ and $V(\vec{R}_l)$, depend only on the position of the atoms, i.e., the displacement out of the equilibrium positions.

If the displacement $\vec{u}(\vec{l})$ is small, $V(\vec{R}_l)$ can be approximated by Tailor series around $\vec{u}(\vec{l}) = 0$ (written in components $(\alpha, \beta = x, y, z)$ of $\vec{u}(\vec{l})$):

$$V(\vec{R}_l) = V_0 + \sum_{\alpha,l} \underbrace{\frac{\delta V}{\delta u_\alpha(\vec{l})}}_{\Phi_\alpha(\vec{l})} u_\alpha(\vec{l}) + \frac{1}{2} \sum_{\alpha,l} \sum_{\beta,l'} \underbrace{\frac{\delta^2 V}{\delta u_\alpha(\vec{l}) \delta u_\beta(\vec{l'})}}_{\Phi_{\alpha\beta}(\vec{l},\vec{l'})} u_\beta(\vec{l'}) u_\alpha(\vec{l}) + \dots \quad . \tag{2.4}$$

The sum runs over all atoms l, l'. The zero point of the potential energy V_0 is chosen to be at the equilibrium position where the net forces $(\Phi_\alpha(\vec{l}))$ are zero and thus, the first and the second term on the right side in Eqn.(2.4) are zero.

In the harmonic approximation, only the quadratic term is taken into account (Eqn.(2.4)). Within this approximation, the net forces $(-\delta V/\delta u_\alpha(\vec{l}))$ are expressed as a linear function of the displacement $u_\beta(\vec{l'})$:

$$F_\alpha(\vec{l}) = -\frac{\delta V}{\delta u_\alpha(\vec{l})} \quad \Longrightarrow \quad M \ddot{u}_\alpha(\vec{l}) = -\sum_{\beta,l'} \Phi_{\alpha\beta}(\vec{l},\vec{l'}) u_\beta(\vec{l'}). \tag{2.5}$$

The factors $\Phi_{\alpha\beta}(\vec{l},\vec{l'})$ are called atomic force constants. With the knowledge of these constants, the equation of motion for the lth atom in the direction $(\alpha, \beta = xyz)$ is

expressed, by the right part of Eqn.(2.5). Thus, the equation of motion includes the coupling of atom l at position α with other atoms l' at positions β. The force constants $\Phi_{\alpha\beta}(\vec{l},\vec{l'})$, represent forces between two atoms and exhibit the following properties [24]:

- $\Phi_{\alpha\beta}(\bar{l},\vec{l'}) = \Phi_{\beta\alpha}(\vec{l'},\vec{l})$: Independence of the order of the derivatives.
- $\sum_{\vec{l'}} \Phi_{\alpha\beta}(\vec{l},\vec{l'}) = 0$: Sum of all force constants originating from atoms l' acting on the atom l are zero.
- Dependence on only the relative position between the atoms l and l'.
- A 3×3 matrix, using the symmetry properties in crystals.

The expression for the kinetic energy including the force constant and the potential energy $V(\vec{R}_l)$ results in coupled equations of motion. A solution for the movement of atoms can be derived if the Cartesian coordinates are transformed into the so-called *normal* coordinates resulting in $3N$ decoupled equations of motion for N atoms. The *normal* mode vibration is not a vibration of a single atom but a collective vibration of all atoms. The collective vibration forms a lattice wave, that depends only on the phase between the atoms. The wave is expressed by a wavevector $\vec{k}$, the position vector $\vec{l}$ of the atom l and the α-component of the polarization vector $e_\alpha(\vec{k}_j)$ describing the direction of the lattice wave with the branch index j at time t. A general expression for the α-component of the displacement of atoms is written as [29]:

$$u_\alpha(\vec{l}) = \frac{1}{\sqrt{NM}} \sum_{j,\vec{k}_j} A(\vec{k}_j) e_\alpha(\vec{k}_j) e^{i[\vec{k}\vec{l} - \omega_j(\vec{k})t]}, \tag{2.6}$$

with N, the number of atoms and M, their mass. $A(\vec{k}_j)$ is the vibrational amplitude depending on the average energy of mode $\vec{k}_j$. The wave, traveling through the crystal displaces neighboring atoms, that differ by a phase factor $\vec{k} \cdot \vec{l}$. Every atom will vibrate with the same frequency ω_j of the branch with the index j. Using the general expression Eqn.(2.6) for the solution of the equation of motion, the eigenvalue equation for every mode $\vec{k}_j$ is obtained [24]:

$$\omega_j^2(\vec{k}) e_\alpha(\vec{k}_j) = \sum_\beta \underbrace{\frac{1}{M} \sum_{\vec{l'}-\vec{l}} \Phi_{\alpha\beta}(0,\vec{l'}-\vec{l}) e^{i\vec{k}\cdot(\vec{l'}-\vec{l})}}_{D_{\alpha\beta}(\vec{k})} e_\beta(\vec{k}_j). \tag{2.7}$$

The sum on the right side of the equation runs over all spatial components β. The force constants matrix $\Phi_{\alpha\beta}(0,\vec{l'}-\vec{l})$ exhibits the above mentioned properties and is therefore only dependent on the position vector $\vec{L} = \vec{l'} - \vec{l}$ from atom l to the atom l'. The 3×3 matrix $D_{\alpha\beta}(\vec{k})$ is the so-called *dynamical matrix*. It is the Fourier-transformed expression of the force constants matrix containing all information necessary for the description of the elastic properties of the crystal [30].

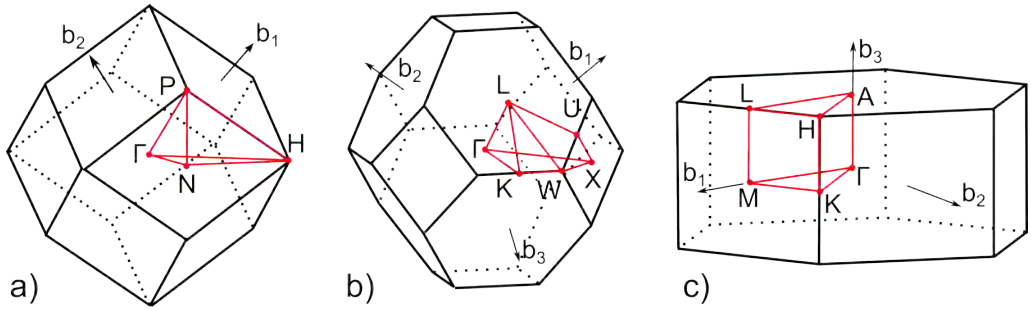

Figure 2.2.: First Brillouin zones of a) *bcc*, b) *fcc* and c) *hcp* lattices. The dispersions relation are usually shown between the main symmetry points $(\Gamma, P, N, H, \ldots)$. The vectors $\vec{b}_i$ are unit vectors [31].

The eigenvalues determine the relation between the frequency ω_j and the wavevector $\vec{k}$ and are calculated by the solution of [24]:

$$det\left\{\omega_j^2(\vec{k})\delta_{\alpha\beta} - D_{\alpha\beta}(\vec{k})\right\} = 0. \tag{2.8}$$

In a one-atomic Bravais lattice, for every wavevector $\vec{k}$ only 3 solutions for each spatial direction have to be solved. Solving Eqn.(2.8), the relation between the frequency $\omega_j(\vec{k})$ and the wavevector $\vec{k}$ is derived. This relation is called *dispersion relation*. The branches $j = 1, 2, 3$ are the three spatial orientations with different dispersion relations. When calculating Eqn.(2.8), it turns out, that ω is a continuous function within one branch j. For a lattice with N atoms per unit cell the dynamical matrix has the dimensions $3N \times 3N$ and each wavevector $\vec{k}$ has $3N$ eigenvalues $\omega_j^2(\vec{k})$ with $j = 1, 2 \ldots, 3N$.
The wavevector $\vec{k}$ appears only in the exponent of the dynamical matrix (Eqn.(2.7)). Thus, for the calculation of the dispersion relations it is sufficient to calculate the dynamical matrix in directions of high symmetry in the first Brillouin zone. The dispersion relations are plotted in between the high symmetry points of the first Brillouin zone in units of reciprocal lattice vectors.

Rare earth metals investigated within the scope of this thesis exhibit either the body centered cubic (*bcc*) (Eu), face centered cubic (*fcc*) (Eu) or hexagonal close packed (*dhcp*) (Sm, Nd) structures. The Brillouin zones for the *bcc*, *fcc* and *hcp* crystals are shown in Fig .2.2. Usually, the dispersion relation are shown between the points of high symmetry $(\Gamma, P, N, H, \ldots)$.

2.1.1. Phonons

Due to the description of the vibrations by normal modes, collective lattice vibrations are treated as independent oscillators. The energy of the harmonic oscillator with the frequency ω and n the number of states, is quantized:

$$E_n = \hbar\omega\left(n + \frac{1}{2}\right), \quad \text{with} \quad n = 0, 1 \ldots \quad . \tag{2.9}$$

The same applies for the energy of the vibrations of the normal modes with the frequency ω_s and the phonon number n. Phonons are the energy quanta $E = \hbar\omega$ of the collective motion of the atoms and are therefore quasi particles without mass but with a quasi momentum. The minimal energy exchange with the lattice corresponds to a transition that changes n by one and is therefore $\hbar\omega$. Due to the long wavelength of the phonons in comparison to the lattice constant, they are considered to be nonlocalized excitations. For a vibration with frequency ω, n is the number of phonons. The average phonon number $\left\langle n(\vec{k}_j)\right\rangle$ at thermal equilibrium is given by the Bose-Einstein statistics. Thus, the average energy of a phonon mode j at temperature T is [24]:

$$\left\langle E(\omega_j(\vec{k}), T)\right\rangle = \hbar\omega_j(\vec{k}) \left[\frac{1}{\exp[\hbar\omega_j(\vec{k})\beta] - 1} + \frac{1}{2}\right], \tag{2.10}$$

with $\beta = 1/k_B T$ and k_B the Boltzmann constant. At $T = 0\,\mathrm{K}$ the zero point energy is $\left\langle E(\omega_j(\vec{k}), 0)\right\rangle = \frac{1}{2}\hbar\omega_j(\vec{k})$.
Knowing the average energy of a phonon mode, the total energy of the vibrations can be derived.

Phonon density of states

The values of $\omega_j(\vec{k})$ are treated as continuous. The temperature dependent expression of the total energy can be written as an integral over ω [24]:

$$\langle E(T)\rangle = \sum_{\vec{k},j} \frac{\hbar\omega_j(\vec{k})}{\exp[\hbar\omega_j(\vec{k})\beta] - 1} = 3N \int_0^{\omega_m} \frac{\hbar\omega}{\exp[\hbar\omega\beta] - 1} g(\omega) d\omega, \tag{2.11}$$

with N the number of atoms and $g(\omega)$ the normalized frequency distribution function or the phonon density of states (phonon DOS). It describes the probability of lattice vibrations having a specific frequency in the interval ω and $\omega + d\omega$, with ω_m being the maximal frequency. $g(\omega)$ satisfies the normalization condition [24]:

$$\int_0^{\omega_m} g(\omega) d\omega = 1\ . \tag{2.12}$$

Knowing the dispersion relations in the first Brillouin zone $\omega_j(\vec{k})$ for all $\vec{k}$, the phonon DOS is calculated by:

$$g(\omega) = \frac{1}{3N} \sum_{j}^{3} \sum_{\vec{k}}^{N} \delta(\omega - \omega_j(\vec{k})). \tag{2.13}$$

Fig. 2.3 shows the dispersion relation and the phonon DOS of a one-dimensional chain consisting of two atoms with different masses ($M_1 < M_2$) [24]. The frequency ω is plotted over the wavevector $\vec{k}$ within the first Brillouin zone ($\frac{-\pi}{a} - \frac{\pi}{a}$). For every $\vec{k}$ there are 2 values of ω and $2N$ waves in total. The upper branch is the the optical branch, while the lower are the acoustic branches. All of them propagate

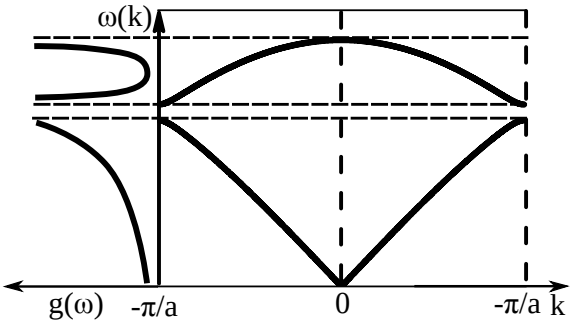

Figure 2.3.: Dispersion curves of a one-dimensional diatomic chain within the first Brillouin zone between $\frac{-\pi}{a}$ and $\frac{\pi}{a}$. The phonon frequency distribution (phonon DOS $g(\omega)$) is the sum of the states in an interval of ω and $\omega + \Delta\omega$.

along the direction of the atomic vibration and are therefore *longitudinal*. In a three dimensional crystal the propagation of the wave perpendicular to the atomic vibrations is possible. This is referred to as *transverse wave*. The sum over the allowed frequencies in the interval ω and $\omega + d\omega$ is plotted on the left graph of Fig. 2.3 and corresponds to the phonon DOS.

In the case of two different atom species in the unit cell, the partial phonon DOS $g_d(\omega)$ gives the spectral distribution of each of the atomic species d. The total density of states is the sum of the partial phonon DOS of all species of atoms in the unit cell [32]:

$$g(\omega) = \sum_d g_d(\omega). \tag{2.14}$$

This is of crucial importance for the methods based on nuclear inelastic scattering on Mössbauer isotopes because there only the isotope specific partial phonon DOS is obtained.

The knowledge of the phonon DOS is necessary for the determination of the total vibrational energy and therefore of all thermodynamic and elastic properties. The lattice dynamics is fully determined if the phonon dispersion relations or the phonon DOS is known.

2.1.2. Elastic and thermodynamic properties

From the classical thermodynamics it is known, that the partition function connects the microscopic properties of a system to the macroscopic thermodynamic quantities.
The *partition function* defines the occupation probabilities that are partitioned among the states of different energy. All thermodynamic quantities can be calculated from the partition function [32].
In a harmonic solid with N atoms and $3N$ independent oscillators, the partition function is calculated by the product of the partition functions of the individual

oscillators [32]:

$$Z_N = \prod_i^{3N} \frac{e^{-\beta E_i/2}}{1 - e^{-\beta E_i}}. \tag{2.15}$$

The frequencies are treated as continuous functions within one phonon branch. Expressed by the phonon DOS, the partition function is written as an integral over the energy:

$$\ln Z_N = -3N \int \ln\left(2 \sinh \frac{\beta E}{2}\right) g(E) dE. \tag{2.16}$$

Therefore, from the phonon DOS $g(E)$ properties of the solid can be calculated, for example:
The **vibrational internal energy** per atom [33]:

$$U = -\frac{\partial \ln Z_N}{\partial \beta} = \frac{3}{2} \int E \coth \frac{\beta E}{2} g(E) dE. \tag{2.17}$$

The **Helmholtz free energy** per atom [33], defined as $F = -k_B T \ln Z_N$:

$$F_{vib} = 3k_B T \int \ln\left(2 \sinh \frac{\beta E}{2}\right) g(E) dE. \tag{2.18}$$

Vibrational entropy
In classical thermodynamics the entropy describes the energetic interaction of a system with its environment [32]. For example, the entropy defines if nanoparticles are stable and how thermodynamic properties are changing in comparison with the corresponding bulk materials. Surfaces and interfaces are characterized with an enhanced vibrational internal energy [32], but certain configurations of atoms or structural excitations are able to stabilize the particle, reducing the free energy by reducing its vibrational entropy [32]. Thus, the vibrational entropy is an important factor for the stability of nanocrystalline materials.
The **vibrational entropy** is given by $S_{vib} = \delta F_{vib}/\delta T$ [33] leading to the expression:

$$S_{vib} = k_B \beta U + \ln Z \tag{2.19}$$

with U defined by Eqn.(2.17). The temperature and volume dependence of the entropy is given by [32]:

$$\frac{dS(T,V)}{dT} = \left(\frac{\partial S}{\partial T}\right)_{V=const.} + \left(\frac{\partial S}{\partial V}\right)_{T=const.} \frac{dV}{dT}. \tag{2.20}$$

Within the harmonic approximation, the contributions to the entropy are described by the first term on the right side of Eqn.(2.20), because the volume is not changing with the temperature. Therefore, within the adiabatic approximation, phonons do not change their frequency with temperature or volume. The temperature dependence arises from the occupancy factors of the phonons. The quasiharmonic contribution to the entropy depends on the volume (second term in the right side of Eqn.(2.20)) and anharmonic effects can contribute to both terms of the entropy [32].

Lattice specific heat

The specific heat of a solid defines its temperature change if a certain amount of heat energy is transferred. The deviation of the lattice specific heat of nanostructures compared to the bulk elements is of fundamental interest, for example, for the miniaturization of nanoelectronic devices.

The total specific heat of a solid contains contributions from the lattice vibrations (lattice specific heat) and the thermal motion of the electrons (electronic specific heat). At constant volume (V), the lattice specific heat of a solid is derived from the temperature derivative of the vibrational internal energy [24]:

$$C_V = \left(\frac{\delta U}{\delta T}\right)_V . \tag{2.21}$$

Applying Eqn.(2.17), the lattice specific heat per atom is:

$$C_V = 3k_B \int \left[\frac{\beta E}{2\sinh(\beta E/2)}\right]^2 g(E)\,dE. \tag{2.22}$$

In accordance with the equipartition principle for each harmonic motion from the classical thermodynamics, C_V approaches $3Nk_B$ at high temperatures [32].

Debye temperature

The Debye model can be used to describe atomic vibration in solids. Unlike the Einstein model, the vibrational frequency ω is not constant for all atoms, but has the distribution (in 3D) [34]:

$$g(\omega) = \begin{cases} 3\omega^2/\omega_D^3 & \text{for} \quad \omega < \omega_D \\ 0 & \text{for} \quad \omega > \omega_D. \end{cases} \tag{2.23}$$

Within this model, the *Debye temperature* is defined as [34]:

$$\Theta_D = \frac{\hbar\omega_D}{k_B}. \tag{2.24}$$

The phonon DOS $g(\omega)$ of real crystals differs from the Debye model. The dependence of the phonon DOS on the square of the phonon frequency (in 3D) is too general. However, experimental data shows that the Debye model can be successfully applied for the calculation of thermo-elastic properties of the solid and Θ_D is therefore an important parameter [24].

Sound velocity

Acoustic phonons are found in the low energy part of the phonon DOS and are responsible for the transfer of heat (mainly in non metals) and sound in solids. In the limit of small energy transfers in isotropic, or polycrystalline samples, the low energy part of the phonon DOS $g(E)$ can be approximated by [35]:

$$g(E) = \frac{M'}{M}\frac{E^2}{2\pi^2\hbar^3\rho v_D^3} , \tag{2.25}$$

with M' the mass of the resonant nucleus (if measured from nuclear resonant scattering), M the mass of the host material and ρ the number density of the whole solid. v_D is the Debye sound velocity of the solid, defined as the average over all sound velocities [36].
In anisotropic and isotopically pure samples, the sound velocities depend on the crystallographic direction, thus, on the phonon polarization and the measured direction. A direction dependent *mean sound velocity* $\bar{c}_k$ along the direction $\vec{k}_0$ can be defined and the low energy part of the phonon DOS approximated by [37]:

$$\tilde{g}(E, \vec{k}_0) = \frac{E^2}{2\pi^2\hbar^3\rho} \frac{1}{\bar{c}_k^3(\vec{k}_0)} \,. \tag{2.26}$$

Mean force constant
Knowing the phonon density of states $g(E)$, the mean force constant can be calculated [2]:

$$K = \frac{1}{4} \int g(E) E \frac{e^{\beta E} + 1}{e^{\beta E} - 1} dE \,. \tag{2.27}$$

When the direction projected phonon DOS $\tilde{g}(E, \vec{k}_0)$ is measured, the direction projected mean force constant $K(\vec{k}_0)$ is calculated by Eqn.(2.27).

2.1.3. First-principles calculations

The comprehensive understanding of lattice dynamics requires the knowledge of the full dispersion relation. This information is impossible to be achieved only from experiments. The experimental results are often compared with the theoretical models such as the Born-von-Kármán-model, for example. The comparison with results from first-principles calculations is another approach, which was employed in this thesis. Therefore, the main aspects of this approach should be explained here briefly:
Within the adiabatic approximation, the electrons are assumed to be in the ground state independent of the position of the nucleus. The force constants (Eqn.(2.7)) are determined by the minimization of the total energy of the crystal at any position of the lattice vibration [24]. It was demonstrated that the electron charge density shows a linear response on the change of the nuclear position. Therefore, the information about the force constant is embedded in this linear response [24]. Within the density functional theory (DFT), the electron charge density describes the electron interactions avoiding the many-body problem of electron-electron interactions [38, 39, 40, 24].
All lattice dynamics calculations presented in this thesis were performed by Dr. habil. P. Piekarz in the group of Prof. K. Parlinski from the Institute of Nuclear Physics (PAS) in Krakow, Poland. The *ab initio* calculations are performed using the DFT implemented in the VASP program [41] using the *full potential projector augmented method* [42]. Phonon energies, dispersion relations, thermodynamic and elastic properties are calculated from the *direct method* [43, 44] implemented in the PHONON software [45, 46].

2.2. Nuclear resonant absorption/emission of photons

The methods for characterization of the hyperfine interactions at the nucleus and determination of the lattice dynamics, used in this thesis are based on the resonant recoilles absorption/emission of photons from the nuclei, namely the Mössbauer effect. Therefore, some basic considerations about the Mössbauer effect that are important for the understanding and interpretation of the experimental results are presented here.

If a photon is absorbed or emitted by a free nucleus the nucleus receives a recoil due to the conservation of energy and momentum. The nuclear excited state has a certain lifetime τ and a natural full width at half maximum Γ_0 at the energy E_0, related by the Heisenberg's uncertainty principle $\Gamma_0 = \frac{\hbar}{\tau}$. A part of the energy of the photon is transferred as kinetic energy to the nucleus during the excitation process [47]. The recoil energy of the nucleus interacting with a photon of the energy E_γ is given by:

$$E_R = \frac{E_\gamma^2}{2Mc^2}, \tag{2.28}$$

with M being the mass of the free nucleus and c the speed of light. The resonant excitation of the nucleus is only possible if the photon energy E_γ is equal to the sum of the energy of the nuclear transition and the recoil energy: $E_\gamma = E_0 + E_R$. During the emission process the energy of the emitted photon is reduced by the recoil energy $E_\gamma = E_0 - E_R$. Therefore, the absorption(A,+)/emission(E,−) cross section $\sigma^{A/E}(E)$ is given by [34]:

$$\sigma^{A/E}(E) = \sigma_0 \frac{\left(\frac{\Gamma_0}{2}\right)^2}{(E - (E_0 \pm E_R))^2 + \left(\frac{\Gamma_0}{2}\right)^2}, \tag{2.29}$$

with σ_0 the maximal value of the cross section for the nuclear resonant absorption/emission [48]:

$$\sigma_0 = \frac{2\pi}{k^2} \frac{1 + 2I_{ex}}{1 + 2I_g} \frac{1}{1 + \alpha}. \tag{2.30}$$

with I_{ex},I_g, the nuclear angular moments of the nuclear exited (ex) and ground state (g), k, the wavevector of the photon and α, the internal conversion coefficient. The factor $\frac{1}{1+\alpha}$ in Eqn.(2.30) is the probability for the de-excitation process via the emission of a photon. It reflects the fact that in addition to the radiative decay from the excited state a decay via internal electron conversion is possible [36]. Nuclear resonant absorption is only possible if the distributions of σ^A and σ^E overlap at least partly. This is not the case for a free, heavy atom. The most common example is the transition with the energy $E_0 = 14.4\,\text{keV}$ and lifetime $\tau = 141\,\text{ns}$ in the nucleus of ^{57}Fe. The natural line width $\Gamma_0 = 4.7 \cdot 10^{-9}\,\text{eV}$ is six orders of magnitude smaller than the recoil energy $E_R = 2 \cdot 10^{-3}\,\text{eV}$. Thus, the line width is extremely narrow and resonant absorption for a free Fe atom is unlikely since the absorption/emission cross sections do not overlap. The resonant process appears if the atoms are bound in a crystal because the recoil energy can be compensated by an interaction with

the crystal lattice. The nuclear resonant absorption/emission cross section $\sigma_N^{A/E}$ ($E_R = 0$) is then calculated by:

$$\sigma_N^{A/E} = b f_{LM} \sigma_0 \frac{\left(\frac{\Gamma_0}{2}\right)^2}{(E - E_0) + \left(\frac{\Gamma_0}{2}\right)^2}. \tag{2.31}$$

b is the isotopic enrichment of the considered isotope of the material and f_{LM} is the Lamb-Mössbauer factor. The Lamb-Mössbauer factor is the probability for the nuclear resonant absorption/emission of photons. The f_{LM} factor describes the interaction of the photon with the lattice and will be discussed in the following section. The Mössbauer effect is an isotope selective process. For example, the Mössbauer transition at $E_\gamma = 14.4\,\mathrm{keV}$ exists only in the nuclei of the isotope ^{57}Fe. Due to a different amount of neutrons, the nuclear states of all other isotopes of Fe exhibit higher nuclear transition energies that leads to a vanishing probability for the Mössbauer effect.

Within the scope of this thesis, the Mössbauer transitions of ^{149}Sm with the transition energy $E_\gamma = 22.496\,\mathrm{keV}$ and ^{151}Eu with $E_\gamma = 21.531\,\mathrm{keV}$ [49] are used for the investigation of material properties.

2.2.1. Lamb-Mössbauer factor

In the case of thermal motion of a free atom, a small overlap between the nuclear absorption/emission cross sections is possible because the thermal velocities obey the Maxwell distribution. The probability for resonant absorption in this case is still very small [34]. If the nucleus is bound in a crystal lattice it is possible to excite lattice vibrations (phonons) when the recoil energy is in the range of their excitation energy (meV). Depending on the recoil energy the resonant absorption/emission of photons without creation or annihilation of phonons can take place. The probability for this so-called zero-phonon transitions is given by the Lamb-Mössbauer factor f_{LM} [34]. This factor is of great importance for the application of nuclear resonant scattering and therefore will be derived here.
In the classical electrodynamics, this factor can be calculated from the assumption that the vibration of the nucleus around its center of mass leads to a modulation of the frequency of the emitted electromagnetic wave. The Lamb-Mössbauer factor can be expressed with the mean square displacement $\langle x^2 \rangle = \frac{1}{2} \sum_m x_m^2$ and the wavevector $\vec{k}$ as [34]:

$$f_{LM} = \exp\left[-k^2 \left\langle x^2 \right\rangle\right]. \tag{2.32}$$

f_{LM} has a significant value when $k^2 \langle x^2 \rangle \ll 1$. The mean square displacement $\langle x^2 \rangle$ has to be smaller than the wavelength of the emitted photon. The nucleus has to be bound in a lattice. In the classical picture, the mean square displacement is proportional to the temperature $T \sim \langle x^2 \rangle$, which does not account for existing oscillation at temperature $T = 0\,\mathrm{K}$.

In the quantum mechanical treatment, the energy of the oscillator is replaced by the quantum mechanical expression for the harmonic oscillator Eqn.(2.9) and the occupation of the states is described by the Bose-Einstein statistics. Assuming the simplest model of the solid – the Einstein model– all atoms vibrate with the same frequency Ω. The mean square displacement is in this case [34]:

$$\left\langle x^2 \right\rangle_E = \frac{\hbar}{2M\Omega}\left[1 + \frac{2}{\exp(\hbar\Omega/k_BT) - 1}\right], \tag{2.33}$$

with the atom mass M and the Boltzmann constant k_B. With the normalization condition $\int g(\Omega)d\Omega = 3N$ (N the number of atoms, $g(\Omega)$ density of phonon states in the Einstein model) and the classical mean square displacement replaced by the quantum mechanical expression: $\langle x^2\rangle = \langle u^2\rangle /3$ with $\langle u^2\rangle = \langle x^2\rangle + \langle y^2\rangle + \langle z^2\rangle$, the quantum mechanical expression for f_{LM} within the Einstein model is written as:

$$f_{LM}(\Omega) = \exp\left\{-\frac{\hbar^2k^2}{6MN}\int_0^\infty \frac{g(\Omega)}{\Omega}\left[1 + \frac{2}{\exp(\hbar\Omega/k_BT) - 1}\right]d\Omega\right\}. \tag{2.34}$$

Using the Debye density of states $g(\omega)$ from Eqn.(2.23) and the Debye temperature from Eqn.(2.24), the Lamb-Mössbauer factor can be calculated in the Debye model with the substitution $y = \hbar\omega/k_BT$:

$$f_{LM}(T) = \exp\left\{-\frac{3\hbar^2k^2}{Mk_B\Theta_D}\left(\frac{1}{4} + \left(\frac{T}{\Theta_D}\right)^2\int_0^{\Theta_D/T}\frac{y}{\exp(y) - 1}dy\right)\right\}. \tag{2.35}$$

For low temperatures ($T \ll \Theta_D$), the integral borders can be set to $\Theta_D/T \to \infty$ and the integral can be solved directly using the Debye integral $\int_0^\infty \frac{y}{\exp(y)-1}dy = \frac{\pi^2}{6}$, which leads to the low temperature approximation :

$$f_{LM}(T) \approx \exp\left\{-\frac{3\hbar^2k^2}{4Mk_B\Theta_D}\left(1 + \frac{2\pi^2}{3}\left(\frac{T}{\Theta_D}\right)^2\right)\right\}. \tag{2.36}$$

For high temperatures ($T > \Theta_D$), f_{LM} can be approximated by [34]:

$$f \approx \exp\left\{-\frac{3\hbar^2k^2T}{Mk_B\Theta_D^2}\right\}. \tag{2.37}$$

From these equations it follows that the condition for high f_{LM} value is $T < \Theta_D$. The higher Θ_D and the smaller the recoil energy, the higher f_{LM} is. This result has a strong influence on the experimental conditions. In materials with low Θ_D or high transition energies, cooling of the sample during the experiment is necessary to achieve high values of f_{LM}. This is particularly important for experiments with rare earth elements and their nanostructures.

2.2.2. Hyperfine interactions

Quickly after its observation and explanation by Rudolf Mössbauer (Nobel Prize 1961) nuclear resonant absorption of photons became a well established spectroscopy

technique for the investigation of electronic, magnetic and dynamic properties of materials. The interactions between the nucleus and the electromagnetic fields produced by its atomic electrons, neighboring atoms or external fields are referred to as nuclear hyperfine interactions. A detailed information about the chemical (oxidation) state, magnitude and direction of the electromagnetic fields acting at the nuclei or information about the structure of the nucleus can be obtained by the analysis of these interactions.
The photon energies and the hyperfine splitting have different energy scales [50]:

$$\text{nuclear transition energy (keV)} \quad \Longleftrightarrow \quad \text{nuclear hyperfine splitting (neV)}$$

The nuclear hyperfine interactions are small in comparison to the energy of the nuclear levels and therefore can be treated with the perturbation theory [34]:

$$\hat{H}_n = \hat{H}_n^0 + \hat{H}_{hf}, \tag{2.38}$$

with the Hamiltonian of the unperturbed nucleus $\hat{H}_n^0$ and the perturbation Hamiltonian $\hat{H}_{hf} = \hat{H}_{el} + \hat{H}_{mag}$, describing electric ($\hat{H}_{el}$) and magnetic ($\hat{H}_{mag}$) hyperfine interactions.

Electric hyperfine interactions: $\hat{H}_{el}$

Considering the nucleus with a charge distribution $\rho_n(\vec{r})$ within a certain volume (the origin of the coordinate system at the center of the charge distribution), the Coulomb interaction can be described by an electric potential $V(\vec{r})$, originating from all charges surrounding the nucleus. The electrostatic interaction energy is written as an integral over the entire volume of the nucleus [34]:

$$E_e = \int \rho_n(\vec{r}) V(\vec{r}) d^3r. \tag{2.39}$$

Expanding the electric potential $V(\vec{r})$ in a Tailor series around the origin of $\vec{r}$ allows to write the electrostatic interaction energy (Eqn.(2.39)) with the components $x_{i,j}$ of $\vec{r}$ as:

$$E_e = \underbrace{V(0) \int \rho_n(\vec{r}) d^3r}_{E_0} + \underbrace{\sum_{i=1}^{3} \left(\frac{\delta V(\vec{r})}{\delta x_i} \right)_{r=0} \int \rho_n(\vec{r}) x_i d^3r}_{E_1} + \underbrace{\frac{1}{2} \sum_{i,j=1}^{3} \left(\frac{\delta^2 V(\vec{r})}{\delta x_i \delta x_j} \right)_{r=0} \int \rho_n(\vec{r}) x_i x_j d^3r}_{E_2} + \cdots \quad . \tag{2.40}$$

$E_0 = V_0 eZ$, with the electron charge e and the atomic number Z, is the constant interaction energy if the nucleus is treated as a point charge. This term is not of interest because it equally affects the ground and excited nuclear states. The second term E_1, contains the electric dipole moment. As $\rho_n(\vec{r})$ is an even function, the

integral is vanishing and E_1 is zero. The quadrupole term E_2, can be rewritten by adding and subtracting $\frac{1}{3}\delta_{ij}\rho_n(\vec{r})r^2$:

$$E_2 = \underbrace{\frac{1}{6}\left[\sum_{i=1}^{3} V_{ii}\right]\int r^2\rho_n(\vec{r})d^3r}_{E_{IS}} + \underbrace{\frac{1}{6}\sum_{i,j=1}^{3} V_{ij}Q_{ij}}_{E_Q}. \tag{2.41}$$

The first term in Eqn.(2.41) is refered to as *isomer* or *chemical shift* (*IS*). The second term is the so-called *electric quadrupole term* E_Q, with the quadrupole moment tensor:

$$Q_{ij} = \int (3x_ix_j - \delta_{ij}r^2)\rho_n(\vec{r})d^3r, \tag{2.42}$$

and the electric field gradient tensor:

$$V_{ij} = \left(\frac{\delta^2 V(\vec{r})}{\delta x_i \delta x_j}\right)_{r=0}. \tag{2.43}$$

Isomer shift (*IS*)

The scalar potential $V(\vec{r})$ is given by the Poisson's equation at $\vec{r} = 0$. The coordinate system is chosen to coincide with the principal axes system where the tensor V_{ij} is diagonal:

$$\sum_{i=1}^{3} V_{ii} = -4\pi\rho_e(0)\ . \tag{2.44}$$

$\rho_e(0) = -e\left|\Psi(0)\right|^2$ with the electron charge e, is the electron charge density responsible for the potential V_{ii} and $\left|\Psi(0)\right|^2$ the probability to find an electron at the center of the nucleus.
The mean square radius of the nuclear charge distribution is defined by $\langle r^2\rangle = (1/eZ)\int r^2\rho_n(\vec{r})d^3r$. With a spherical nucleus of radius R and a uniform charge density $\rho(\vec{r}) = Ze\frac{3}{4\pi}R^3$, the isomer shift is written as [34]:

$$E_{IS} = \frac{2\pi}{5}e\left|\Psi(0)\right|^2 R^2. \tag{2.45}$$

In comparison to a point charge, the energy level of a nucleus with a certain volume is changed by E_{IS}. The radius of the nucleus differs in the ground (g) and the excited state (ex). Thus, the energy level of the ground and the excited state are shifted by slightly different amounts. This difference is small and the approximation $R_{ex} - R_g = \delta R$ and $R_{ex} + R_g = 2R$ is valid [34]. With this approach we obtain:

$$\Delta E_{IS} = E_{IS}^{ex} - E_{IS}^{g} = \frac{2\pi}{5}e\left|\Psi(0)\right|^2\frac{\delta R}{R}R^2. \tag{2.46}$$

The isomer shift of a material (m) is measured relative to a reference (ref) of the same isotope. Fig. 2.4 shows the nuclear levels of the reference and the material. The offset of the energy level due to the surrounding electrons is labeled $E_{IS}^{ex,g}$. For example the nuclear transition of ^{151}Eu in Eu_2O_3 can be used as a reference to

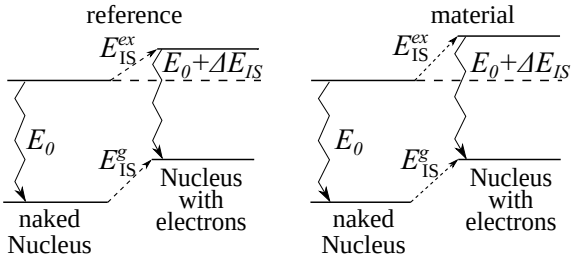

Figure 2.4.: The nuclear level of the reference and the material. The shift of the levels $E_{IS}^{ex,g}$ originating from the influence of the surrounding electrons is indicated.

determine the isomer shift of metallic Eu. The nuclear properties $\frac{\delta R}{R}$ and R^2 are the same in reference and material. The difference arises from the probability to find s-electrons at the nucleus $|\Psi(0)|$ that is sensitive to the valence state of the Mössbauer isotope and its chemical bonding. This difference is referred to as the isomer shift and is calculated by [34]:

$$\delta_{IS} = \Delta E_{IS}^{ref} - \Delta E_{IS}^{m} = \frac{4\pi}{5} S(Z) \left[\left| \Psi^{ref}(0) \right|^2 - |\Psi^{m}(0)|^2 \right] \frac{\delta R}{R} R^2. \tag{2.47}$$

The relativistic factor $S(Z)$ is introduced due to relativistic effects in heavy elements.

The material investigated in the frame of this thesis exhibit the values of $S(Z) = 3.99$ for ^{151}Eu, $S(Z) = 3.84$ for ^{149}Sm [51]. For ^{151}Eu $\frac{\delta R}{R} = 0.60 \cdot 10^{-3}$ and $R^2 = 47.0\,\mathrm{fm}^2$ [52].

Electric quadrupole splitting: $\hat{H}_{el}$

The Laplace equation applies for the potential originating from external electrons (outside of the nuclear charge density). In this case the isomer shift term does not contribute to Eqn.(2.41). The quadrupole interaction term is:

$$E_Q = \frac{1}{6} \sum_{i,j=1}^{3} V_{ij} \underbrace{\int \left(3x_i x_j - \delta_{ij} r^2 \right) \rho(\vec{r}) dr}_{Q_{ij}} \ . \tag{2.48}$$

The quantization axis z is the main axis for the nuclear quadrupole moment tensor Q_{ij}, which in that case is symmetric with trace zero. One independent variable Q is enough to fully characterize the nuclear quadrupole moment [34]. If the nucleus is elongated along z (prolate shape) $(z > x, y)$ then $Q > 0$. It has an oblate form if $z < x, y$ and $Q < 0$. In the case of spherical symmetry, $Q = 0$ [24].
For the transformation from the classical to the quantum mechanical expression, the classic density ρ_n is replaced by a sum over all protons of the quantum mechanical density operator $\hat{\rho}(\vec{r}) = \sum_p e\delta(\vec{r} - \vec{r}_p)$ and the Wigner-Eckart theorem is applied: The tensor of the electric quadrupole moment can be replaced by a tensor operator

[34]. Thus, $Q \sim I(2I-1)$ with I the nuclear angular momentum. Q is zero if $I = 0$ or $\frac{1}{2}$, only if the nuclear angular momentum $I > \frac{1}{2}$ a quadrupole interaction is found [34].
The main axis of the electric field gradient tensor V_{ii}, is chosen in a way that it has a diagonal form with $|V_{zz}| \geq |V_{xx}| \geq |V_{yy}|$. In this case an asymmetry parameter is defiend as $\eta = \frac{V_{xx}-Vyy}{V_{zz}}$. Defining z as the quantization axis and the operators $I_{\pm} = I_x \pm iI_y$, the perturbation Hamiltonian for the quadrupole interaction H_Q is written as [34]:

$$H_Q = \frac{eQV_{zz}}{4I(2I-1)}\left[3\hat{I}_z^2 - \hat{I}^2 + \frac{1}{2}\eta(\hat{I}_+^2 + \hat{I}_-^2)\right], \tag{2.49}$$

The eigen energies to this Hamiltonian are:

$$E_Q = \frac{eQV_{zz}}{4I(2I-1)}\left[3m^2 - I(I+1)\right]\left(1 + \frac{\eta^2}{3}\right)^{\frac{1}{2}}, \tag{2.50}$$

with the scalar quadrupole moment Q, the z component of the electric field gradient V_{zz}, the nuclear angular momentum I, and the asymmetry parameter η. The quantum number $m = I, I-1, ... -|I|$ appears only squared therefore each sublevel is twofold degenerated. In the case of a nonzero η, I_z is not a "good" quantum number and "forbidden" transitions with $\Delta m \pm 2$ appear [53].

^{151}Eu has the nuclear angular moment $I_g = \frac{5}{2}$ in the ground state (g) and $I_{ex} = \frac{7}{2}$ in the excited state (ex). The electric quadrupole moments for the ground and excited state are $Q_g = 1.14$ barn and $Q_{ex} = 1.49$ barn [36]. At ambient pressure, Eu exhibits the *bcc* crystal structure and therefore $V_{xx} = V_{yy} = V_{zz}$. Therefore, quadrupole splitting does not appear in *bcc* Eu.
Sm exhibits the non-cubic $9R$ structure. The angular moments are $I_g = \frac{7}{2}$, $I_{ex} = \frac{5}{2}$ and the electric quadrupole moments are $Q_g = 0.058$ barn and $Q_{ex} = 0.50$ barn. The ground state splits in 4 and the excited state in 3 sublevels [24]. The states are twofold degenerated. In the cases of $\eta \neq 0$ and $I > 2$ the eigenvalues are usually calculated numerically [54, 53].

Magnetic hyperfine interaction: $\hat{H}_{mag}$

The (anomalous) nuclear Zeeman effect is an analog of the Zeeman effect observed in the electron shell. Its origin is the interaction of the magnetic moment $\vec{\mu}$ of the nucleus and the magnetic field $\vec{B}$ that leads to an equidistant splitting of the nuclear states. The magnetic perturbation Hamiltonian is [34]:

$$\hat{H}_{mag} = -\vec{\mu}\vec{B} = -g\mu_N\vec{I}\vec{B}. \tag{2.51}$$

with $\vec{\mu}$ the magnetic moment, g the Landé factor, μ_N the nuclear magneton, $\vec{I}$ the nuclear angular moment and $\vec{B}$ the magnetic field. The direction of the magnetic

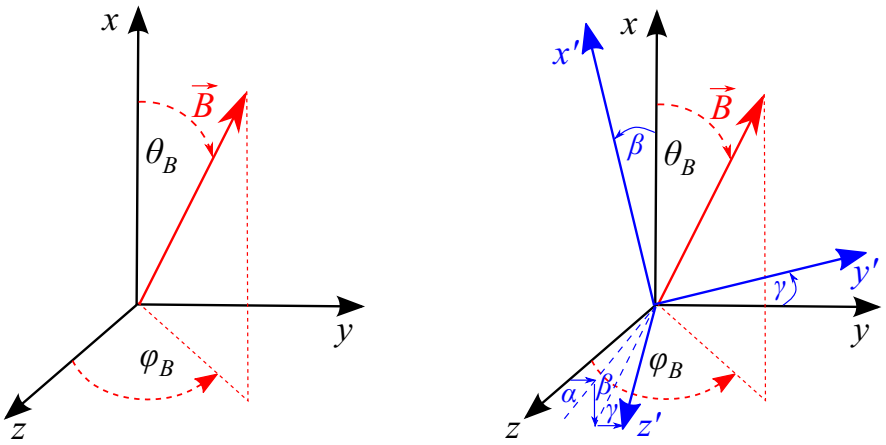

(a) $\vec{B}$ in the main axis (xyz) **(b)** main axes ($x'y'z'$) of the EFG

Figure 2.5.: a) Orientation of the magnetic field with respect to the quantization axis z with the angles θ_B and ϕ_B. b) Orientation of the main axis ($x'y'z'$) of the *EFG*-tensor with respect to the quantization axis z. $\alpha\beta\gamma$ are the Euler angles for the transformation from $x'y'z'$-axis of the EFG to the xyz-quantization axis of the magnetic field $\vec{B}$.

field is described by the angles θ_B and ϕ_B (Fig.2.5 a)). With the operators $I_\pm = I_x \pm iI_y$, Eqn.(2.51) can be rewritten:

$$\hat{H}_{mag} = -g\mu_N B \left[I_z \cos\theta_B + \frac{1}{2}(I_+ e^{-i\phi_B} + I_- e^{i\phi_B}) \sin\theta_B \right]. \tag{2.52}$$

In the special case when θ_B is zero, Eqn.(2.52) reduces to $\hat{H}_{mag} = -g\mu_N I_z B$ with the corresponding energies of the sublevels given by:

$$E_{mag} = -gmB\mu_N, \tag{2.53}$$

with $m = I, I-1, ..., -I$ and $2I+1$ possible sublevels. Provided that the transition is of the magnetic dipole (M1) type, the selection rules are: $\Delta m = -1, 0, +1$. The transition energies are calculated by:

$$E = E_0 - (\frac{\mu_{ex}}{I_{ex}} m_{ex} - \frac{\mu_g}{I_g} m_g)B, \tag{2.54}$$

with E_0 the unperturbed energy, $\mu_{ex,g}$ the magnetic moments and $I_{ex,g}$ the nuclear angular moments of the excited and the ground states.

For ^{151}Eu ($I_g = \frac{5}{2}$,$I_{ex} = \frac{7}{2}$) and ^{149}Sm ($I_g = \frac{7}{2}$, $I_{ex} = \frac{5}{2}$) 18 transitions are allowed (Fig. 2.6).

In the general case, the magnetic field at the nucleus is a superposition of several contributions [24]:

$$B = B_{Ext} + B_{tHf} + B_S + B_L + B_D. \tag{2.55}$$

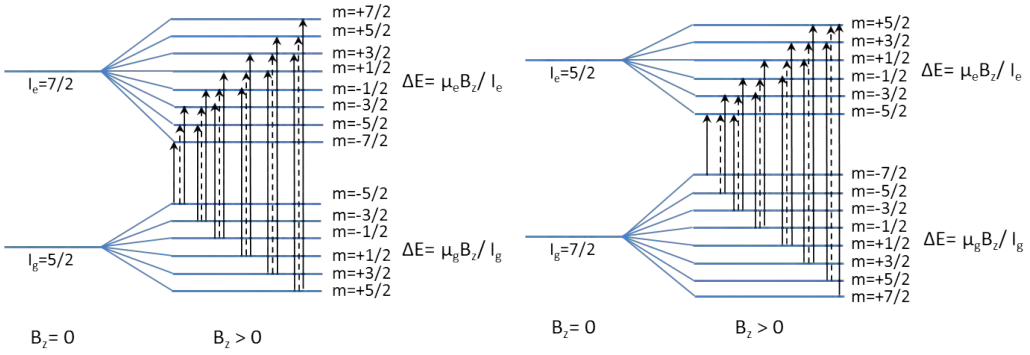

(a) ^{151}Eu **(b)** ^{149}Sm

Figure 2.6.: Nuclear levels and the splitting of the levels due to magnetic hyperfine interaction for the ground and first exited states in the nuclei of a) ^{151}Eu and b) ^{149}Sm. The solid lines correspond to $\Delta m = \pm 1$ the dashed lines correspond to $\Delta m = 0$.

- B_{Ext}: An external magnetic field.
- B_{tHf}: The influence of the surrounding nuclei via the magnetic interaction.
- B_S: The Fermi contact field produced by the interaction of the spin-up and spin-down s-electron density at the nucleus with the nuclear magnetic moment. The s-electrons are polarized in two groups through the interaction with the outer shells. As they have large densities at the nucleus there is a net interaction which leads to a magnetic field.
- B_L: Orbital field. Unpaired electrons in not completely filled shells have an angular momentum L which interacts with the nuclear magnetic moment.
- B_D: Dipole field at the nucleus. This field originates from the total spin magnetic moment of the valence electrons. Closed or half-filled shells do not contribute. B_D is zero in a charge distribution of cubic symmetry but can have large values if the orbital momentum is not suppressed.

B_L fields are relatively large for rare earths metals. In some rare earth compounds B_D has large values if the orbital momentum is not suppressed [24].

Usually, the magnetic field and the electric field gradient appear simultaneously. The hyperfine splitting depends on the relative orientations of the *EFG* main axis ($x'y'z'$) (Fig. 2.5 b)) to the orientation of the magnetic field and the orientation of the wavevector ot the incident photon. In Fig. 2.5 b) the orientation of the quantization axis z (xyz) for the general case of the electric and magnetic fields is sketched. The *EFG* in the main axis ($x'y'z'$) can be transferred by the Euler angles ($\alpha\beta\gamma$) to the magnetic field main axis (xyz).

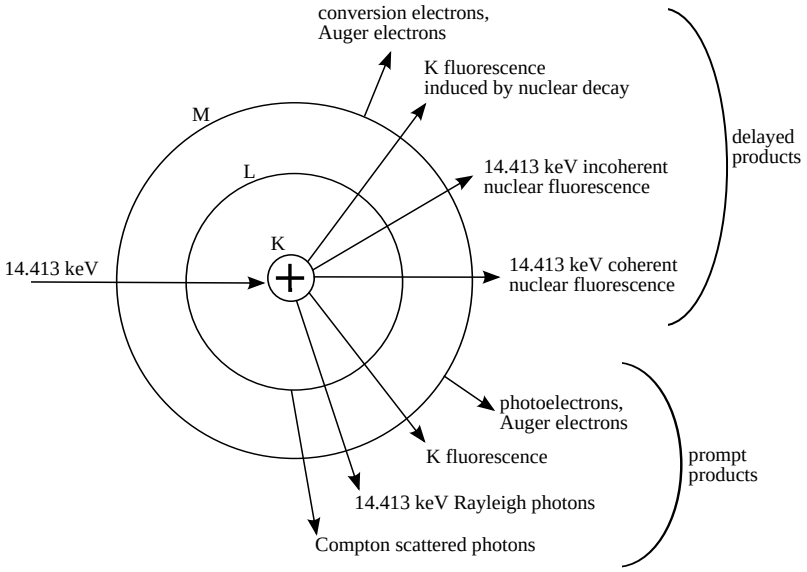

Figure 2.7.: All decay channels after the excitation of ^{57}Fe [56] with photons of an energy of 14.4 keV. Prompt products origin in the scattering from electrons, delayed products from the nuclear resonance absorption/emission processes.

2.3. Nuclear resonant scattering of synchrotron radiation

Classical Mössbauer spectroscopy is performed using a radioactive source. The use of synchrotron radiation instead of a radioactive source has opened new possibilities in this field of research.
If a Mössbauer active atom is excited with a synchrotron radiation (SR) pulse, the electronic scattering follows on the picoseconds time scale, i.e., instantaneously. The response of the resonant nuclei, however, is delayed. With the timing mode of the SR and the time resolution of the detectors (avalanche photo diodes (APD) [55]) it is possible to separate the nuclear from the electronic of the sample. Fig. 2.7 summarizes the prompt and delayed decay products arising from scattering of photons with an energy of 14.4 keV from the electron shell and nuclei of ^{57}Fe [56].
The following decay processes take place after the nuclear resonant absorption:

- Conversion electron emission: The excitation energy is transferred to the electron shell and an electron is emitted.
- Atomic K line X-ray fluorescence induced by the internal conversion: The electronic recombination after the emission of a conversion electron leads to an emission of fluorescence photons.
- Coherent/incoherent nuclear resonant fluorescence: The incident photon is absorbed and a photon is re-emitted.

The relative probability for the radiative decay (coherent/incoherent nuclear resonant fluorescence) can be expressed with $1/(1+\alpha)$ with α the internal conversion

coefficient. The probability for the internal conversion is $\alpha/(1+\alpha)$. For most Mössbauer isotopes $\alpha > 1$ that makes the internal conversion the dominant decay channel.

2.3.1. Nuclear forward scattering

Nuclear forward scattering (NFS) explores the hyperfine interaction of the nuclei by nuclear resonant scattering (NRS). It is an analog to the Mössbauer spectroscopy but using synchrotron radiation instead of a radioactive source.

A single pulse of X-rays excites all possible sub-levels of the hyper-fine split nuclear resonant level at once. The reason is that the energy resolution of meV achieved nowadays at 3^{rd} generation synchrotron radiation sources is still orders of magnitude lower compared to the hyperfine splitting of the degenerated nuclear level, which is in the neV range.
With an APD detector located in forward direction (the direction along the incident X-ray beam after the sample) the de-excitation of the nuclei is measured by detecting the coherently scattered, delayed photons. A direct consequence of the coherent nature of NFS is that only one excited state of one nucleus has to be considered, that cannot be distinguished from the other atoms. Instead, a collectively excited state is assumed where the single excitation is distributed over all states.
Due to the elastic and coherent nature of the process, the decay of this collectively excited state results in a superposition of coherent waves that interfere and form a specific temporal variation pattern of the scattered intensity which is referred to as nuclear forward scattering spectrum.

For the description of NFS, the macroscopic ensemble of scattering atoms is replaced by a continuous medium, characterized by an index of refraction $\mathbf{n}$ in matrix form [36]:

$$\mathbf{n}(\omega) = 1 + \frac{2\pi}{k_0^2} \sum_i \rho_i \mathbf{M}_i(\omega) \ , \tag{2.56}$$

with $\mathbf{M}_i$, the coherent forward scattering length of the ith atom and ρ_i, the number density of atoms in the material. k_0 is the wave number and the sum runs over all atoms in the scattering volume. In an anisotropic medium, $\mathbf{n}$ depends on the polarization of the X-ray. If the transversality of the electric field of the electromagnetic wave is used, $\mathbf{n}$ can be treated as a second-rank tensors in the two-dimensional subspace defined by the plane normal to the propagation direction of the photons with the basis σ, π.

It can be shown that the wave amplitude A in the depth d of a material with the refractive index $\mathbf{n}$ and the transition matrix $\mathbf{T}_d$ is given by [36]:

$$A_d(\omega) = e^{ik_0\mathbf{n}(\omega)d} A_0(\omega) = \mathbf{T}_d A_0(\omega). \tag{2.57}$$

The transition matrix is defined by $\mathbf{T}_d(\omega) = e^{i\mathbf{F}d}$, with the propagation matrix $\mathbf{F} = \mathbf{k_0} + \mathbf{f}$. The scattering geometry is sketched in Fig. 2.8 a). Since $e^{i\mathbf{k_0}d}$ results

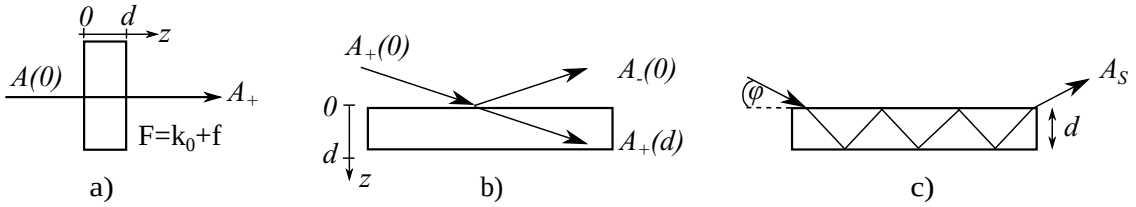

Figure 2.8.: Scattering channels in case of forward scattering in a) transmission geometry: The propagation matrix is $\mathbf{F} = \mathbf{k_0} + \mathbf{f}$. Only one scattering channel is open. b) grazing incidence geometry: Two scattering channels are open. The specularly reflected field $A_-(0)$ and the transmitted field $A_+(d)$. c) The superposition of the incident and reflected wave results in a standing wave with the amplitude A_S in a sample with thickness d [36].

in a phase shift of all components of the traveling wave, it is sufficient to calculate $\mathbf{f}$. Thus the forward scattering matrix is given by:

$$\mathbf{f}(\omega) = \frac{2\pi}{k_0} \sum_i \rho_i \mathbf{M}_i(\omega). \tag{2.58}$$

The interaction of X-rays with the atoms is contained in the scattering length $\mathbf{M}(\omega)$. This 2×2 matrix can be decomposed into an electronic non-resonant part $\mathbf{E}(\omega)$ and the nuclear resonant scattering part $\mathbf{N}(\omega)$. The matrix representation accounts for the polarization mixing, occurring due to optical activity [36]:

$$\mathbf{M}(\omega) = \mathbf{E}(\omega) + \mathbf{N}(\omega). \tag{2.59}$$

The electronic scattering length $\mathbf{E}(\omega)$ can be expressed by [36]:

$$[\mathbf{E}(\omega)]_{\mu\nu} = (\epsilon_\mu \cdot \epsilon_\nu) \left[-Z r_0 + i \frac{k_0}{4\pi} \sigma_t(\omega) \right] , \tag{2.60}$$

with Z the atomic number, r_0 the classical electron radius and $\sigma_t(\omega)$ the total absorption cross section in the polarization basis σ, π, k_0 for the polarization basis vectors ϵ_μ and ϵ_ν.
The nuclear resonant part $\mathbf{N}(\omega)$ for electric 2^L transitions is expressed in its matrix elements [36]:

$$[\mathbf{N}(\omega)]_{\mu\nu} = \frac{4\pi}{k_0} \sum_{M=-L}^{L} \left[\vec{\epsilon_\nu} \cdot \mathbf{Y}_{ML}(\vec{k_0}, \vec{m}) \right] \left[\mathbf{Y}^*_{ML}(\vec{k_0}, \vec{m}) \cdot \vec{\epsilon_\mu} \right] F_M(\omega) \ . \tag{2.61}$$

$\mathbf{Y}_{ML}(\vec{k_0}, \vec{m})$ are the vector spherical harmonics that describe the multipole transitions [50]. They depend on $\vec{k_0}$, the orientation of the photon wavevector and the unit vector $\vec{m}$ defining the orientation of the magnetic quantization axis. In the case of a magnetic dipole transition (M1) the polarization vectors are transformed by the cross product with the unit vector along the photon vector.
The energy dependent part of $\mathbf{N}(\omega)$ is [36]:

$$F_M(\omega) = \frac{2\pi}{k_0(1+\alpha)} \frac{\Gamma_0}{2I_g + 1} f_{LM} b \sum_{m_g} \frac{C^2(I_g 1 I_{ex}; m_g M)}{(E_{(m_g, m_{ex}=m_g+M)} - \hbar\omega) - i\Gamma_0/2} \ , \tag{2.62}$$

containing the coefficient of internal conversion α, the spin of the ground and excited state $I_{g,ex}$, the Lamb-Mössbauer factor f_{LM} and the isotope abundance b. The sum runs over all ground states with m_g and Γ_0 is the resonance width. $E_{(m_g,m_{ex}=m_g+M)}$ is the resonance energy of the transition from m_g to the state of the quantum number $m_{ex} = m_g + M$ and $C^2(I_g 1 I_{ex}; m_g M)$ are the Clebsch-Gordan coefficients for those transitions. $F_M(\omega)$ is a sum of Lorentzian resonances corresponding to the various allowed transitions between the ground and excited hyperfine split states. Together with Eqn.(2.61) and transformed polarization vectors ($\vec{\epsilon} \rightarrow \vec{\epsilon} \times \vec{k_0}$) for magnetic dipole transitions (M1), the matrix elements of $\mathbf{N}(\omega)$ can be expressed as [36]:

$$\begin{aligned}[\mathbf{N}(\omega)]_{\mu\nu} = \frac{3}{16\pi}\left\{(\epsilon_\nu \cdot \epsilon_\mu)\left[F_{+1} + F_{-1}\right]\right\} \\ - \frac{3}{16\pi}\left\{i(\vec{\epsilon_\nu} \times \vec{\epsilon_\mu}) \cdot \vec{m}\left[F_{+1} - F_{-1}\right]\right\} \\ - \frac{3}{16\pi}\left\{(\vec{\epsilon_\nu} \cdot \vec{m})(\vec{\epsilon_\mu} \cdot \vec{m})\left[2F_0 - F_{+1} - F_{-1}\right]\right\} \quad (2.63)\end{aligned}$$

The optical activity depends on the orientation of $\vec{m}$ to the incident wavevector $\vec{k}_0$ and the polarization state σ, π. The off-diagonal elements describe the polarization rotation from $\vec{\sigma}$ to $\vec{\pi}$ and *vice versa*. Thus, polarization mixing effects appear in resonant scattering experiments on magnetized samples, which strongly depends on the orientation of $\vec{m}$ relative to $\vec{k}_0$ and the polarization states.

The transmission matrix $\mathbf{T}_d(\omega) = e^{ik_0 \mathbf{n} d}$ can be calculated using Eqn. 2.57, 2.62 and 2.63. The intensity is defined as $I(t) = |A_d(t)|^2$ – with the amplitude defiend in Eqn. (2.57) – and therefore can be calculated from the Fourier transform of the squared transmission matrix. In the case of σ-polarized incoming radiation, as in the case of a standard SR experiment, the transition matrix, expressed in the basis of the polarization vectors σ, π, is:

$$\mathbf{T}_d(\omega) \cdot \sigma = \begin{pmatrix} T_{\sigma\sigma}(\omega) \\ T_{\pi\sigma}(\omega) \end{pmatrix} . \quad (2.64)$$

With the intensity:

$$I(t) = |A|^2 = I_{\sigma\sigma}(t) + I_{\pi\sigma}(t) = \left|\frac{1}{2\pi}\int_0^\infty T_{\sigma\sigma}(\omega) e^{-i\omega t} d\omega\right|^2 + \left|\frac{1}{2\pi}\int_0^\infty T_{\pi\sigma}(\omega) e^{-i\omega t} d\omega\right| . \quad (2.65)$$

The matrix exponentials are usually calculated numerically. Special cases exists where an analytical calculation is possible. This expression contains the restriction that the SR pulse is much shorter compared to the lifetime of the excited state and is treated as a δ(t) function [36].

Grazing incidence nuclear forward scattering

In order to enhance the surface sensitivity of the NFS, the grazing incidence geometry is applied. In this experimental geometry X-rays hit the sample at an angle,

close to the critical angle. In this case one additional scattering channel opens (Fig. 2.8 b)). The scattering matrix $\mathbf{F}$ can be expressed as a 2×2 matrix that describes the polarization amplitudes in the specular reflection and forward transmission [36]:

$$\mathbf{F} = \begin{pmatrix} \mathbf{f} + k_z & \mathbf{f} \\ -\mathbf{f} & -\mathbf{f} - k_z \end{pmatrix} . \tag{2.66}$$

$\mathbf{f}$ and $\mathbf{k}_z$ are 2×2 matrices. The angular dependence arises through $\mathbf{k}_z$ the z component of the wavevector of the incident X-ray beam. The scattering matrix $\mathbf{F}$ contains the electronic and nuclear scattering properties and depends on ω (Eqn. 2.62 and 2.63). For the calculation of the specularly reflected amplitude $\mathbf{A}_-(0)$ (Fig. 2.8 b)), the so called *layer matrix* ($\mathbf{L}$) formalism is used [36]. The amplitudes $\tilde{A}$ can be calculated by:

$$\tilde{\mathbf{A}}(d) = \mathbf{L}_i(d)\tilde{\mathbf{A}}(0) = e^{i\mathbf{F}_i d}\tilde{\mathbf{A}}(0) . \tag{2.67}$$

The amplitudes $\tilde{A}$ are defined with $(+)$ for the direction of incidence and $(-)$ for the direction of reflection with (Fig.2.8 b)):

$$\tilde{\mathbf{A}}(0) = \begin{matrix} \mathbf{A}_+(0)(\omega) \\ \mathbf{A}_-(0)(\omega) \end{matrix} \quad \text{and} \quad \tilde{\mathbf{A}}(d) = \begin{matrix} \mathbf{A}_+(d)(\omega) \\ 0 \end{matrix} . \tag{2.68}$$

Within this notation, the reflectivity $\mathbf{R}$ and the transmission $\mathbf{T}$ are defined as [36]:

$$A_-(0) =: \mathbf{R}A_+(0) , \tag{2.69}$$

$$A_+(d) =: \mathbf{T}A_+(0) . \tag{2.70}$$

The reflectivity $\mathbf{R}$ is used to calculate the NFS signal in grazing incidence geometry. Within the approximation of an ultra-thin film on a substrate, the exponential of the scattering matrix can be expanded up to the first order and the layer matrix turns to $\mathbf{L} \approx 1 + id\mathbf{F}$ with the reflectivity matrix [36]:

$$\mathbf{R}(\omega) \approx re^{i\mathbf{f}(\omega)t^2 \frac{d}{\alpha_{in}}} . \tag{2.71}$$

$\mathbf{R}(\omega)$ and $\mathbf{f}(\omega)$ are 2×2 matrices, d the thickens of the layer and r the reflectivity of the substrate without the resonant effect. t^2 is the relative intensity of the standing wave with the amplitude A_s (Fig. 2.8 c)) building up at the critical angle, describing the increased path length of the X-ray traveling at an angle α_{in}. The reflection of an ultra-thin film can be treated as forward scattering (Eqn. 2.65), with d increased by X-ray interference effects [36].
The time response of the system is obtained by Fourier transformation of $\mathbf{R}(\omega)$. The amplitude of the reflected radiation is expressed in the time domain by [36]:

$$\mathbf{R}(t) \approx \delta(t) - \tilde{\mathbf{f}}(t)\chi e^{-\chi t/2\tau_0} . \tag{2.72}$$

The delta function denotes the instantaneous radiation, i.e. without resonant interaction. $\tilde{\mathbf{f}}(t)$ is the Fourier transform of $\mathbf{f}(\omega)$ (Eqn.(2.71)). The time dependence is governed by the natural lifetime τ_0 and χ is defined by:

$$\chi = \frac{1}{4}\rho\sigma_0 f_{LM} |t|^2 \frac{d}{\alpha_{in}} , \tag{2.73}$$

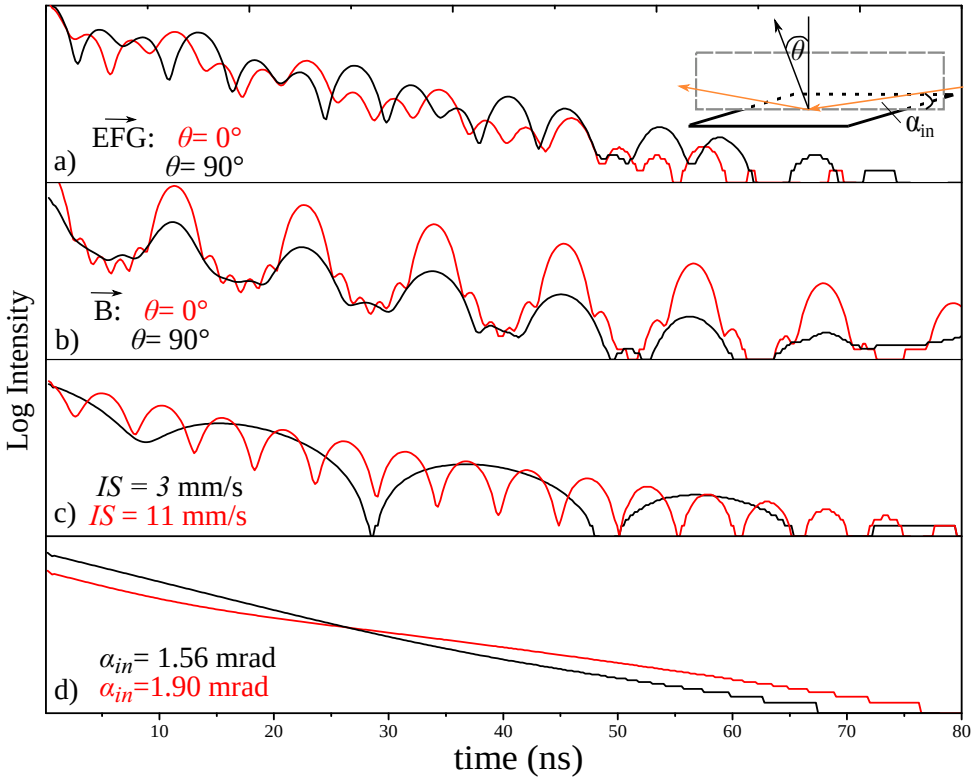

Figure 2.9.: Simulated NFS spectra for the nuclear transition in ^{149}Sm in the case of a 250 $\AA$ thick Sm film on a substrate. The inset shows the geometry with the incoming X-ray at a grazing angle α_{in} and the scattering plane (gray plane) defined by the surface normal. The influence of the a) the *EFG* and b) the magnetic field $\vec{B}$ on the the NFS spectra in the cases of orientation along the surface normal ($\theta = 0°$) and in the surface plane, along the scattered beam $\theta = 90°$. c) and d) illustrate the effect of the isomer shift and the incidence angle on the NFS spectra for different *IS* and α_{in} values, respectively.

with the density ρ, the maximal value of the cross section of the nuclear resonant absorption/emission σ_0 (Eqn.(2.30)), the Lamb-Mössbauer factor f_{LM} (Eqn.(2.32)), the relative intensity of the standing wave $|t|^2$, film thickness d and the incidence angle α_{in}.
The envelope I_{en} of the intensity I(t) calculated from Eqn.(2.72), can be approximated by:

$$I_{en} \approx \chi^2 e^{-(1+\chi)t/\tau_0} \ . \tag{2.74}$$

The decay of the nuclear excitation is accelerated compared to that of a single nucleus. This behavior is known as *speed up effect* [36].

Simulated NFS spectra are shown in Fig. 2.9 a-d) assuming the grazing incidence geometry as sketched in the inset. The simulations were done by the program REFTIM [57, 58], assuming a 250 $\AA$ thick ^{149}Sm layer on a substrate. α_{in} denotes the incidence angle and θ the angle to the normal of the surface plane. The gray dashed line denotes the scattering plane defined by the surface normal and the direction of the incident/scattered X-rays. Fig. 2.9 a) shows the dependence of the

NFS spectrum on the orientation of the electric field gradient to the scattering plane with $\theta = 0°$ (red line) and $\theta = 90°$ (black line). Fig. 2.9 b) shows the NFS spectrum as a function of the orientation of the magnetic field $\vec{B}$ for the cases of $\theta = 0°$ (red line) and $\theta = 90°$ (black line) with $B = 200\,\mathrm{T}$. The angular dependence arises through the forward scattering matrix Eqn.(2.61). Fig. 2.9 c) shows the influence of the isomer shift (Eqn.(2.47)) if two sites of the same resonant atom are equally distributed in the film and one of them exhibits the IS values $IS = 11\,\mathrm{mm/s}$ (red line), or $IS = 3\,\mathrm{mm/s}$ (black line) for comparison. In Fig. 2.9 d) the NFS spectra for different incidence angles α_{in}, without hyperfine splitting of the nuclear states, are plotted to visualize the influence of the incidence angle on the NFS spectra (Eqn.(2.72)).

2.3.2. Nuclear inelastic scattering

Nuclear resonant absorption/emission of a photon by the nucleus of an atom bound in a crystal lattice leads either to a change of only the nuclear state (nuclear resonant absorption, Mössbauer effect) or to a change of the nuclear state accompanied by a change in the vibrational quantum state of the lattice, which is the "phonon assisted nuclear resonant absorption/emission" [36] or *nuclear inelastic scattering* (NIS).

New eigenstates are created from the combination of nuclear and phonon states. This can be expressed by $|g\rangle\,|1\rangle$, i.e., the nucleus is in the ground (g) state and one phonon is present. Nuclear resonant elastic transitions are observed when the phonon state is unchanged $|g\rangle\,|n\rangle \rightarrow |e\rangle\,|n\rangle$, with g, e the ground- and exited states. This is the case for the recoilless absorption/emission of X-rays at the Mössbauer resonance. Off resonance m-phonon creation $|g\rangle\,|n\rangle \rightarrow |e\rangle\,|n+m\rangle$ leads to an increase of the transition energy E_t by $E_t = E_0 + m\epsilon$, with E_0 the transition energy without phonon creation, m the number of excited phonons and ϵ the energy of one phonon. The phonon annihilation $|g\rangle\,|n\rangle \rightarrow |e\rangle\,|n-m\rangle$ with $n \geq m$ decreases the transition energy E_t by $E_t = E_0 - m\epsilon$.
The cross section of the nuclear resonant absorption of a photon with a certain energy can be expressed as [36]:

$$\sigma(E) = \frac{2}{\pi}\sigma(E_0)\Gamma_0 S(\vec{k}_0, E - E_0), \tag{2.75}$$

with $\sigma(E_0) = \sigma_N$ the absorption cross section, the natural line width Γ_0 at the resonance energy E_0 (Eqn.(2.31)) and the excitation probability density $S(\vec{k}_0, E - E_0)$. The latter is proportional to the normalized probability for absorption per unit energy interval [36]:

$$S(\vec{k_0}, E - E_0) = \frac{1}{2\pi}\int_0^\infty e^{-iEt - \frac{\Gamma_0 t}{2}} F(\vec{k_0}, t)dt. \tag{2.76}$$

The function $F(\vec{k}_0, t)$ describes the correlation between the positions of a nucleus at different times. The dependence on the incidence vector $\vec{k_0}$ shows the anisotropic

nature of nuclear inelastic scattering. $S(\vec{k_0}, E - E_0)$ exhibits a sharp peak with the natural line width Γ at the nuclear transition energy E_0 being $\Gamma \cdot S(\vec{k_0}, 0) = f_{LM}$.

Experimentally NIS is measured by detuning the energy of the incident X-ray pulses from the Mössbauer resonance energy E_0 by a high energy resolution monochromator, while the delayed K-fluorescence photon yield is measured. Using the normalized probability for absorption, the total yield of delayed K-fluorescence photons can be expressed as [36]:

$$I(E) = I_0 \rho \sigma_N \frac{\eta_K \alpha_K}{1+\alpha} \Gamma_0 S(\vec{k_0}, E) \ , \tag{2.77}$$

with the incident flux I_0, the effective area density of the nuclei ρ, the K-fluorescence yield η_K and the total and partial internal conversions coefficients α and α_K. In approximation of a harmonic lattice, $S(\vec{k_0}, E)$ can be expanded in contributions from multi-phonon excitations [36]:

$$S(\vec{k_0}, E) = f_{LM} \left(\delta_\Gamma(E) + \sum_{n=1}^{\infty} S_n(\vec{k_0}, E) \right). \tag{2.78}$$

The zero phonon contribution S_0 is approximated by a δ-function. S_1 is the one (single) phonon contribution. Excitations with $n > 1$ are termed multi-phonon contributions.

Different moments of the excitation probability density $S(\vec{k_0}, E - E_0)$ can be calculated via the Lipkin's sum rules [59, 60]. The first moment depends only on the properties of the nuclear isotope, which are defined by the recoil energy. It also expresses the fact that, the average energy transfer to the lattice per photon emission is the recoil energy of a free atom:

$$1. \quad \int E \ S(\vec{k_0}, E) dE = E_R \ . \tag{2.79}$$

The second moment contains E_{kin}, the average kinetic energy of the resonant nuclei, which expresses the temperature dependence and the zero-point motion of the bound atoms:

$$2. \quad \int (E - E_R)^2 S(\vec{k_0}, E) dE = 4 E_R E_{kin}. \tag{2.80}$$

The third moment describes the binding strength of the atom in the lattice. It contains the mean force constant K of the resonant nuclei:

$$3. \quad \int (E - E_R)^3 S(\vec{k_0}, E) dE = \frac{\hbar^2}{m} E_R K. \tag{2.81}$$

Phonon density of states from nuclear inelastic scattering

The phonon DOS can be calculated from the NIS spectrum (Eqn.(2.77)), by decomposing $I(\vec{k_0}, E)$ to an elastic part, described by the δ-function δ_Γ and an inelastic part, described by S'_n [36]:

$$I(\vec{k_0}, E) = a \sum_{n=1}^{\infty} S'_n(\vec{k_0}, E) + b f_{LM} \delta_\Gamma(E). \tag{2.82}$$

The first of Lipkin's sum rules can be used to calculate the factor a because the central part contributes to both sides of the integral Eqn.(2.79):

$$a = \frac{1}{E_R} \int I(\vec{k_0}, E) E dE. \tag{2.83}$$

The inelastic part $I'(\vec{k_0}, E) = a \sum_{n=1}^{\infty} S'_n(\vec{k_0}, E)$ and $\int S'(\vec{k_0}, E) dE = 1 - f_{LM}$ can be derived by the subtraction of the elastic part [36]. Finally, the Lamb-Mössbauer factor can be directly calculated to:

$$f_{LM} = 1 - \frac{1}{a} \int I'(\vec{k_0}, E) dE. \tag{2.84}$$

Using the values of a and f_{LM}, the inelastic part of the spectrum $I'(\vec{k_0}, E)$ can be decomposed into single- and multi-phonon contributions.
Fig. 2.10 shows an example for the NIS spectrum ($I(\vec{k_0}, E)$) in a), the spectrum with subtracted elastic line ($I'(\vec{k_0}, E)$) in b) and different phonon contributions of the NIS spectrum in c) in the case of α-Fe (taken from [36]).
In the harmonic approximation for the lattice vibrations the (direction projected) single-phonon contribution $S_1(\vec{k_0}, E)$ and phonon density of states $\tilde{g}(\vec{k_0}, E)$ are related by [36]:

$$S_1(\vec{k_0}, E) = \frac{E_R}{E(1 - e^{-\beta E})} \tilde{g}(\vec{k_0}, E) \ . \tag{2.85}$$

Fig.2.10 d) shows the obtained phonon DOS of α-Fe. The multiphonon contribution can be calculated by [36]:

$$S_n(\vec{k_0}, E) = \frac{1}{n} \int S_{n-1}(\vec{k_0}, E - E') S_1(\vec{k_0}, E') dE', \tag{2.86}$$

which corresponds to a convolution with the one phonon therm. This equation is solved by Fourier transformation using the *Fourier-Log decomposition* [36].

The single-phonon contribution depends essentially on the subtraction of the elastic peak. Often problems related to the finite width of the resolution function appear. The area under the elastic peak in the NIS spectrum is approximated by the behavior of a Debye-like solid. This approach is problematic in case of non-Debye-like solids or in the case of a small values of f_{LM} implying a significant multi-phonon contribution to the measured signal.
The *detailed balance* [36] describes the proportionality between the Stokes and anti-Stokes part of the nuclear inelastic spectrum at a given temperature:

$$S_1(\vec{k_0}, E) = e^{-\beta E} S_1(\vec{k_0}, -E) \ . \tag{2.87}$$

If $S_1(\vec{k_0}, E)$ is obtained from the measured spectra, the density of phonon states is calculated from the positive and negative part of the spectrum by:

$$\tilde{g}(\vec{k_0}, E) = \frac{E}{E_R} (S_1(\vec{k_0}, E) + S_1(\vec{k_0}, -E)) \tanh\left(\frac{\beta E}{2}\right) \ . \tag{2.88}$$

The phonon DOS obtained from the NIS experiment exhibits the following properties:

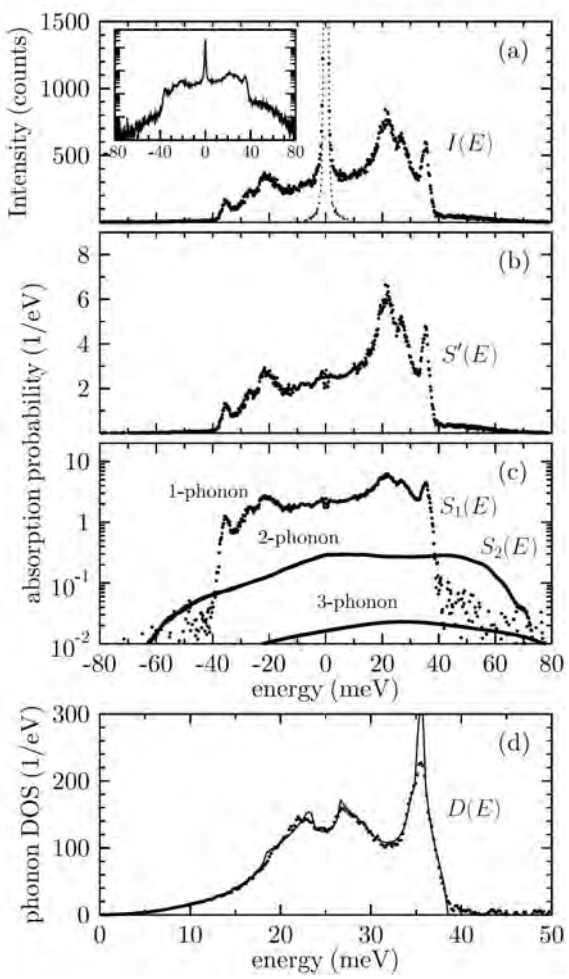

Figure 2.10.: Determination of the phonon DOS from the experimental NIS for α-Fe: (a) NIS spectra: the total yield of delayed K-fluorescence photons $I(\vec{k_0}, E)$. The same dependence is shown in semilogarithmic scale in the inset. The resolution function $R(E)$ is indicated with the dotted line. (b) $S'(\vec{k_0}, E)$ after subtraction of the elastic peak. (c) 1-, 2-, 3-phonon terms, i.e., $S_{1,2,3}$. (d) Phonon density of states $g(\vec{k_0}, E)$ determined from the single(1)-phonon term from Eqn.(2.88) (taken from [36]).

- The phonon DOS is the Mössbauer isotope specific partial phonon DOS. For compounds, oxides and alloys containing the resonant atom only the partial phonon DOS of the resonant atom can be derived.
- Due to the dependence of $S(\vec{k_0}, E)$ on the direction of the incident wavevector the derived phonon DOS is the direction-projected phonon DOS $\tilde{g}(k_0, E)$. It can be described by an integration of the phonon branches weighted by the projections of the phonon polarization vectors $e_j(\vec{q})$ along $\vec{k_0} = \vec{k}/k$, the normalized incident wavevector [2]:

$$\tilde{g}(E, k_0) = V_0 \frac{1}{(2\pi)^3} \sum_j \int d\vec{q}\ \delta(E - \hbar\omega_j(\vec{q})) \left| \vec{k_0} \cdot \vec{e}_j(\vec{q}) \right|^2 \qquad (2.89)$$

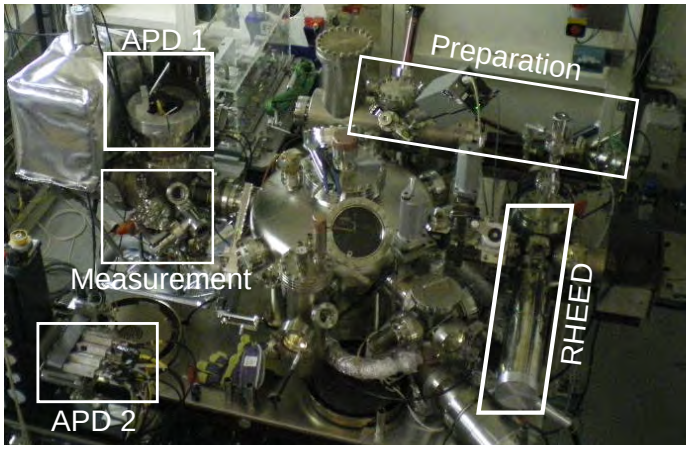

Figure 2.11.: UHV system located in the experimental hutch of ID18 with the possibility for sample preparation (Preparation), characterization with electron diffraction (RHEED) and *in situ* NIS/NFS experiments (APD 1/APD 2) at variable temperatures (Measurement) [61].

V_0 is the volume of the unit cell, the sum is over the branches j of the dispersion relation $\hbar\omega_j$. The integral over the phonon momentum $\vec{q}$ is done in the first Brillouin zone.

- In the case of the grazing incidence geometry of the experimental set up for NIS, the obtained phonon DOS is the on the sample surface plane projected one. Due to the small incidence angle, the contribution of phonons with an out of plane polarization is negligible.

2.3.3. *In situ* nuclear resonant scattering at ID18/ESRF

Investigations of ultra-thin films and nanostructures require ultra-high vacuum (UHV) conditions for sample preparation, characterization and performance of the experiment. The study of the lattice dynamics of nano-scaled samples is particularly challenging due to the usually low count rates during the inelastic scattering experiments. *In situ* nuclear inelastic scattering is a unique technique for the study of the lattice dynamics from bulk down to a monolayer and even sub-monolayer material coverage [62].

A multifunctional UHV system (Fig. 2.11) with a base pressure of 3×10^{-11} mbar is installed directly in the experimental hutch of the nuclear resonance beam line ID18 of the European Synchrotron Facility (ESRF). This chamber allows to grow and characterize nanostructures and to investigate them by *in situ* NRS methods. The sample preparation (MBE), characterization (electron diffraction) and measurements with X-rays at variable sample temperatures can be performed in this chamber [61]. All nuclear inelastic scattering experiments reported in this thesis are performed *in situ* and at a temperature of 100 K at this UHV system.

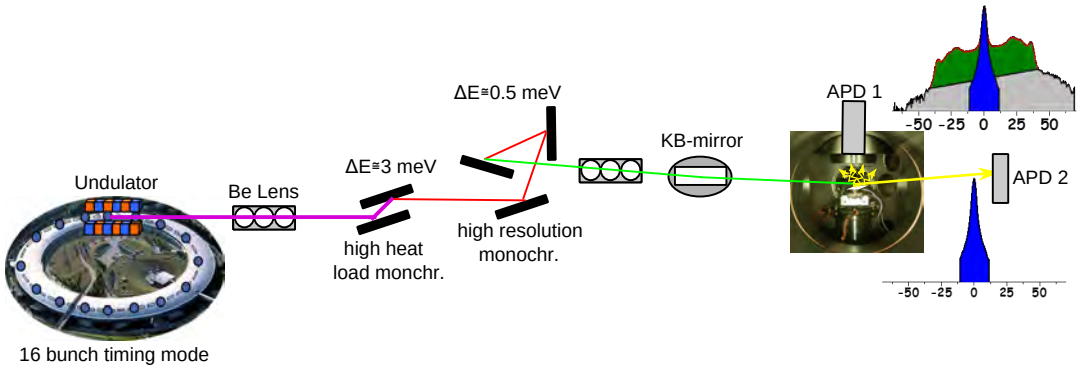

Figure 2.12.: Layout of the nuclear resonance beamline ID 18 of the ESRF in Grenoble/France [64]. The energy resolution of the *high heat load* monochromator is $\Delta E \cong 3\,\mathrm{eV}$, while the *high resolution* monocromator ensures $\Delta E \cong 0.5\,\mathrm{meV}$. The beam is collimated by a KB-mirror to a size of $10 \times 5\,\mu\mathrm{m}^2$ and hits the sample at a grazing incidence angle. The NFS signal and the instrumental function are measured by an avalanche photo diode (APD 2) in forward direction. APD 1 is detecting the NIS signal.

Nuclear resonant scattering experiments require a timing mode of the storage ring operation. The 16 bunch mode operation of the ESRF storage ring provides X-ray pulses with a length of 100 ps that are separated by time intervals of 176 ns. This mode combines the maximum possible photon flux with the bunch spacing of 176 ns for the measurement of the nuclear response. Fig. 2.12 describes the set up of the beam line ID 18 at the ESRF Grenoble/France. The beamline has a straight section equipped with three undulators. The beam is collimated by compound refractive lenses and monochromatized by a *high heat load* monochromator ensuring an energy resolution of $\Delta E \cong 3\,\mathrm{eV}$ [63].

An ultimate energy resolution of 0.5 meV can be achieved (Fig. 2.12) using high resolution monochromators [65]. This resolution is necessary for the performance of nuclear inelastic scattering experiments. A dedicated high resolution monochromator has to be designed for every isotope specific resonance energy. Currently, monochromators are available for the study of the isotopes ^{57}Fe, ^{119}Sn, ^{149}Sm, ^{151}Eu and ^{161}Dy.
The monochromatized X-ray beam is focused by a Kirpatrick-Baez (KB)-mirror [66] to a size of $10 \times 5\,\mu\mathrm{m}^2$ at the sample position. The sample is measured at grazing incidence geometry (Fig. 2.12). NIS spectra are obtained by avalanche photo diode (APD 1) (Fig. 2.12) mounted above the sample, while APD 2 (Fig. 2.12) is recording the instrumental function in forward direction. The latter is of crucial importance for the determination of the phonon DOS because the instrumental function has to be subtracted from the NIS spectrum for the evaluation of the data. NFS is measured by APD 2 (Fig. 2.12), that is an array of 4 APDs with a time resolution of about 0.1 ns (APD 2 Fig. 2.11) [67].

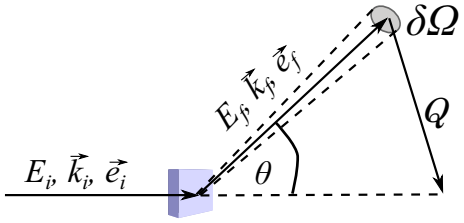

Figure 2.13.: IXS scattering geometry. The incident (i) and scattered (f) photons are characterized by the energy E, wavevector $\vec{k}$ and polarization vector $\vec{e}$.

2.4. Inelastic scattering of X-rays

Inelastic scattering of X-rays is one of the classical methods for probing phonon dispersion relations in solids. In this thesis it has been employed for the determination of the lattice dynamics of thick (bulk-like) films.

The inelastic scattering process of X-rays is outlined in Fig. 2.13. The energy and the momentum are conserved in the scattering process:

$$\vec{Q} = \vec{k}_i - \vec{k}_f \ , \tag{2.90}$$

$$E = E_i - E_f \ , \tag{2.91}$$

$$\vec{Q}^2 = \vec{k}_i^2 + \vec{k}_f^2 - 2k_i k_f \cos(\theta) \ . \tag{2.92}$$

θ is the scattering angle between the incident and the scattered photons with the wavevectors $\vec{k}_i$ and $\vec{k}_f$, respectively. The energy scale of phonon excitations (meV) is much smaller than the energy of the incident photons (keV) ($E \ll E_i$). Therefore, the following approximation for the wavevector transfer Q applies:

$$Q = 2k_i \sin\left(\frac{\theta}{2}\right) \ . \tag{2.93}$$

For inelastic X-ray scattering the momentum transfer is completely determined by the scattering angle.

The scattered intensity is described by the double differential cross section $\delta^2\sigma/\delta\Omega\delta E$, which is proportional to the number of incident probe particles, scattered within an energy range ΔE into a solid angle $\Delta\Omega$ [68]:

$$\frac{\delta^2\sigma}{\delta\Omega\delta E} = r_0^2(\vec{\epsilon}_i \cdot \vec{\epsilon_f})^2 \frac{k_i}{k_f} \sum_{I,F} P_I \left| \langle F| \sum_j e^{i\vec{Q}\vec{r_j}} |I\rangle \right|^2 \delta(E - E_f - E_i) \ , \tag{2.94}$$

with the classical electron radius r_0 and the coordinate of the jth electron $\vec{r}_j$. P_I corresponds to the thermal population of the initial state. The sum over the initial $|I\rangle$ and final $\langle F|$ states is the thermodynamic average. The cross section describes the process where a photon of the energy E_i, wavevector k_i and polarization $\vec{\epsilon_i}$ is scattered into a final state with the energy E_f, wavevector k_f and polarization $\vec{\epsilon_f}$.

The electron system changes from the initial state $|I\rangle$ to the final state $|F\rangle$. This expression already contains the *correlation function of the electron density*.
An expression of the *correlation function of the atomic density* is obtained by the application of the adiabatic approximation. Thus, it is possible to separate the ground state of the system to terms containing an electronic part (e), that depends only on the nuclear coordinates and a nuclear part (n), $|S\rangle = |S_e\rangle\,|S_n\rangle$. The second assumption is that during the scattering process the electronic part of the wave function is not changed, i.e., the difference in the initial $|I\rangle = |I_e\rangle\,|I_n\rangle$ and final states $|F\rangle = |I_e\rangle\,|F_n\rangle$ arises from atomic density fluctuations. Within these assumptions, the double differential cross section can be written as [68]:

$$\frac{\delta^2\sigma}{\delta\Omega\delta E} = r_0^2(\vec{\epsilon_i}\cdot\vec{\epsilon_f})^2\frac{k_i}{k_f}\left\{\sum_{I_n,F_n} P_{I_n}\left|\langle F_n|\sum_l f_l(\vec{Q})e^{i\vec{Q}\vec{R}_l}\,|I_n\rangle\right|^2\delta(E-E_f-E_i)\right\}. \quad (2.95)$$

$f_l(\vec{Q})$ is the atomic form factor of the atom l at the position $\vec{R}_l$. With the dynamical structure factor $S(\vec{Q},E)$, Eqn.(2.95) can be simplified to [68]:

$$\frac{\delta^2\sigma}{\delta\Omega\delta E} = \underbrace{r_0^2(\vec{\epsilon_i}\cdot\vec{\epsilon_f})^2\frac{k_i}{k_f}}_{(\delta\sigma/\delta\Omega)_{Th}}\left|f(\vec{Q})\right|^2 S(\vec{Q},E)\ . \quad (2.96)$$

The Thomson scattering cross section $(\delta\sigma/\delta\Omega)_{Th}$ is separated from the dynamical properties of the system. The atomic form factor $f(\vec{Q})$ is as a multiplicative factor and the structure factor $S(\vec{Q},E)$ can be expressed assuming one-phonon scattering by [68]:

$$S(\vec{Q},E) = \sum_j\left\langle n(E)+\frac{1}{2}\pm\frac{1}{2}\right\rangle(E_j(\vec{q}))^2F_{in}(\vec{Q})\ \delta(E\pm E_j(\vec{q})). \quad (2.97)$$

The phonon population is expressed by the Bose-factor $n(E)$ and the sum runs over the possible $3k$ phonon modes per unit cell. $\pm$ corresponds to phonon creation and annihilation. $E_j(\vec{q})$ is the energy of the phonon. The inelastic structure factor $F_{in}(\vec{Q})$ is proportional to the dot product of the phonon eigenvectors and the momentum transfer $\vec{Q}$, therefore $F_{in}(\vec{Q})$ is at its maximum when the direction of $\vec{Q}$ is along the phonon eigenvector. In summary, the phonons cause electron charge density variations, that directly can be observed by inelastic scattering of X-rays.

The phonon eigenvectors $\vec{e}_k^{\,j}(\vec{q})$ define the direction of the atomic vibrations as a function of the incident wavevector $\vec{q}$. Fig. 2.14 shows the two different vibrational modes. The longitudinal mode is connected to an atomic displacement parallel to the incidence vector ($\vec{e}_k^{\,j}||\vec{q}$) (Fig. 2.14 a)). The transverse mode is connected to an atomic displacement perpendicular to the direction of the wavevector ($\vec{e}_k^{\,j}\perp\vec{q}$) (Fig. 2.14 b)). The eigenvectors defined by these orientations are called polarization vectors. The corresponding scattering geometries for the detection of phonons are outlined in Fig.2.15. The scattering vectors in the (hk0)-plane of the reciprocal space are shown for the measurement of longitudinal (Fig. 2.15 a)) and transverse

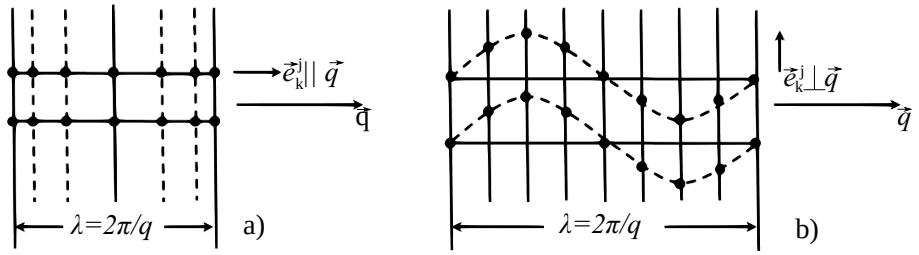

Figure 2.14.: a) Atomic vibrations in the main symmetry directions of a crystal with a) longitudinal b) transverse polarization in real space [69].

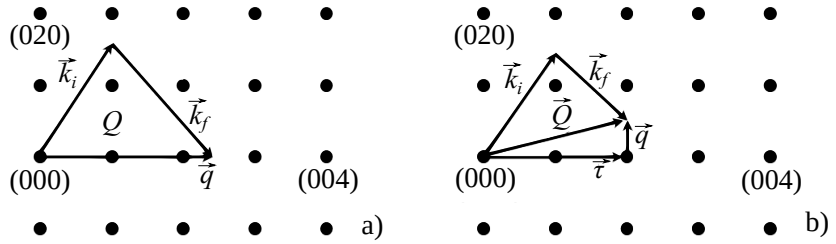

Figure 2.15.: a) Scattering geometry in the reciprocal space for the measurement of a) longitudinal b) transverse phonons in [100] direction.

(Fig. 2.15 b)) phonons in the [100] direction. The wavevector transfer $\vec{Q}$ (Eqn.(2.93)) is obtained by:

$$\vec{Q} = \vec{k_i} - \vec{k_f} = \vec{\tau} + \vec{q}\,, \tag{2.98}$$

with $\vec{q}$ the phonon wavevector with respect to $\vec{\tau}$, the nearest reciprocal point (Fig. 2.15). By choosing the wavevector transfer $\vec{Q}$ and the direction of the polarization vector $\vec{e}^{j}_{k}(\vec{q})$ the vibrational mode is selected. An energy scan with a specific wavevector transfer shows the creation and annihilation of phonons in the Stokes and anti-Stokes part, respectively.

2.4.1. Inelastic X-ray scattering at ID28/ESRF

The inelastic X-ray scattering experiments presented in this thesis are performed at the beamline ID28 of the ESRF Grenoble/France. The setup is schematically shown in Fig. 2.16. After the undulator source the beam is collimated by Be lenses and pre-monochromatized by a *high heat load* monochromator. The energy resolution of up to $\Delta E \cong 1\,\mathrm{meV}$ is achieved by a monochromator operating close to back-scattering geometry (Fig.2.16). The X-rays are focused by X-ray optics (compound refractive lenses CRL [71] and/or a KB-mirror [66]) at the sample position. A spherical silicon crystal analyzer in Rowland geometry is used for the energy analysis [69]. The wavevector transfer Q is chosen by the rotation of the analyzer arm in the horizontal plane. The wavelength of the X-ray is determined from Bragg's law ($n\lambda = 2d\sin(\theta)$) by the lattice planes d of the back scattering monocromator. An energy scan $E(\lambda)$ is done by changing the lattice constant d

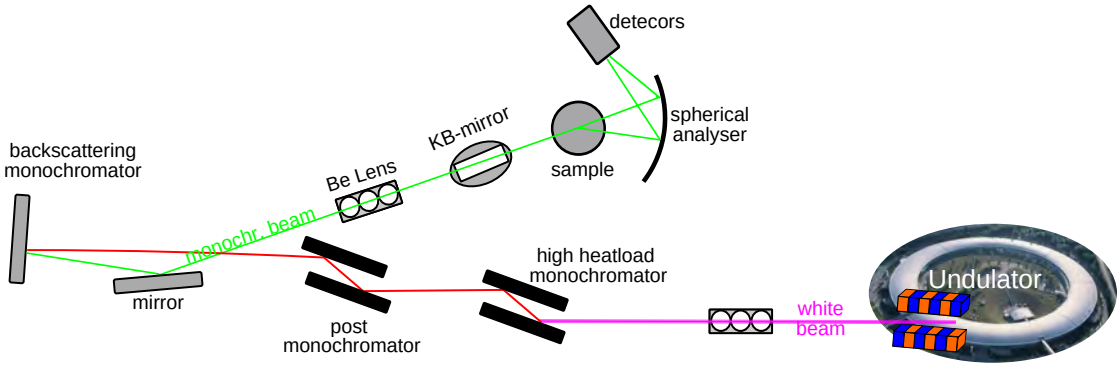

Figure 2.16.: Layout of the IXS beamline ID 28 ESRF Grenoble/France. Very high energy resolution can be achieved by a back scattering high resolution monochromator. The beam is focused by X-ray optics (Beryllium refractive lenses (Be) and a KB-mirror). A spherical Si crystal analyzer in Rowland geometry is used for the energy analysis [70].

of the Al_2O_3 crystal used as back-scattering monochromator by variation of its temperature with steps of $\Delta T = 0.5\,\mathrm{mK}$ while the temperature of the analyzer is kept at a constant temperature.

Preliminary information from theoretical models (Born von Krámán [31]), or from *ab initio* calculations on the lattice dynamics *prior* to the IXS experiments are indispensable. They predict the positions, directions and intensities of the phonon branches in the reciprocal space and therefore guide the experiment. An example for an energy scan performed in an IXS experiment is shown in Fig.2.17. The energy transfer ($E - E_0$ (E_0 corresponds to the analyzer)) is plotted against the intensity measured by the detector. Fig. 2.17 shows the Stokes part where the photon loses energy for phonon creation and the anti-Stockes part where the photon gains energy from annihilation of a phonon. The elastic peak (Thomson scattering) is centered around 0 energy transfer. The position of the peak (Stokes/anti-Stokes part) at a certain energy and the wavevector transfer $\vec{Q} = \vec{\tau} + \vec{q}$ define the measured point in the dispersion relation. In this way different branches of the phonon dispersion relations are obtained experimentally.

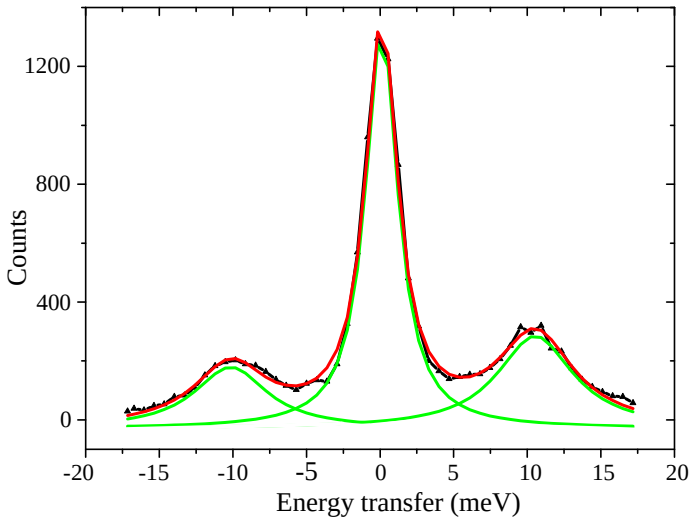

Figure 2.17.: Energy scan performed in an IXS experiment. The experimental data (black triangles and line) is shown with the best fit (red line). The individual components to the fit are shown with green lines. From left to right: anti Stokes peak, elastic peak and Stokes peak.

3. Sample growth and *in situ* characterization methods

The comprehensive investigation of the lattice dynamics requires the study of samples with high chemical and crystal phase purity as well as superior single crystalline quality. The following chapter describes the approach employed in this thesis to obtain high quality films and nanostructures of lanthanides and the in situ laboratory methods used for their characterization.

3.1. Sample growth

3.1.1. Molecular beam epitaxy

All samples investigated in this thesis were grown by molecular beam epitaxy (MBE). In MBE beams of atoms or molecules in ultra-high vacuum (UHV) environment are used as a source to provide the material on the surface of a single crystalline substrate. In UHV environment atoms and molecules travel in nearly collision free paths before arriving at the substrate surface or the walls of the chamber. The molecular beam is turned off almost instantaneously when a shutter is inserted between the source and the substrate. Therefore, it is possible, to grow films or nanostructures with low rates and very high precision of the amount of the deposited material. The substrate crystal is kept at a certain temperature, that provides sufficient thermal energy to the impinging atoms to migrate across the surface [72]. Crystal growth by molecular beam epitaxy is a kinetically driven process occurring through an oversaturation of the evaporated atoms in the gas above the surface of a suitable single crystalline and atomically clean surface [73]. Dependent on the lattice mismatch between the film/nanostructure and the substrate, the single crystalline nature of the substrate is adopted.
Evaporation of materials with melting temperatures of less than 1100 °C such as Europium, Samarium and Neodymium, is done from effusion cells equipped with Pyrolytic Boron Nitride (PBN) or Tantalum (Ta) crucibles. With these cells it is possible to achieve a constant beam flux of the evaporated material with a flux uniformity of 1% [74]. Metals and materials with higher melting temperatures such as Niobium, are evaporated from an electron beam evaporator. In this case high voltage is applied on a metal rod (target anode). Electrons emitted from a tungsten filament are accelerated by the electric field towards the target anode. These electrons bombard the metal rod, leading to the emission of a metal atom flux. A stable evaporation can be achieved with a flux electrode, measuring the electron flux between the target anode and the filament.

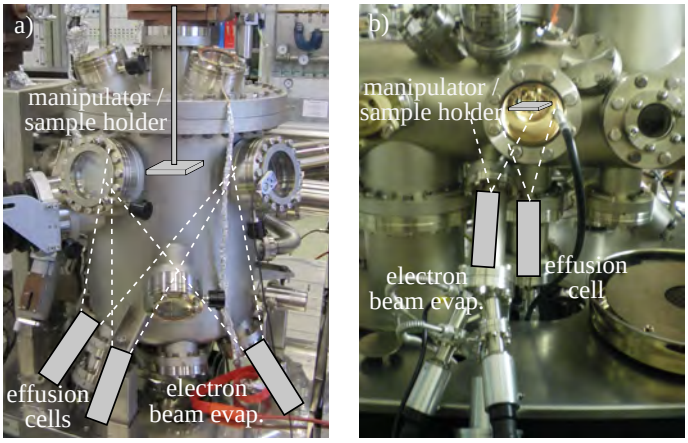

Figure 3.1.: a) The RE-MBE chamber in the UHV-analysis laboratory at the synchrotron light source ANKA of the Karlsruhe Institute of Technology. b) The sample preparation chamber of the UHV system for *in situ* nuclear resonant scattering experiments at the beamline ID18 at the ESRF Grenoble/France. The effusions cells and the electron beam evaporators are indicated.

The atoms or molecules evaporated from the source reach the substrate and interact with its surface. The atom is diffusing across the surface until it is adsorbed or desorbed. By adsorbtion, the atom is integrated into the surface structure, a step edge or nucleates into clusters, islands, wires or rods. Depending on the properties of the evaporant, the substrate and the available surface energy, three different growth modes can be distinguished [75]:

- *Franck-van der Merwe* or layer-by-layer growth mode: The formation of a new layer starts only after the previous layer is completed.
- *Vollmer-Weber* or island growth mode: The interaction between the deposited adatoms is stronger compared to the interaction with the surface, leading to the growth of three dimensional clusters and islands.
- *Stranski-Krastanov* is a combination of the layer-by-layer and the island growth modes: The transition between these two growth regimes depends on the crystallographic and physico-chemical properties of the substrate and the adatoms (lattice mismach, sufrace energies, chemical activity).

Which of the growth modes (or whether a combination between them) appears depends on many parameters such as the density of incident particles (deposition rate, vacuum conditions), the diffusion coefficient of the adatoms, substrate temperature and surface morphology (flat, vicinal or pre-patterned), lattice mismatch between the evaporant and the substrate, presence of defects on the substrate, chemical activity, etc. [73].

The sample growth, characterization and investigation of the nanostructures studied in this thesis are realized in two UHV systems:

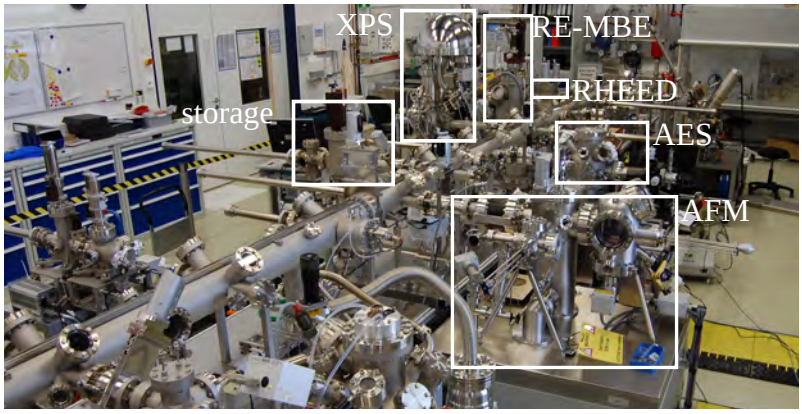

Figure 3.2.: Image of the UHV cluster at the UHV-Analysis laboratory located at ANKA/Karlsruhe Institute of Technology. The reflection high energy electron diffraction gun (RHEED) is installed in the RE-MBE chamber. Auger electron spectroscopy (AES), X-ray photoelectron spectroscopy (XPS) and UHV atomic force microscopy (AFM) are available in separate UHV chambers, connected to the UHV transfer line.

Fig. 3.1 a) shows the Rare Earth MBE chamber (RE-MBE) located in the UHV-analysis laboratory of the synchrotron light source ANKA at the Karlsruhe Institute of Technology. Two effusion cells and a 4-pocket electron beam evaporator are attached to this chamber. An electron gun for reflection high energy electron diffraction (RHEED) is mounted in the chamber. The fluorescent screen on the opposite side is used to visualize the diffracted electrons. The growth conditions for the samples are established in this chamber. Fig. 3.1 b) shows the MBE deposition chamber for sample preparation that is integrated in the UHV facility for *in situ* nuclear resonant scattering experiments at the beam line ID18 at the ESRF in Grenoble/France [61]. Attached to it are an effusion cell and a 4-pocket electron beam evaporator. The growth conditions established at the RE-MBE in Karlsruhe are applied in this growth chamber for sample preparation *prior* to the *in situ* experiments with synchrotron radiation.
The source flux distribution can be calculated assuming a cosine distribution with the peak intensity along the central axis of the effusion cell/electron beam evaporator [76]. For both chambers the flux homogeneity is calculated to be about ~1% for substrates with typical dimensions of $10\times10\,\mathrm{mm}^2$ used for all experiments. Both chambers have a base pressure of 3×10^{-11} mbar. The substrates can be heated up to 1373 K and cooled down to 100 K in both chambers.

UHV cluster at the UHV-Analysis laboratory at ANKA

The UHV cluster at the UHV-analysis lab at ANKA in Karlsruhe is a long ultra-high vacuum transfer system with a base pressure of 3×10^{-10} mbar, offering several docking stations for portable and stationary growth chambers and *in situ* characterization chambers (Fig. 3.2).
The sample characterization is performed with reflection high energy electron diffrac-

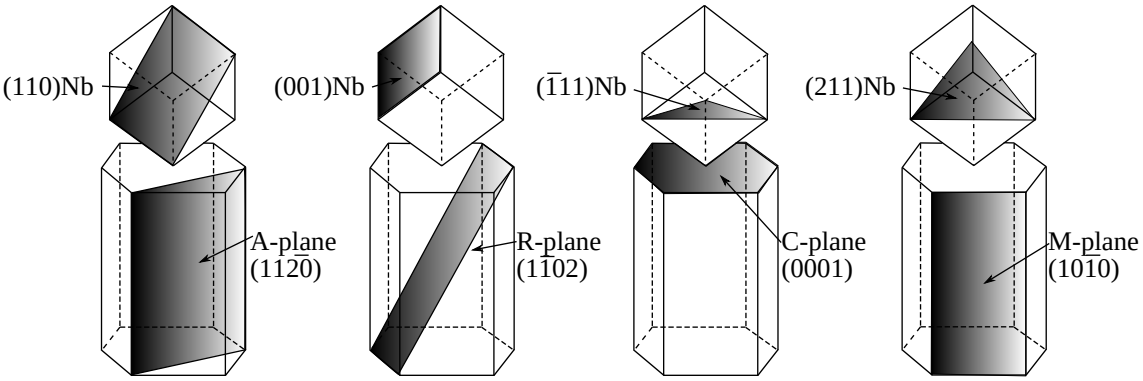

Figure 3.3.: Epitaxial relationship between Nb and Al_2O_3 for different substrate orientations [80].

tion (RHEED) installed in the RE-MBE chamber, Auger electron spectroscopy (AES), X-ray photoelectron spectroscopy (XPS) and UHV atomic force microscopy (AFM), available in separate UHV chambers connected to the UHV transfer line (Fig. 3.2).

3.1.2. Epitaxial growth of refractory metals on sapphire

The crystal structure of sapphire can be described by a hexagonal unit cell [77] (Fig. 3.3) with the lattice parameters $a = 4.7602\,\mathring{A}$ and $c = 12.9933\,\mathring{A}$. Refractory metals such as Nb, Ta and Mo grow epitaxially on different sapphire planes [20, 78, 79]. For example, Niobium grows epitaxially on several Al_2O_3 planes. Most common are the following four orientations (Fig. 3.3) [80]:

- (110)Nb || (11$\bar{2}$0)Al_2O_3 A-plane,
- (001)Nb || (1$\bar{1}$02)Al_2O_3 R-plane,
- ($\bar{1}$11)Nb || (0001)Al_2O_3 C-plane,
- (211)Nb || (10$\bar{1}$0)Al_2O_3 M-plane.

All elements from the *V* B and *VI* B group of the periodic table exhibit an almost negligible chemical reactivity with pure lanthanides [81]. The metal of choice for the buffer layer for all samples investigated in this thesis is Nb grown on A-plane sapphire, since several studies demonstrated the successful epitaxial growth of lantanides with a hexagonal structure on the (110)Nb surface [78, 82].
A-plane sapphire substrates with the dimensions $10 \times 10\,mm^2$, purchased from MaTecK GmbH, are characterized with a surface miscut of $\pm 0.5°$ or smaller and a root mean-square surface roughness on the order of 0.35 nm. The substrates are cleaned by a solvent degreasing treatment in an ultrasonic bath and afterwards annealed under UHV conditions for 1 h at 1073 K, after an elaborated cleaning procedure adopted from Doufur *et al.* [82, 83]. Fig. 3.4 (left) shows a RHEED image along the [$\bar{1}$100] azimuth. The high crystalline quality of the substrate is confirmed

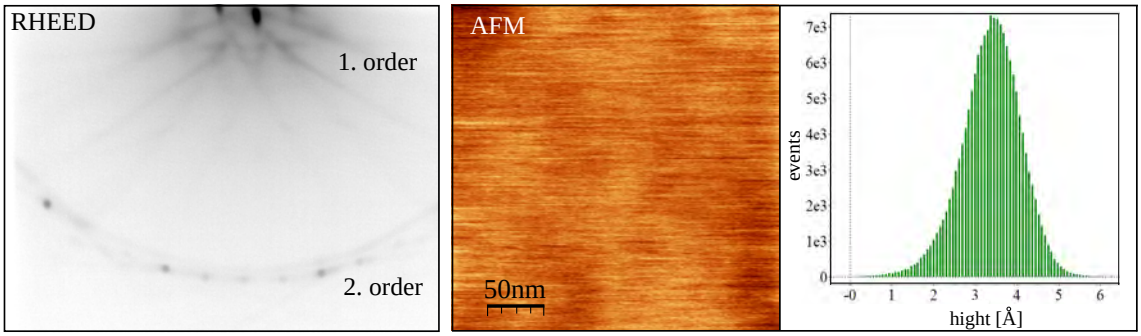

Figure 3.4.: Left: RHEED image obtained along the $[\bar{1}100]$ azimuth of a clean $(11\bar{2}0)$ Al_2O_3 surface. The first and second order high intensity diffraction peaks indicate a smooth single crystalline surface. Middle: AFM image from the same surface. Right: The analysis reveals a roughness of the order of 0.35 nm.

by sharp spots of the first and second order. Atomic force microscopy investigations of a clean $(11\bar{2}0)$ substrate confirm a surface roughness of about 0.4 nm (Fig. 3.4 (right)).
The deposition of Nb on sapphire can be described by a layer-by-layer growth, or by the so called step-flow model. This model describes the layer-by-layer growth on vicinal (miscut) substrates, where the deposited overlayer nucleates at the steps of the surface [80]. A systematic RHEED study of the Nb growth as a function of the substrate temperature is performed by Orderno *et al.* [84]. In the first stages of the Nb growth, a film of hexagonal structure is formed in a temperature range between $553\,\mathrm{K} < T < 1093\,\mathrm{K}$ on the $(11\bar{2}0)$ Al_2O_3 surface (Fig. 3.5). The temperature

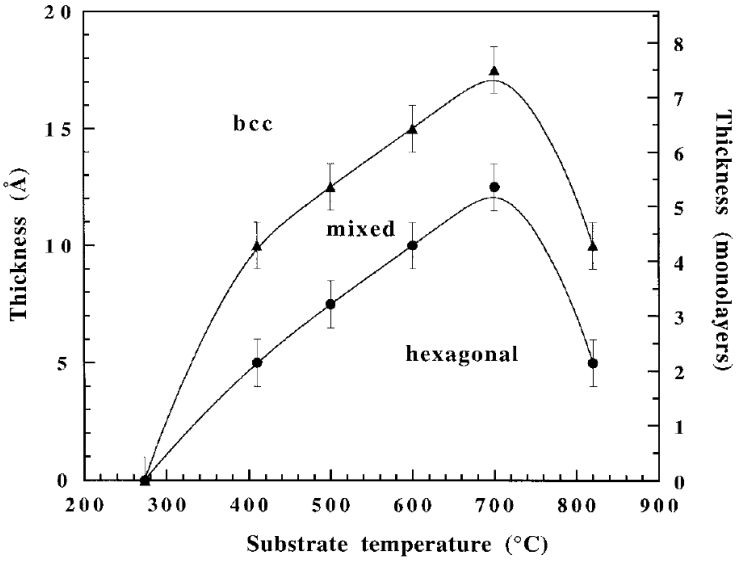

Figure 3.5.: The temperature-thickness phase diagram of the Nb deposit on A-plane sapphire. At low Nb coverages a hexagonal film forms in the temperature range $553\,\mathrm{K} < \mathrm{T} < 1093\,\mathrm{K}$ (taken from [84]). For coverages higher than 1.7 nm the growth continues in the *bcc* phase.

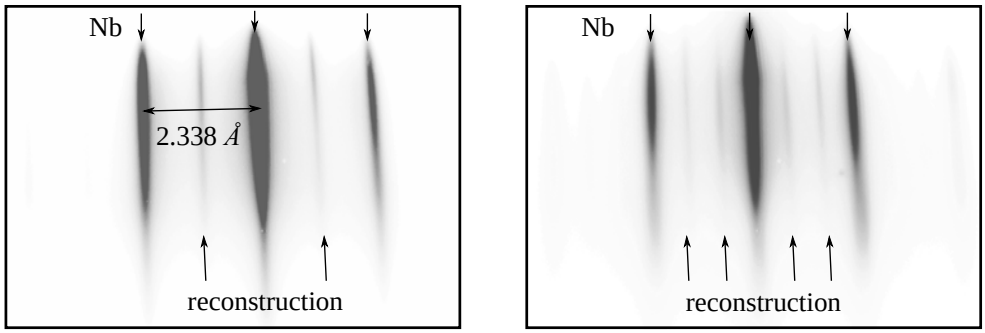

(a) [001]-azimuth **(b)** 111-azimuth

Figure 3.6.: RHEED images along the a) [001] azimuth b) [111] azimuth of the (110) Nb surface. The inner streaks with low intensity appear due to the oxygen induced reconstruction at the surface.

dependence of the structure is shown in Fig. 3.5. With increasing thickness of the Nb deposit, a gradual transition to the native *bcc* structure of niobium occurs within this temperature range. The *bcc* structure continues to grow for coverages higher than 1.7 nm.

A detailed study of the crystalline quality and the surface morphology of the (110)Nb layer grown on Al_2O_3 was performed by Wildes *et al.* [80]. A strong influence of the film thickness and the substrate temperature on the crystalline quality, surface roughness and surface lattice constant was found in the temperature range $573\,\mathrm{K} \leq T_S \leq 1173\,\mathrm{K}$. These studies reveal that Nb films grown at substrate temperatures (T_S) $T_S \geq 1073\,\mathrm{K}$ and film thicknesses $d \geq 25\,\mathrm{nm}$ exhibit high single crystalline quality, smooth surface and relaxed lattice constant [80]. Therefore, the growth parameter for all (110) Nb buffer layers are chosen to be $T_S = 1173\,\mathrm{K}$ and $d = 25\,\mathrm{nm}$. A strong dependence of the Nb surface on the surface morphology of the Al_2O_3 substrate miscut has been reported [85]. The Nb layer of a thickness of $\sim 20\,\mathrm{nm}$ exhibits very small features (large smooth terraces) with small pits on Al_2O_3 substrates with a small ($\sim 0.2°$) miscut . For substrates with higher miscut ($\sim 0.7°$), long features (*fingers*) are formed at the Nb film surface [86].

A surface reconstruction is found on the (110)Nb surface at substrate temperatures higher than $T_S \geq 723\,\mathrm{K}$. Sürges *et al.* [87] report that diffused oxygen from the substrate is responsible for the formation of an oxygen induced surface reconstruction. The results have been reproduced in the present study. The RHEED images in Fig. 3.6 of a 25 nm thick Nb buffer layer grown at $T_S = 1073\,\mathrm{K}$ show the oxygen induced reconstruction as additional low intensity streaks between the high intensity main streaks of (110)Nb. These additional streaks are visible along both azimuths (Fig. 3.6a) ,b)). A similar surface reconstruction is reported for the (110)V surface, when annealed at temperatures higher than $T_S \geq 723\,\mathrm{K}$ [20].
The atomic configuration on the surface can be concluded from the RHEED study. The possible configuration of the reconstruction on the (110)Nb surface in reciprocal and real 2D space is shown in Fig. 3.7 a) and b), respectively. This

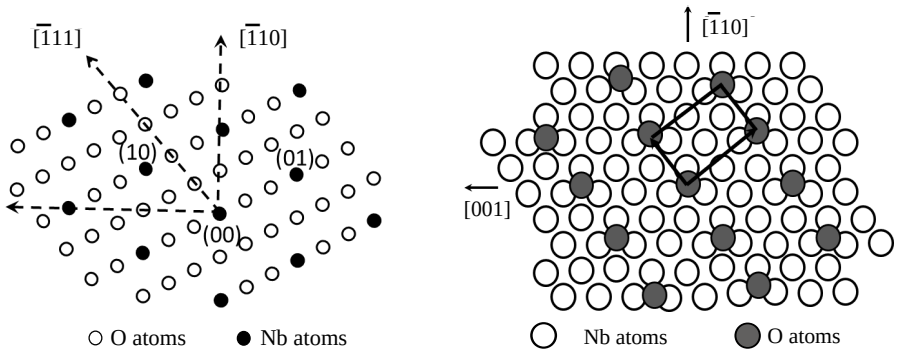

(a) reciprocal space **(b)** real lattice

Figure 3.7.: a) The lattice in two dimensional reciprocal space derived from the RHEED patterns in Fig. 3.6. The (110)Nb surface (black circles) is indexed with the primitive unit cell. The open circles represent the positions of the fractional-order streaks. b) A possible superstructure (gray circles) on the (110)Nb surface (white circles) in real space estimated from the corresponding reciprocal space, suggested by Süergers *et al.* [87].

reconstruction is described either by $c(2 \times 2)$ [87] or by $c(6 \times 2)$ [18, 88].

The horizontal inter streak distance in the RHEED image along the [001]-azimuth (Fig. 3.6 a)) corresponds to a horizontal lattice spacing of $\sqrt{2}a_{Nb}/2 = 2.338\,\mathring{A}$, with $a_{Nb} = 3.307\,\mathring{A}$ being the lattice constant of Nb [80]. Even though the exact nature of the reconstruction is still under debate [89], the distance between the main streaks can be used as a reference for the estimation of lattice constants of epitaxial rare earth nanostructures grown on the (110) Nb surface [80].

3.1.3. Growth of rare earth metals on refractory metal surfaces

The epitaxial growth of RE metals on the surfaces of some transition metals (TM) has extensively been studied. Prominent examples are RE/W [90, 91], RE/Mo [92], RE/Nb [78], and RE/V [93, 94]. These studies demonstrate that for all lanthanide metals with *fcc*, *hcp*, *dhcp* or *Sm-type* structures two orientations with respect to the (110)TM surface are possible. In the Nishijama-Wassermann (NW) orientation relationship, the close-packed rows of $\langle 110 \rangle$ of the *fcc* or $\left\langle 11\bar{2}0 \right\rangle$ of the *hcp* lattice are parallel to the $\langle 100 \rangle$ rows of the (110) *bcc* surface. In this case, the epitaxy is of the type m:n with m the rare earth and n the transition metal [95].

In the Kurdjumov-Sachs (KS) orientation relationship, the RE $\langle 110 \rangle$ rows are aligned parallel to the $\langle 111 \rangle$ rows of the (110) *bcc* TM surface. A sketch of the NW and KS orientation relationships is shown in Fig. 3.8. Hexagonal based rare earth metals adopt the NW-type orientation relationship with respect to the (110) TM surface.
Europium exhibits the *bcc* structure and is therefore an exception. However, the

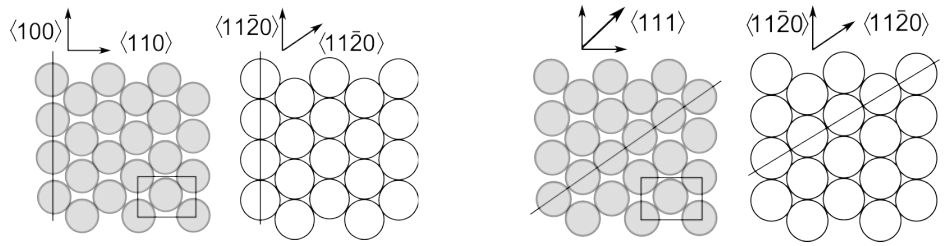

(a) NW:⟨100⟩ ∥ ⟨11$\bar{2}$0⟩ **(b)** KS:⟨111⟩ ∥ ⟨11$\bar{2}$0⟩

Figure 3.8.: *hcp* or *fcc* overlayer (white circles) on a *bcc* (110) surface (gray circles) for the a) Nishiyama-Wassermann and b) Kurdjumov-Sachs orientations [75].

epitaxial growth of hexagonal Eu films on (110)TM surfaces is reported (Eu/Ta [19], Eu/W [21], Eu/Nb [18]). In all studies, epitaxial hexagonal Eu films are formed in the submonolayer range following the NW orientation relationship. A systematic study of the formation of the initial Eu phase is performed in the scope of this thesis and is discussed in detail in chapter 5. In all cases, an increase of the Eu coverage leads to a relaxation of the phases to (110) Eu domains adopting the KS orientation relationship [18, 19].

3.2. *In situ* surface characterization methods

All films and nanostructures grown and investigated in this thesis are characterized by *in situ* laboratory methods such as AFM, RHEED and XPS. The working principles of this methods are briefly outlined below.

3.2.1. Atomic force microscopy

The surface morphology of the studied samples is investigated by contact and noncontact atomic force microscopy (AFM). A sharp tip is moved across a surface by one or more piezo motors. In contact AFM mode the tip is pressed with a constant force onto the sample surface. The height of the tip is adjusted keeping the applied force constant when the tip moves over the structures on the surface. The position (height) of the tip is mapped by a laser and detected by a detector. The danger of destruction or material removal exists in the case of soft material. To avoid such effects, the AFM is used in noncontact mode. In this mode an oscillation is applied on the tip. The oscillation frequency changes, depending on the distance to the surface. In this way images of the surface topography can be generated without the contact between tip and surface.
The acquired data sometimes does not correspond to the real surface features because experimental artifacts may appear. These artifacts have to be taken into account when the AFM results are examined. The structure visible in the AFM images is always a convolution between the size and shape of the tip and the nanostructure [96]. Fig. 3.9 a) shows the case of the tip radius R being smaller than the

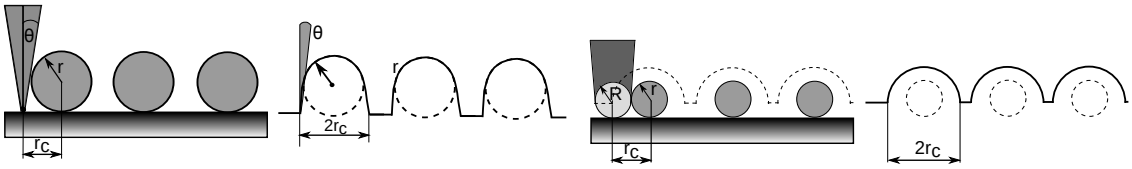

(a) $R \ll r$ **(b)** $R \approx r$

Figure 3.9.: a) Left: Tip and objects, Right: Image profile of objects for the case $R \ll r$ b) Left: Tip (R) and objects (r), Right: Image profile of the objects for the case $R \approx r$. r_c is the radius of the object in the image profile.

feature radius r, $R \ll r$ and Fig. 3.9 b) the case of $R \approx r$. In both cases, the height is not affected by the tip radius R. In case $R \approx r$, the AFM image of the object shows approximately a radius $r_c = R + r$ for the lateral width (Fig. 3.9 b)).

The AFM studies done within the scope of this thesis are performed using noncontact super sharp silicon tips (sss-nch NanoWorld). These tips are characterized by a typical tip radius $R = 2\,\text{nm}$ and half cone angle $\theta < 10°$. The influence of the tip was taken into account when size and shape of the nanostructures were evaluated from the AFM images.

3.2.2. Reflection high energy electron diffraction

RHEED is an *in situ* technique for the real time study of the crystallographic structure of films and nanostructures during growth, for example, by molecular beam epitaxy. Electrons are emitted from a tungsten filament inside the RHEED gun. These electrons are accelerated in a potential of 30 keV (RHEED Gun RHD-30, Specs), forming an electron beam. The wave length of the electrons can be calculated from the de Broglie relation and the relativistic expression of the kinetic energy: $\lambda_{electron}(30\,\text{keV}) = 0.0698\,\mathring{A}$. The electron beam hits the sample surface at a grazing angle of about $1 - 3°$ (Fig. 3.10 a)). The diffracted electrons are detected on a fluorescent screen. The image on the fluorescent screen is recorded by a digital camera. Depending on the morphology of the surface, diverse diffraction patterns may appear, as sketched in Fig. 3.10. In the case of a perfectly flat crystalline surface, the intersection of the Ewald's sphere with the crystal truncation rods [97] results in the formation of spots on a ring (Fig. 3.10 b)). If the surface shows atomic roughness, steps or a wavy structure, vertical streaks are visible on the fluorescent screen. In this case, the truncation rods are broadened and the intersection with the Ewald's sphere is larger and appears as streaks (Fig. 3.10 c)). In the case of island growth on the surface, the electrons are diffracted in Laue geometry and diffraction spots emerge on the screen (Fig. 3.10 d) [97]. The in-plane lattice constant and the crystal structure can be derived from a systematic RHEED study. The scattered beam obeys the Bragg's law ($2d \sin\theta = n\lambda$). Since the radius of the Ewald's sphere is large and the angles, where the diffraction conditions are fulfilled are small, the following approximation holds:

$$2\sin\theta = \tan 2\theta = \frac{D}{L}, \tag{3.1}$$

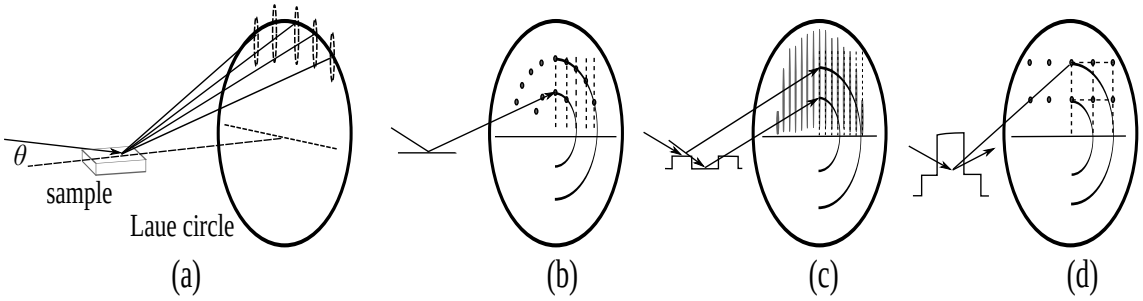

Figure 3.10.: a) RHEED geometry. The incidence angle θ is $1-3°$. Depending on the surface morphology different diffraction patterns are detected on the fluorescent screen; b) perfect crystalline surface: single sharp spots on a circle; c) atomic roughness, a stepped or wavy surface: "vertical" streaks; d) island (3D growth): diffraction pattern formed by transmitted electrons.

where D is the distance between the streaks measured directly on the fluorescent screen and L the distance between the sample and the screen. The angle θ is sketched in Fig. 3.10 a). From this approximation the lattice spacing d_{hkl} is calculated by:

$$d_{hkl} = \frac{L \cdot \lambda}{D}, \tag{3.2}$$

with λ, the wavelength of the electrons. The constant $L \cdot \lambda$ has to be determined in a calibration experiment with a sample of known lattice spacing d_{hkl}. A way to circumvent the determination of the absolute value of L is to determine the lattice spacing from the comparison with a known lattice spacing. The values of the sample (D, d_{hkl}) and the calibration sample (D', d'_{hkl}) can be compared by:

$$\frac{d_{hkl}}{d'_{hkl}} = \frac{D'}{D}. \tag{3.3}$$

It can be shown that the full width half maximum of the diffracted streak pattern on the fluorescent screen is inversely proportional to the size of the terraces of a stepped surface [98]. Therefore, the terrace size can be as well estimated from Eqn.(3.3). In the case of epitaxial islands, a transmission electron diffraction image is visible on the screen [97]. The diffraction spots can be indexed and the in-plane and out-of-plane lattice parameter is obtained. This method is used to determine the crystallographic structure of the Eu islands in section 5.2.3.

3.2.3. X-ray photoelectron spectroscopy

X-ray photoelectron spectroscopy (XPS) is a technique for the investigation of chemical and electronic properties of surfaces and can be used to derive the elemental composition of the sample [99].

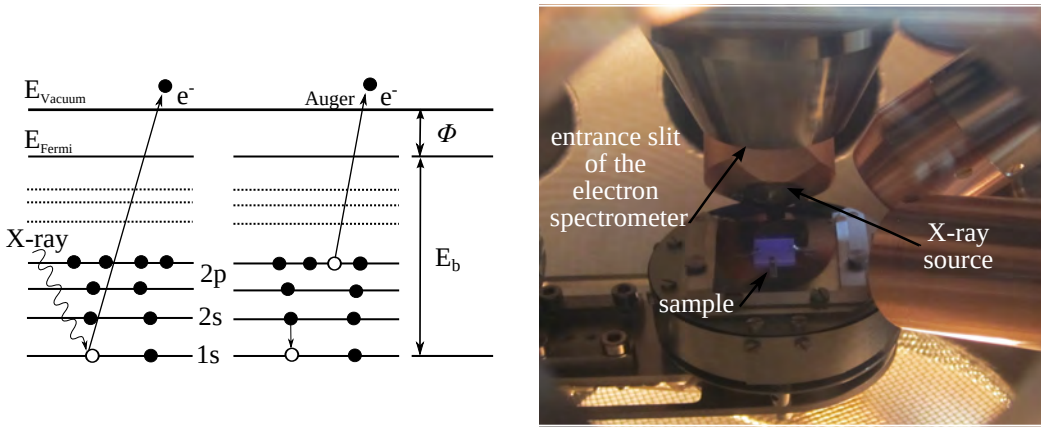

Figure 3.11.: a) Sketch of the X-ray photoelectron and Auger electron process: The emission of an electron from the 1s shell of an atom (left) and the process of Auger electron emission (right), where the filling of an inner-shell vacancy of an atom occurring after the excitation by an X-ray, is accompanied by the emission of an electron from a higher shell of the same atom. b) Photograph of the interior of the XPS-chamber at the UHV-Analysis laboratory at ANKA with the X-ray source in a 45° angle towards the sample and the entrance of the electron spectrometer above.

XPS is based on the photoelectric effect. The sample is irradiated by X-rays of distinct energy, e.g., Al K_α ($h\nu = 1486.6\,\mathrm{eV}$) or Mg K_α ($h\nu = 1253.6\,\mathrm{eV}$). As a result of the photoemission or Auger process, electrons escape from the surface with a certain kinetic energy. Their energy is analyzed by a spectrometer and the number of electrons within a kinetic energy interval is recorded [99].
Due to the conservation of energy before and after photoemission, the photoelectron has a kinetic energy of:

$$E_{kin} = \hbar\omega - E_b - \Phi, \tag{3.4}$$

with the energy of the incident photon $\hbar\omega$, binding energy of the electron E_b, and the workfunction Φ of the material. By a suitable callibration of the spectrometer all quantities in Eqn.(3.4) can be measured relative to E_{Fermi} (Fig. 3.11 a)) and Φ can be eliminated from the equation. The basic principle of the photo electric and Auger-electron effect are schematically sketched in Fig. 3.11 a). A (photo)electron from the 1s shell of an atom is emitted due to the excitation by an X-ray. The filling of an inner-shell vacancy of an atom, following the excitation by an X-ray, can be accompanied by an emission of an electron from the same atom but from a higher shell. This process is called the emission of an Auger electron (Fig. 3.11 a), right) and is visible in the XPS spectrum.
Each element has a characteristic XPS spectrum due to its specific electronic structure exhibiting peaks that are characteristic for the bound electronic states of electrons from the atom species at the sample surface.

All XPS measurements in this thesis were performed with the XPS instrument

(SPECS) located in the UHV-Analysis laboratory at ANKA using the Mg K_α radiation with the energy E=1253.6 eV. The configuration of the X-ray source and the electron analyzer is shown in Fig. 3.11 b).
The potential seen by an electron is affected by neighboring atoms, by their arrangement, number and species and existing chemical bonds. If the environments for atoms of the same element are different, their electron binding energies are shifted relative to each other. A real spectrum consist of peaks, which are the sum of all contributions (bulk, surface, different chemical states), convoluted with the instrumental function describing the X-ray source and the electron analyzer of the XPS system [99].

XPS data evaluation: It is possible to determine relative ratios of the elements contained within the probing volume from the relative intensities of the XPS lines. The XPS line intensities are proportional to [99]:

$$I(Z, N, h\nu, E_{kin}, d) \propto \sigma(Z, N, h\nu) T(E_{kin}/E_{pas}) \int_0^d c(Z, x) e^{-x/\lambda(E_{kin})} dx, \qquad (3.5)$$

with:
c : Depth dependent concentration distribution of the element Z,
N : Core level,
d : Thickness of the layer,
λ : Energy dependent (E_{kin}) inelastic mean free path of the electrons,
σ : Absorption cross section for the transition,
$h\nu$: Energy of the X-ray,
T : Transmission function of the electron analyzer,
E_{kin} : Resulting kinetic Energy of the photo electron,
E_{pas} : Transmission energy of the electron analyzer.

The cross sections used in this work for the analysis of the XPS data were taken from [100], while λ was taken from the universal curve [101]. The integral is evaluated in the regions of constant element concentrations assuming a layer system.

Part II.

Results and Discussions

4. Lattice dynamics of bulk rare earth metals

In order to investigate the lattice dynamics of bulk Sm type Sm, dhcp Sm and dhcp Nd which were unknown until now, bulk-like single crystalline films were grown by MBE and characterized by diffraction of X-rays and electrons. The Sm type structure of the film was additionally fully confirmed by a temperature dependent NFS study in the interval $4-120\,K$*. The lattice dynamics was determined by nuclear inelastic scattering (Sm type Sm) and inelastic X-ray scattering (dhcp Sm, Nd) and is compared to the results from first principle calculations. The thermodynamic and elastic properties of these metals relevant to the lattice dynamics were determined.*

4.1. Samarium

Introduction

Samarium is certainly one of the most fascinating elements across the periodic table. At ambient conditions, Sm exhibits the so called *Sm type* structure, characterized by a rhombohedral unit cell with a stacking of nine layers. The heavy lanthanides Gadolinium to Lutetium as well as Yttrium, Lithium and Sodium also form this exotic crystal structure at high pressure (Gd-Lu, Y [75]) or at low temperatures (Li [102] and Na [103]).

The unit cell of the *Sm type* structure is characterized by a periodic stacking of nine close packed planes along [0001] with two sublattices with hexagonal (h) and cubic (c) symmetry with a ratio 2:1 [104] and the sequence $A_cB_hA_hB_cC_hB_hC_cA_hC_hA_c$ [105] (Fig. 4.1). The *Sm type* structure is an intermediate between the double hexagonal close packed (*dhcp*) – with the stacking $A_cB_hA_cC_hA_cB_hA_cC_h$– and the hexagonal close packed (*hcp*) – with the stacking $A_hB_hA_hB_h$ – lattices exhibited by light and heavy lanthanides, respectively.
Magnetic moments on the hexagonal site order antiferromagentically below $T_{Neél} = 106\,\mathrm{K}$ [106]. Calculations done by Moon and Köhler [107] revealed strong exchange interactions between the atoms located at the hexagonal sites that explain their high ordering temperature. In the basal plane, the magnetic moments couple ferromagnetically. The coupling is antiferromagnetic along the c-axis in the sequence (0++0–0++0–...) [106]. Zero corresponds to the paramagnetic cubic planes at $T = 106\,\mathrm{K}$. The cubic sublattice orders antiferromagnetically below $T = 14\,\mathrm{K}$ with the magnetic unit cell being four times larger than the chemical unit cell in the c and a-axis. This complex magnetic structure is caused by the long range order

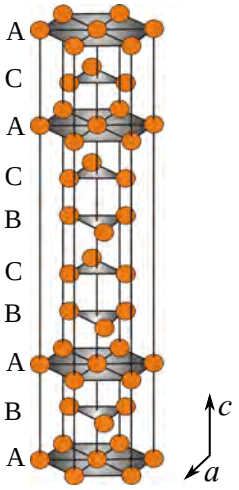

Figure 4.1.: Rombohedral $9R$ unit cell of *Sm type* Sm with the stacking sequence $A_cB_hA_hB_cC_hB_hC_cA_hC_hA_c$. It satisfies $R3m$ symmetry with three atoms per unit cell.

coupling of the $4f$ moments and crystal field effects [107]. Temperature dependent investigations of the hyperfine interactions of a polycrystalline foil by NFS from Barla *et al.* [108] reveal that at $T = 3\,\mathrm{K}$ a combination of magnetic hyperfine and electric quadrupole interactions with $B^h = 344(5)\,\mathrm{T}$ and the quadrupole interaction $E_Q^h = -1.80(3)\,\mathrm{mm/s}$[1] for the hexagonal site and $B^c = 317(5)\,\mathrm{T}$ and $\Delta E_Q^c = -1.51(3)\,\mathrm{mm/s}$ for the cubic site exist.

4.1.1. Sample growth and characterization

The investigation was conducted on a 500 nm thick Sm film in order to ensure bulk properties of the sample. The (0001)Sm film was grown in the preparation chamber of the UHV system of ID 18 at the ESRF in Grenoble, following the growth procedure described by Dumesnil *et al.* [109]. The treatment of the A-plane Al_2O_3 substrate was described in chapter 3.1.2. The (110)Nb buffer layer was deposited from high purity (99, 9%) Nb (Goodfellow) with a rate of 1.5 Å/min at a substrate temperature of $T_S = 1173\,\mathrm{K}$. High-purity (99.99 %) vacuum-outgassed Sm, supplied by Ames laboratory, was evaporated from an effusion cell with a rate of 30 Å/s on the surface of the 25 nm thick buffer layer, while the substrate was kept at 373 K. During all evaporation steps the pressure in the chamber did not exceed $5 \times 10^{-10}\,\mathrm{mbar}$.
The sample was transferred to the chamber for the *in situ* NIS and NFS experiment. The X-ray beam was monochromatized by crystal optics optimized for a photon energy of E=22.5015(5) keV with an energy resolution of 1.1 meV at full width half maximum (FWHM) [49, 110]. The pressure during the experiment was $3 \times 10^{-10}\,\mathrm{mbar}$ or lower. During the measurement the film was kept at $T = 111\,\mathrm{K}$ in order to reduce the contribution of multi-phonon excitations. After the NIS experi-

[1] $\Delta E_Q = eV_{zz}Q_g$,
Q_g is the nuclear quadrupole moment of the ground state with $I_g = 7/2$.

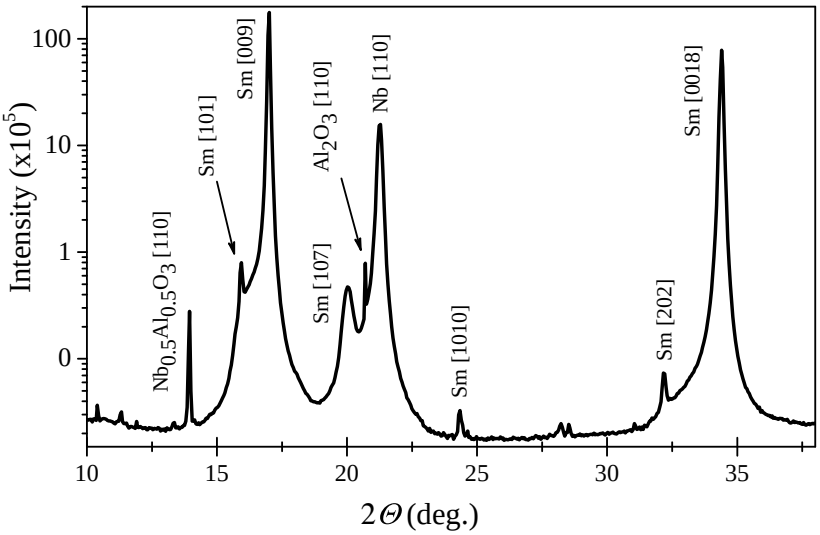

Figure 4.2.: X-ray diffraction scan on the single crystalline Sm film. The data is measured at a wavelength of $\lambda = 0.8602\,\mathring{A}$. The peaks indicate a high quality sample with the main reflections [0009] and [00018] of the *Sm type* structure. The low intensity peaks are found to belong to a polycrystalline fraction of Sm of less than 0.8 % and the peaks from the single crystalline Nb buffer layer [111].

ment, the sample was covered with a 6 nm thick Nb layer to prevent the Sm metal from oxidation.

To verify the quality of the investigated sample an *ex situ* X-ray diffraction (XRD) study was performed on the covered Sm film. The diffraction pattern shown in Fig. 4.2 confirms the high crystalline quality of the sample. The strongest peaks arise from [0009] and [00018] reflections of the *Sm type* structure. The low intensity peaks are found to belong to the single crystalline Nb buffer layer. The smallest peaks indicate a fraction of polycrystalline Sm of less than 0.8 %.

Temperature dependent hyperfine interactions

Additionally to the XRD experiment, the formation of the *Sm type* structure was investigated by a temperature dependent NFS study. The NFS experiment was performed at grazing incidence geometry in the temperature range $4 - 120\,\mathrm{K}$, that covers the Neél temperatures of the hexagonal and cubic sites.

The experimental data was consistently analyzed by the program REFTIM [57, 58], setting the isomer shift, magnetic field and electric field gradient and the corresponding angles (section. 2.3.1) as fit parameters. The nuclear parameters characterizing the ^{149}Sm Mössbauer transition used in the REFTIM input files are listed in Table 4.1. The specific X-ray properties of the materials are taken from the X-ray data

Table 4.1.: Nuclear properties of ^{149}Sm, used for definition of the ^{149}Sm Mössbauer transition in the input files for fits of the NFS data with REFTIM (with the nuclear magneton $\mu_N = 5.058 \cdot 10^{-27}$J/T and 1 barn= 10^{-28} m^2, is the ground (g) and the excited (ex) state). The values are taken from [34, 36].

^{149}Samarium	parameter	value
isotope mass	M	$149\,u$
natural abundance	β_{nat}	13.8%
transition energy	E_0	22501.5 eV
wavelength	λ_0	0.5511 $\mathring{A}$
recoil energy	E_R	1.82 meV
lifetime	τ	10.27 ns
halflife	$\tau_{1/2}$	7.12 ns
natural width	Γ_0	64.1 neV
internal conversion coefficient	α	29.2
nuc. ang. moment	I_g	$^-7/2$
	I_{ex}	$^-5/2$
resonance cross section	σ_0	120.1 kbarn
electronic cross section	σ_{el}	6.94 kbarn
transition multipole character	$M1 + E2$	M1 dominant
nuc. quadrupole moment	Q_g	0.075 barn
	Q_{ex}	1.01 barn
nuc. magnetic moment	μ_g	$-0.672\,\mu_N$
	μ_{ex}	$-0.625\,\mu_N$

booklet [112]. According to [113] the used definition for the *EFG* is:

$$\Delta E_Q = \frac{eV_{zz}Q_{ex}}{2}. \tag{4.1}$$

with V_{zz} the electric field gradient tensor and Q_{ex} the quadrupole moment of the nuclear exited state. The NFS spectra are fitted with a model assuming a Sm layer containing sites with hexagonal and cubic symmetry with the ratio 2:1, that is the *Sm type* structure. Both have their own set of hyperfine interaction parameters, which were fit parameters: magnetic field $\vec{B}$ with corresponding angles (θ, ϕ), electric field gradient *EFG* and the isomer shift *IS*. In the program package REFTIM, a symmetric *EFG* is assumed implying that $\eta = 0$ in Eqn.(2.50). Fig. 4.3 depicts the geometry used by the program. The main axis of the *EFG* is set to coincide with the quantization axis of the magnetic field $\vec{B}$. The orientation of the magnetic field is defined by the scattering plane that is determined by the direction of the incidence vector $\vec{k}_0$ and the normal of the sample surface. The incidence angle is set to the experimental value $\alpha_{in} = 1.56$ mrad. α_{in} is defined as the angle between the sample surface and the incidence vector $\vec{k}_0$. Fig. 4.4 shows selected NFS spectra with the fits derived from the described model revealing a remarkable agreement between experiment and theory. The data analysis shows that the magnetic field

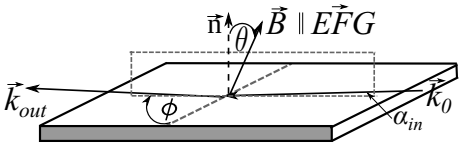

Figure 4.3.: Geometrical configuration used in REFTIM to analyze the experimental NFS data. The angles are defined according to the scattering plane determined by the direction of the incidence vector $\vec{k}_0$ and the normal of the sample surface. In the case of $\theta = 90°$ and $\phi = 90°$, the magnetic hyperfine field is oriented along the scattered beam in the surface plane of the sample. The *EFG* is assumed to be symmetric $\eta = 0$ (Eqn.(2.50)) with V_{zz} oriented along the magnetic field vector $\vec{B}$.

$\vec{B}$ is oriented perpendicular to the sample surface, following the *c*-axis of the Sm cell with the angles θ and ϕ being zero (Fig. 4.3). The isomer shift between the hexagonal and cubic sites is zero.
The evolution of the magnetic field $B(T)$ and the electric field gradient EFG(mm/s) with the temperature of the cubic and hexagonal sites derived from the fits, are summarized in Fig. 4.5. At $T = 4\,\mathrm{K}$, the cubic and hexagonal sites are magnetically ordered having maximum values of the magnetic field $B_h = 341(3)\,\mathrm{T}$ and $B_c = 316(4)\,\mathrm{T}$ (Fig. 4.5 a)). These values are in a good agreement with the value measured by Mössbauer spectroscopy $B = 345(18)\,\mathrm{T}$ at $4.2\,\mathrm{K}$ [114] and the expected value for the magnetic field of a free Sm^{3+} ion $B = 338(6)\,\mathrm{T}$ [115]. Calculations that take the strong exchange interactions for Sm atoms with hexagonal symmetry into account, found a value of $EFG = -7.8\,\mathrm{mm/s}$ [108]. The values for the *EFG* and the magnetic field at $T = 4\,\mathrm{K}$ can be compared with the results from [108][2]. These values are in a good agreement with the present results.
The temperature dependent paramagnetic *bcc* fraction extracted from the fits to the NFS data is shown in Fig. 4.6. With increasing temperature a paramagnetic fraction of Sm atoms with cubic symmetry appears (Fig. 4.6). This fraction increases until the cubic site is fully paramagnetic at $T = 15\,\mathrm{K}$. At temperatures higher than $T = 15\,\mathrm{K}$, only the hexagonal site is magnetically ordered. With increasing temperature, the value of the magnetic field of the hexagonal site is decreasing. At a temperature of $T = 105\,\mathrm{K}$, the Neél temperature of the hexagonal site, the magnetic ordering is completely vanished. Only traces of the temperature dependent *EFG* are visible in the spectrum of Fig. 4.5 b) at $T = 120\,\mathrm{K}$.

The hyperfine interaction parameters derived from the fits of the NFS data from the single crystalline film are compared with those from a polycrystalline Sm foil measured in the temperature interval $3 - 200\,\mathrm{K}$ [3] [111] in Fig. 4.5 and Fig. 4.6. The temperature dependence of the hyperfine interactions of the single crystalline film from the present study and the polycrystalline foil show good agreement (included in Fig. 4.5). A paramagnetic *bcc* fraction is found in the foil even at temperature

[2]The *EFG* in [108] is defined as $\Delta E_Q = eV_{zz}Q_g$. For direct comparison of the results the values of the *EFG* given in [108] have to be multiplied by a factor $Q_{ex}/2Q_g$.
[3]analyzed by A.Barla assuming a random distribution of *EFG* and magnetic field [111].

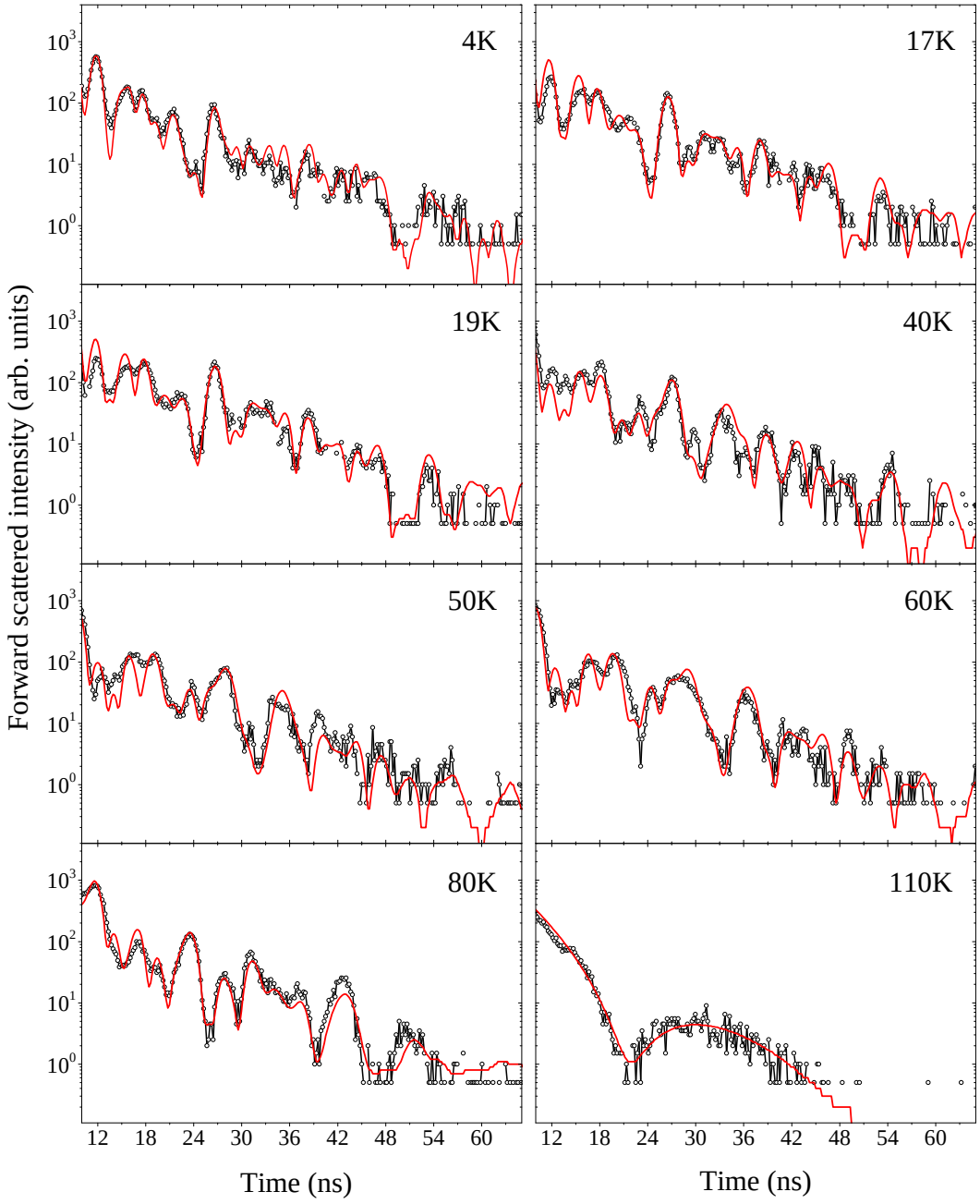

Figure 4.4.: Selected NFS spectra (open circles) measured *ex situ* on the Sm film covered with a Nb layer. The spectra are measured in a temperature range from $T = 4$ to 120 K. Fits (red solid line) to the spectra were performed using the program package REFTIM 4.3 [57, 58]. The parameters derived from the fits are summarized in Fig. 4.5 and Fig. 4.6.

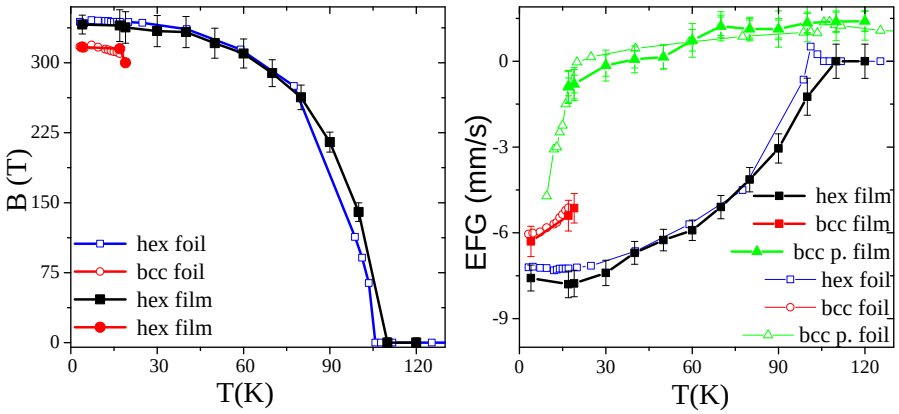

Figure 4.5.: Results from the analysis of the NFS data from Fig. 4.4 (full symbols), compared with the values from a polycrystalline foil (empty symbols). The magnetic field B(T) (left) and the electric field gradient EFG(mm/s) (right) are shown as a function of the temperature. The Neél temperatures are $T_c = 15\,\mathrm{K}$ for the Sm atoms with cubic symmetry and $T_h = 105\,\mathrm{K}$ for the Sm atoms with hexagonal symmetry. The paramagnetic *bcc* fraction exhibits an EFG labeled as *bcc p* shown as full green triangles/empty green triangles for film and foil, respectively.

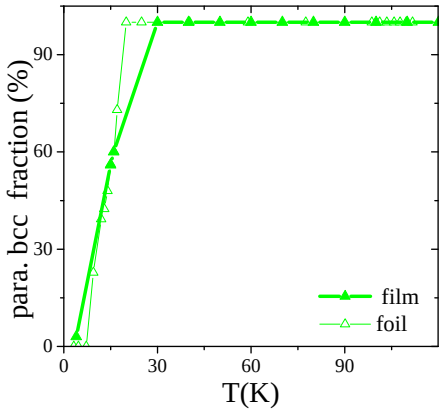

Figure 4.6.: Paramagnetic *bcc* fraction as a function of the temperature obtained from the NFS data (Fig. 4.4) of the Sm film (full symbols) and compared with the values of a polycrystalline Sm foil (empty symbols). For temperatures lower than the Neél temperature of the *bcc* site, a fraction of paramagnetic *bcc* is found. The fraction decreases with decreasing temperature and is zero at 4 K.

lower than the Neél temperature of the *bcc* site. These values are depicted in Fig. 4.6 and agree well with the values obtained in this study. The analysis of the obtained NFS spectra unambiguously proves the formation of *Sm type* Sm and excludes a possible formation of other Sm phases and oxides.

Prior to the NIS experiment for the determination of the lattice dynamics, *in situ* NFS spectra were measured at 297 K and 94 K as a proof for structure and sample quality. The same hyperfine interaction parameters as in Fig. 4.5 are used for the fit of these spectra. A comparison of the fit and the experimental data is shown

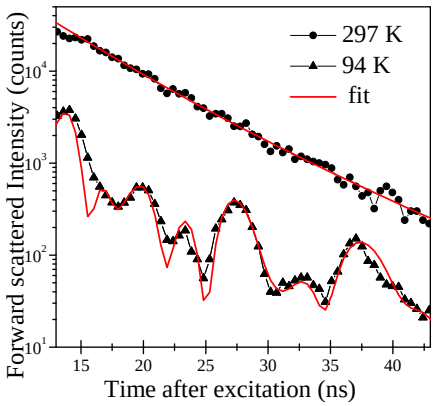

Figure 4.7.: NFS spectra at 94 K and 279 K measured on the Sm film before the *in situ* NIS experiment. The spectra are fitted (red line) with the same set of parameters as used for the *ex situ* NFS data (Fig. 4.4) [111].

in Fig. 4.7. From the good agreement between both, a degradation of the sample between the *in situ* NIS and *ex situ* NFS and XRD experiment is excluded.

4.1.2. Lattice dynamics

The raw data of the NIS measurements performed at 111 K and at 270 K at an incidence angle of α_{in}=6.981 mrad along the [$\bar{1}$100] direction of the (0001) Sm film is shown in Fig. 4.8. The critical angle for Sm at the photon energy of E=22.5015 keV is $\alpha_c = 2.25$ mrad. The experimental value of $\alpha_{in} = 6.981$ mrad was chosen in order to increase the bulk and to decrease the surface contribution to the measured signal. The phonon DOS was calculated from the experimentally obtained NIS spectra shown in Fig. 4.8.
To get a comprehensive understanding of the lattice dynamics of Sm, *ab initio* calculations [4] have been performed by a collaboration partner. The phonon DOS

[4]The *ab initio* calculations were performed by the Group of P.Piekarz from the Institute of Nuclear Physics, Polish Academy of Sciences, Krakow using the density functional theory implemented in the VASP program [41]. There, the full-potential projector-augmented wave method [42] with the generalized-gradient approximation (GGA) was used for the calculation of the lattice parameters and magnetic moments for the $R\bar{3}m$ structure of Sm with three atoms in the primitive cell. The valence basis was assumed to have 16 electrons per atom in the $5s^2 5p^6 4f^6 6s^2$ configuration in a collinear ferromagnetic order. In order to investigate the influence of the spin-order coupling on the lattice dynamics, the calculations were done with and without spin-orbit-coupling (SOC) [111]. In comparison to the experimental values for the lattice constants (c=26.21(8)$\mathring{A}$ and a=3.62(8) [82]), the optimized values are larger by 2%. This is attributed to the GGA method that is known to overestimate the lattice parameters. In addition, the assumed ferromagnetic order differs from the antiferromagnetic order and may as well have an influence on the parameters and magnetic moments. Using the DFT optimized parameter, the phonon energies were calculated by the PHONON program [45, 46]. A super cell of 36 atoms was assumed. For the lattice parameters the experimental values were used. Nonequivalent atoms were displaced and the Hellmann-Feynman forces acting on all atoms in the super cell are calculated [43, 44]. By the diagonalization of the dynamical matrix the phonon dispersion relations were calculated.

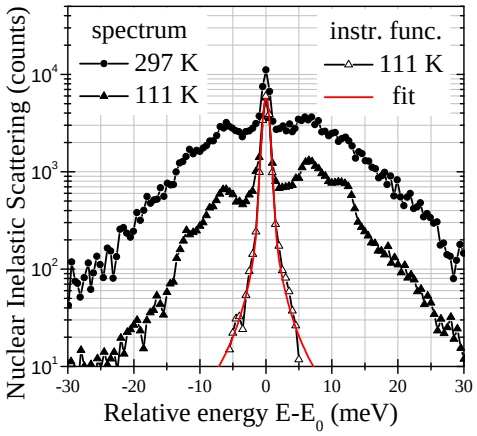

Figure 4.8.: Energy dependence of the nuclear inelastic absorption measured at 111 K and 279 K. The latter is shifted up by a factor of 10 for clarity. Open triangles show the instrumental function measured at $T = 111$ K. The solid red line is the to the instrumental function fitted pseudo-Voigt function with a FWHM= 1.115(4) meV. Due to the low Lamb-Mössbauer factor the spectrum at 279 K is dominated by multi-phonon excitations. To reduce this effect, the sample was measured at 111 K [111].

and dispersion relations of the *Sm type* structure obtained from the calculations are plotted in Fig. 4.9 a) and b) respectively.

Fig. 4.10 a) shows the $[\bar{1}100]$ projected experimental phonon DOS of the single crystalline film extracted by the program DOS from the NIS data at 111 K and 297 K (Fig.4.8). The large error bars for the data measured at 297 K originate from the lower statistical accuracy and the high contribution of multi-phonon excitations due to the low Lamb-Mössbauer factor at this temperature [116]. The phonon DOS is characterized by phonon peaks at 7.5, 8.5 and 12 meV with an onset of a phonon peak at 11.5 meV. The high energy cut off is at 16 meV. The *ab initio* calculated, $[\bar{1}100]$ projected and with the Gauß function with a full width at half maximum (FWHM) of 1.1 meV convoluted phonon DOS is plotted with red line in Fig. 4.10 a). The value for the convolution was derived from the FWHM of the instrumental function. The discrepancy in the high energy cutoff most likely origins from the residual strain induced by the Nishiyama-Wasserman epitaxial relation between the (110)Nb buffer and the (0001) Sm film. Fig. 4.10 b) shows the phonon DOS of the polycrystalline foil determined at $T = 297$ K. The spectrum reveals the onset of the phonon peak at 11.5 meV and confirms the broadening of the 12 meV peak observed in the phonon DOS of the film. In the same image the direction-averaged and with the Gauß function convoluted *ab inito* calculated phonon DOS is displayed by a red line. The direct comparison shows that the low energy parts of the calculated and experimental phonon DOS coincide. The onset of the peak at 11.5 meV is not found in the calculations. An explanation could be the splitting of the phonon modes at 12 meV due to electron correlation effects based on electron-phonon interactions that were not included in the calculations.

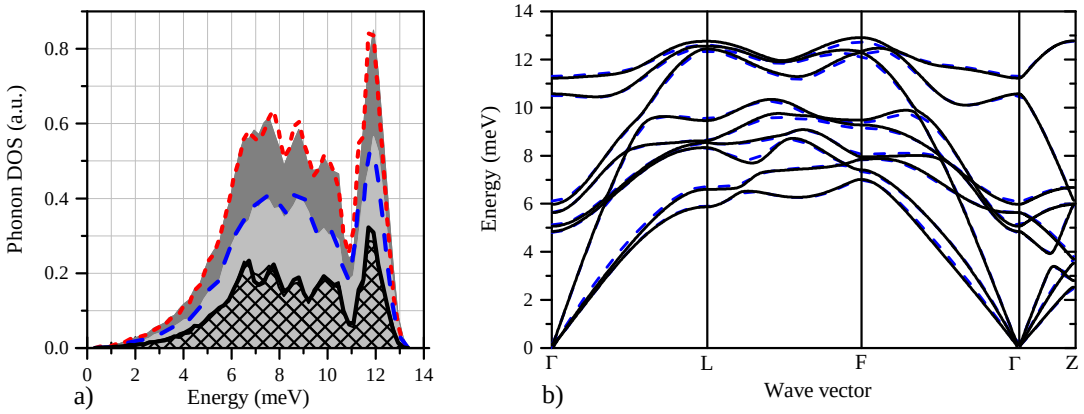

Figure 4.9.: *Ab inito* calculations for *Sm type* Sm [111]. a) Phonon DOS: with (lines) and without (filled areas) spin orbit coupling for the total (red broken line, dark gray area), the x,y-projected $[\bar{1}100]$ (blue broken line, light gray area) and the z-projected along [0001] (black line, area filled with lines) phonon DOS. b) Dispersion relations calculated with (black lines) and without (blue dashed lines) spin-orbit coupling: The high symmetry points are in units of $2\pi/a$: $\Gamma = (000)$, $L = (\frac{1}{2}00)$, $F = (\frac{1}{2}\frac{1}{2}0)$, $Z = (\frac{1}{2}\frac{1}{2}\frac{1}{2})$.

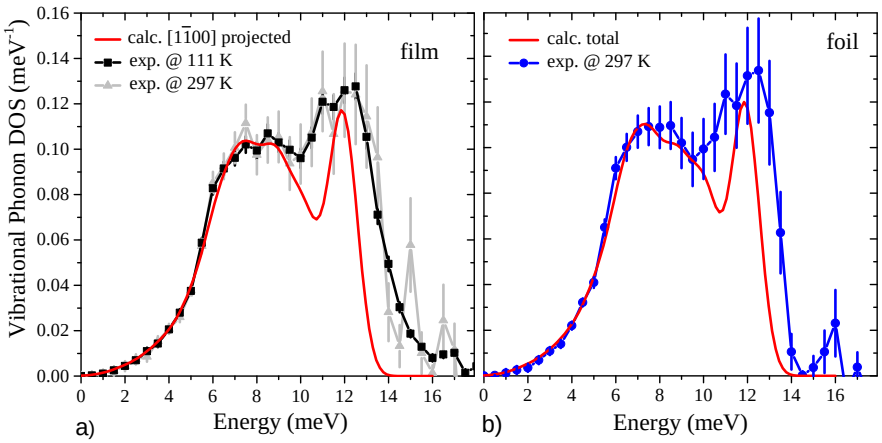

Figure 4.10.: a) Experimental phonon DOS obtained at 111K (black) and 297K (gray). The red line shows the $[\bar{1}100]$ projected theoretical phonon DOS. b) phonon DOS of a polycrystalline foil measured at 297K. The red line depicts the calculated phonon DOS averaged over all crystallographic directions [111]).

Thermodynamic and elastic properties

Once the phonon DOS of Sm is known, the thermodynamic and elastic properties can be calculated (section 2.1.2).
The thermoelastic properties were calculated using the phonon DOS of the epitaxial Sm film and the polycrystalline Sm foil at 111 K (Fig. 4.10). The values of the mean force constant (Eqn.(2.27)), sound velocity Eqn.(2.26), lattice specific heat Eqn.(2.22) and vibrational entropy Eqn.(2.76) are compared with the values de-

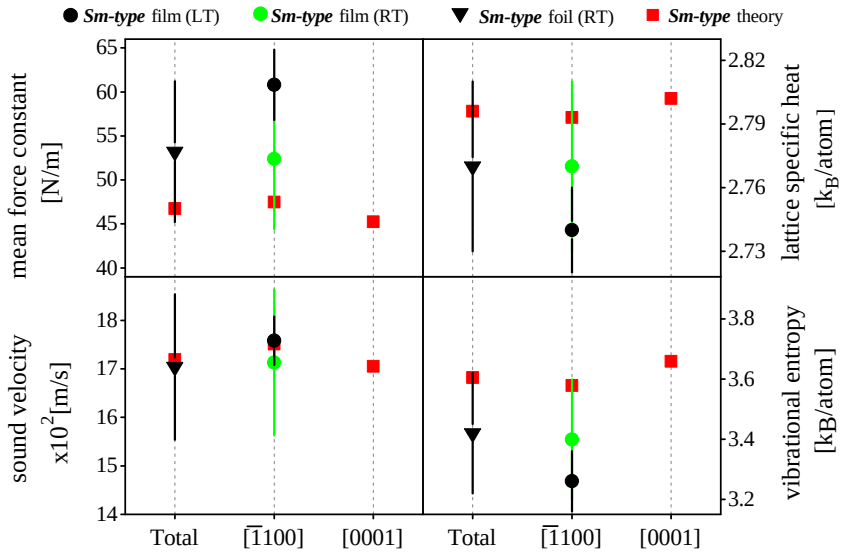

Figure 4.11.: Elastic (mean force constant, sound velocity) and thermodynamic (vibrational entropy, lattice specific heat) properties at 111 K obtained from the total and direction projected ([$\bar{1}$100], [0001]) experimental and *ab inito* calculated phonon DOS. The values derived from the phonon DOS of the polycrystalline foil at 297 K (RT) and the single crystalline (0001) Sm film at 297 K (RT) and 111 K (LT) are shown.

rived from the *ab inito* calculated phonon DOS in Fig. 4.11. The theoretical values calculated from the total phonon DOS (direction averaged) and from the phonon DOS projected along the nonequivalent directions [$\bar{1}$100] and [0001] (Fig. 4.9), are shown in Fig. 4.11.

The sound velocity is calculated from the low energy part of the phonon DOS by Eqn.(2.26). The experimental and calculated phonon DOS coincide for the epitaxial film as well as for the polycrystalline foil in the low energy parts resulting in an excellent agreement between the values of the sound velocity. The source of the deviations for the mean force constant, lattice specific heat and vibrational entropy from the theoretical values is the broadening of the peak at 12 meV and therefore the higher energy cutoff in comparison to the theoretical DOS.

A deviation between the thermoelastic properties calculated at 297 K from the phonon DOS measured at 111 K and the thermoelastic properties from the phonon DOS measured at 297 K exists. This can be attributed to anharmonic effects in the lattice dynamics of the *Sm type* Sm.
The physical properties such as the electrical-resistivity [117], magnetic susceptibility [118] and the heat capacity [119, 120, 121] of Sm have already been studied. All studies show anomalies at 14 K and 106 K. Both anomalies can be attributed to the onset of antiferromagnetism of the atoms located at the cubic and hexagonal sites, respectively. Anomalies at the magnetic ordering temperatures are not reported for the temperature dependence of the Debye temperature determined from earlier

experiments via the measured longitudinal sound wave velocities [122]. Thus, the Debye temperature was estimated to be $\Theta_D = 165\,\mathrm{K}$ at a temperature of 274 K [122]. Colorimetric measurements, for the estimation of the magnetic contribution to the heat capacity done by Jennings *et al.*, estimated the Debye temperature to be $\Theta_D = 150\,\mathrm{K}$ at 274 K [121].
The Debye temperature can also be calculated from the Debye model approximation for the calculation of the Lamb-Mössbauer factor. In the present study, the phonon DOS of the polycrystalline Sm foil is used to calculate the value $f_{LM} = 0.17(1)$ at $T = 274\,\mathrm{K}$. In the high-temperature limit of the Debye model from Eqn.(2.37):

$$\ln(f_{LM}) = -\frac{6E_R T}{k_B \Theta_D^2}, \tag{4.2}$$

we obtain a Debye temperature $\Theta_D = 146(2)\,\mathrm{K}$ at $T = 297\,\mathrm{K}$. Here $E_R = 1.8231\,\mathrm{meV}$ is the recoil energy for ^{149}Sm and k_B the Boltzmann constant. This temperature is in good agreement to the value from Jennings *et al.* [121]. A disagreement of about $\Delta\Theta_D$=15 K from the study of Rosen *et al.* [122] to the values from the present study is found. The difference questions the results from Rosen *et al.*, where the data was derived from longitudinal and transverse sound velocities measured by the ultrasonic pulse technique [122].

4.1.3. Conclusions

A 500 nm thick single crystalline (0001)*Sm type* structured Sm film was grown on (110)Nb/(11$\bar{2}$0)Al_2O_3 and characterized by *ex situ* XRD. Additionally, the structure is confirmed by the temperature evolution of the hyperfine interactions, determined from the analysis of the temperature dependent NFS data measured in the range $4 - 120\,\mathrm{K}$. The analysis shows that the quantization axis of the magnetic field is oriented along the *c*-axis of the *Sm type* structure. The assumption of a symmetric *EFG* with the z-component oriented parallel to the quantization-axis of the magnetic field is proven to be correct by the close correspondence between the fitted values and the values derived at 3 K published elsewhere [108]. Excellent agreement between the temperature dependent hyperfine interaction parameters is found for the polycrystalline foil [111] and the epitaxial film. Both confirm the presence of a paramagnetic fraction of the *bcc* site at temperatures lower than the Neél temperature of this phase (14 K).
The lattice dynamics of the epitaxial film and the polycrystalline foil, both exhibiting the *Sm type* structure, is derived by determining the phonon DOS. A comparison with the first principles calculation reveals a good agreement at low energies. The onset of a peak at 11.5 meV in the phonon DOS that is not found in the calculations as well as the broadening of this peak suggest strong electron-phonon interactions that were not included in the calculations.
Thermodynamic and elastic properties of this metal are obtained using the phonon DOS. The sound velocities calculated from the low energy part of the phonon DOS of the experimental and calculated phonon DOS show an excellent agreement. The deviation of the mean force constant, lattice specific heat and vibrational entropy

from the phonon DOS measured at 111 K with the properties calculated for 297 K and the properties directly derived from the spectrum measured at 297 K indicate the existence of anharmonic effects in the lattice dynamics of *Sm type* Sm. The Debye temperature determined from the high temperature approximation of the Lamb-Mössbauer factor is in agreement with the published values [121].

4.2. *dhcp* Samarium

Introduction

Sm undergoes a series of crystallographic phase transitions at high pressure, transforming from native *Sm type* structure to *dhcp*, *fcc*, disordered *fcc* and *hcp* phases[123].

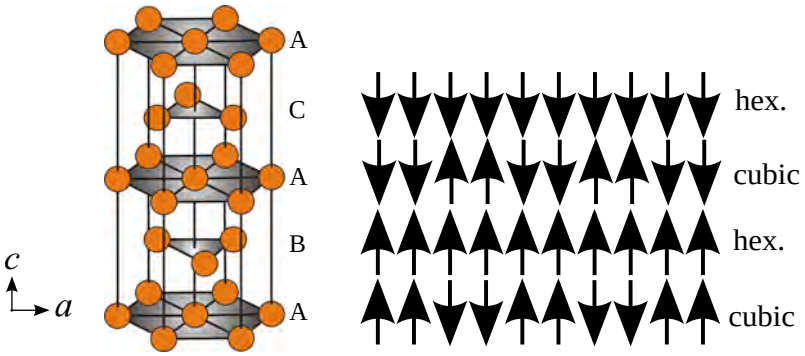

Figure 4.12.: Left: crystal unit cell of *dhcp* Sm with the *ABACA* staking. Right: Magnetic structure of the *dhcp* Sm. The coupling between hexagonal planes separated by cubic planes is antiferromagnetic leading to a +0-0+0... sequence along c. Within the hexagonal planes, the coupling is ferromagnetic and antiferromagnetic within the planes of cubic symmetry [83].

In the *dhcp* phase, Sm exhibits an $A_cB_hA_cC_h$ stacking (Fig. 4.12 Left) with the indices corresponding to a cubic (c) and a hexagonal (h) local symmetry. Both sites have a Neél temperature of 25 K, revealed by earlier neutron-scattering and resonant X-ray magnetic scattering experiments [83]. In comparison to the hexagonal sites of the *Sm type* structure, the ordering temperature is significantly reduced from 106 K to 25 K. This can be attributed to the isolation of every hexagonal site by cubic sites. On the other hand, the separation of the cubic planes by only one hexagonal plane leads to an increase of the ordering temperature of the cubic sites from 15 K in the *Sm type* structure, to 25 K in *dhcp* Sm [83]. The magnetic structure proposed by Dufour et al. is shown on the right side of Fig. 4.12. Similarly to the *Sm type* structure, the coupling between the hexagonal planes separated by cubic planes is antiferromagnetic leading to a +0-0+0... sequence along c. Within the hexagonal planes, the coupling is ferromagnetic [83].
Shi *et.al.* were able to stabilize this phase from polycrystalline bulk Sm at normal pressure by heat treatment [124]. Recently, a MBE grown 500 nm thick *dhcp* Sm film was reported [83]. There, an additional Neodymium (Nd) layer on $(110)Nb/(11\bar{2}0)Al_2O_3$ was used as a template to stabilize the *dhcp* Sm phase [83].

4.2.1. Sample growth and characterization

The growth of the *dhcp* structure by the method described in [83] is not the only possible technique to obtain a high quality single crystalline *dhcp* Sm film. We

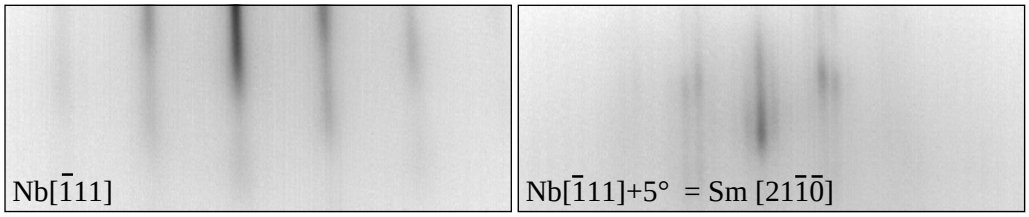

Figure 4.13.: RHEED images of the (110)Nb surface along the [$\bar{1}$11] azimuthal direction and the 5° clockwise rotated, the [2$\bar{1}\bar{1}$0] azimuth of Sm, indicating the NW orientation relationship. The satellite streaks are characteristic for a surface reconstruction on the (0001)Sm surface.

report the MBE growth of *dhcp* Sm directly on the (110)Nb surface, without a (0001)Nd layer. The 500 nm thick *dhcp* Sm film is grown in the RE-MBE system in the UHV-Analysis laboratory at ANKA/Karlsruhe.
The (110)Nb buffer layer was grown on the A-plane Al_2O_3 at a temperature of 1173 K. After the high temperature deposition of the buffer layer, the substrate was cooled down to the Sm growth temperature. Sm was evaporated from a PBN crucible with an evaporation rate of 10 $\AA$/min. The evaporation rate was continuously controlled by a quartz crystal monitor placed in the vicinity of the substrate. At a substrate temperature of 573 K, Sm grows in the *Sm type* structure, as described by Dofour *et al.* [82]. However, with an increase of the substrate temperature to 773 K, while keeping all other parameters constant, a 500 nm thick *dhcp* Sm film was obtained. The RHEED images in Fig. 4.13 show the [$\bar{1}$11] azimuth of (110)Nb surface and the 5° clockwise rotated [2$\bar{1}\bar{1}$0] azimuth after the deposition of Sm, indicating a NW-type epitaxial relation. Similarly to the *Sm type*, the *dhcp* Sm film grows with the *c*-axis parallel to the surface normal.
The RHEED image shows satellite streaks characteristic for a surface reconstruction, similarly to the results reported by Dufour *et al.* [82]. After the RHEED investigations, the Sm film was covered by a 20 nm thick Nb layer to avoid oxidation.

The crystalline structure of the film was studied in detail by *ex situ* XRD at the photon energy $E = 7.976$ keV. The reciprocal space map of the H0L plane is shown in the reciprocal lattice units of the *dhcp* structure ($4H$) in Fig. 4.14[5]. The map reveals that the sample contains two hexagonal based phases. A cut through the [H0L] plane along $H = 2$, shown in Fig. 4.15 (left) confirms the dominating contribution from the *dhcp* structure consisting of 4 layers ($4H$). However, a contribution of about 15% from the native *Sm type* phase with the stacking of 9 layers ($9R$) is also visible. From this study, the lattice constants of the *dhcp* structure were estimated to be $a = 3.64\,\AA$ and $c = 11.75\,\AA$. These values are consistent with the published values ($a = 3.629\,\AA$, $c = 11.673\,\AA$ [82]). The positions of the *dhcp* peaks (Fig. 4.15 (Right) $4H$) are displaced in comparison to the *Sm type* peaks (Fig. 4.15 (Right) $9R$) indicating that the lattice constant a of the *Sm type* Sm is by about 2% larger than the lattice constant of the *dhcp* Sm.

[5]Reconstruction of the map done by A. Bosak

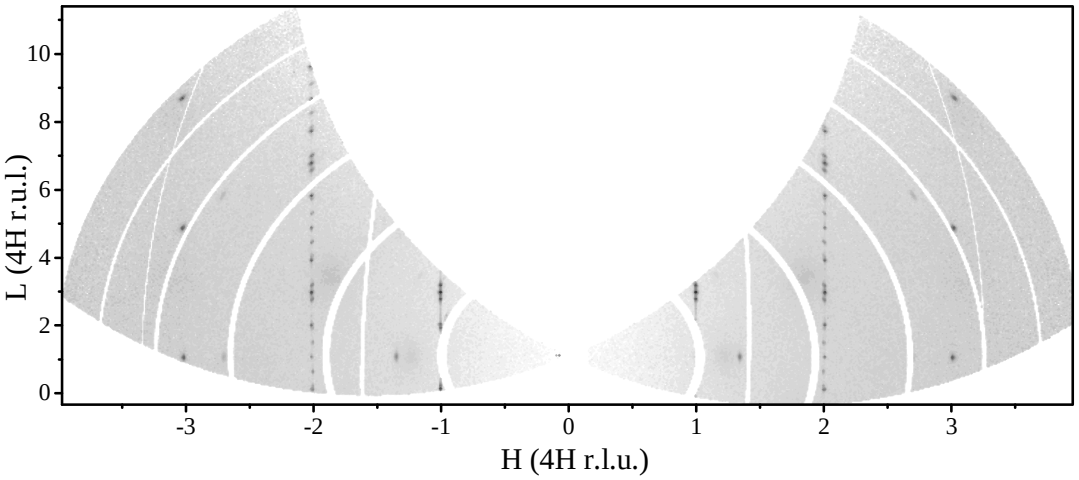

Figure 4.14.: Reciprocal space map of the H0L plane, reconstructed from several scans measured at the photon energy $E = 7.976\,\mathrm{keV}$.

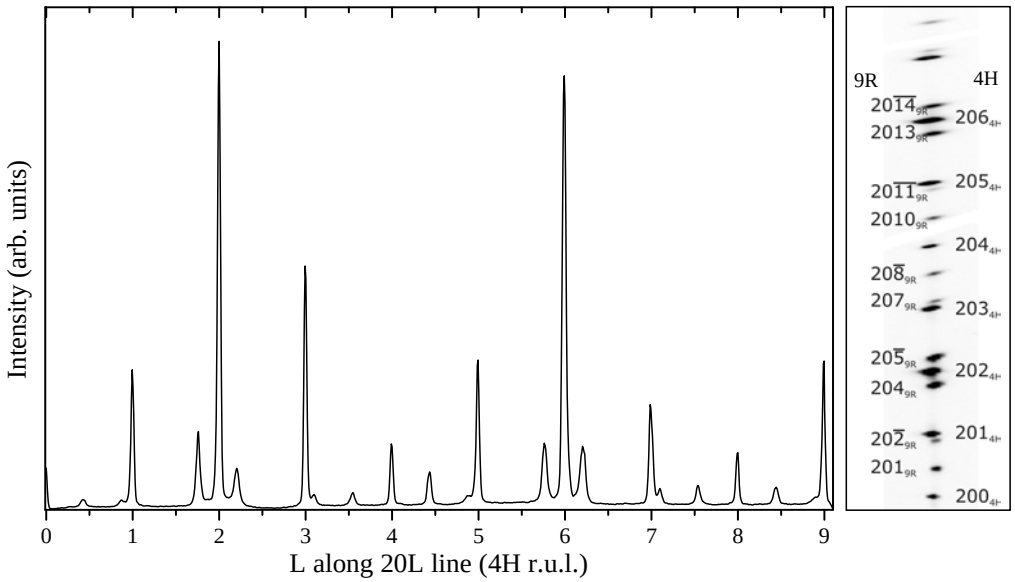

Figure 4.15.: Left: Cut through the reciprocal space [H0L] plane along [20L], in reciprocal unit length of the *dhcp* Sm structure ($4H$r.u.l.). Right: 2D cut from the [H0L] plane in the vicinity of [20L]. The peaks from the *dhcp* structure are indicated with $4H$ and the Sm type structure peaks are marked with $9R$.

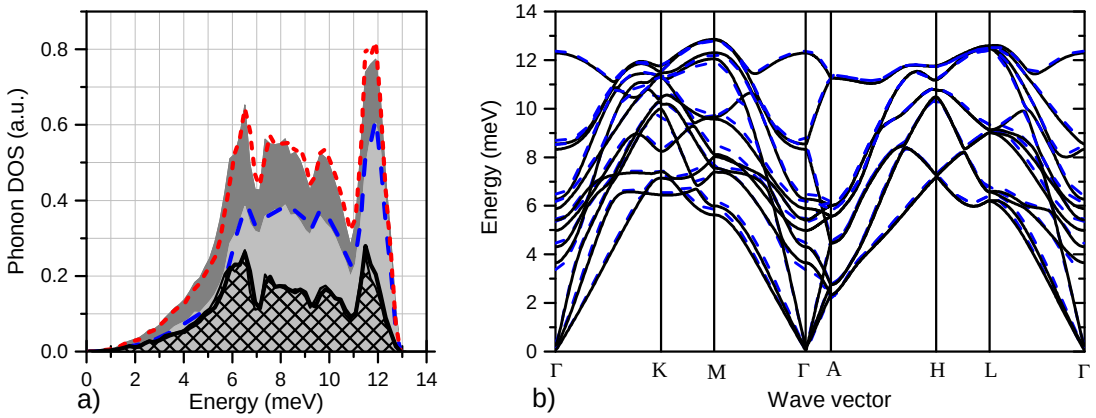

Figure 4.16.: a) *Ab inito* calculated phonon DOS for *dhcp* Sm [111]. The calculations were done with spin-orbit coupling for the total (dark gray area), $[\bar{1}100]$ (xy) projected (light gray area), [0001] z-projected (grid area) phonon DOS, and without spin-orbit coupling for the total (red dotted line), $[\bar{1}100]$ xy-projected (dashed blue line) and [0001] z-projected (solid black line) phonon DOS. b) Corresponding *ab inito* calculated dispersion relations for *dhcp* Sm [111]. The high symmetry points are in units of $2\pi/a$: $\Gamma = (000)$, $K = (\frac{1}{3}\frac{1}{3}0)$, $M = (\frac{1}{2}00)$, $A = (00\frac{1}{2})$, $H = (\frac{1}{3}\frac{1}{3}\frac{1}{2})$, $L = (\frac{1}{2}00)$. The calculations were done with (black lines) and without (blue dashed lines) spin-orbit coupling.

4.2.2. Lattice dynamics

The lattice dynamics of *dhcp* Sm was investigated by IXS and first principles calculations. The experimental values of the lattice constants obtained from the XRD study were used for the calculations[6]. The derived *ab initio* calculated phonon DOS and the corresponding dispersion relations are shown in Fig. 4.16 a) and b), respectively.

The calculations are done with and without spin-orbit coupling (SOC). Fig. 4.16 a) shows the phonon DOS for the total (grey), xy-projeced (light grey) and z-projected (grid area) with SOC. The phonon DOS without SOC is shown with lines (total (red dotted), xy-projeced (blue dashed), and z-projected (black)). Fig. 4.16 b)

[6]The *ab initio* calculations were performed by the Group of P.Piekarz from the Institute of Nuclear Physics, Polish Academy of Sciences, Krakow using the density functional theory implemented in the VASP program [41]. There, the full-potential projector-augmented wave method [42] with the generalized-gradient approximation (GGA) was used for the calculation, assuming 16 electrons per atom for the valence basis in the configuration $5s^2 5p^6 4f^6 6s^2$. An energy cut-off of 520 eV was set for the plane wave expansion. Similar to the calculations for *Sm type* Sm, a collinear ferromagnetic order was assumed and the spin-orbit coupling was taken into account. For the *dhcp* Sm with the space group $P6_3/mmc$, four atoms in the primitive unit cell were assumed for the calculation of the lattice parameters and magnetic moments. The phonon energies were calculated using the PHONON program [45, 46]. A super cell of 32 atoms was assumed. The calculations were performed adopting the experimental values of the lattice constant.

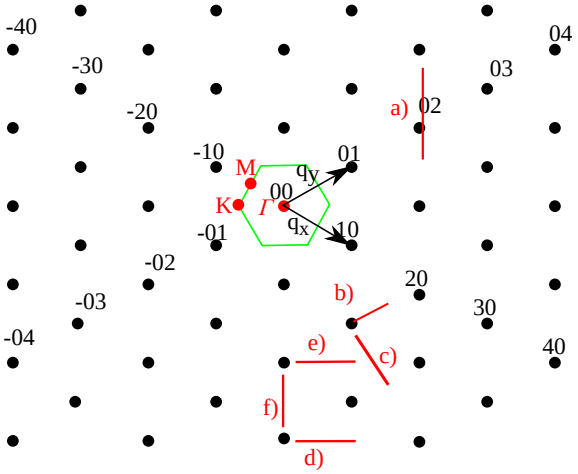

Figure 4.17.: Reciprocal space lattice of *dhcp* Sm in the q_x, q_y-plane with the high symmetry points Γ, K, M. The measured paths, projected on the q_x, q_y-plane are indicated by red lines a) – f). The green hexagon corresponds to the q_x, q_y projection of the first Brillouin zone and is a guide for the eye.

shows the dispersion relations between the high symmetry points (Γ, K, M, A, H, L) corresponding to the phonon DOS. This theoretical study demonstrates that the influence of the SOC on the lattice dynamics of the *dhcp* Sm can be neglected.

Measurements of the phonon dispersion relations by IXS

The IXS experiment was performed at the beamline ID28 at the ESRF/Grenoble at an energy of 17.793 keV and an energy resolution of 2.2 meV (FWHM). The setup of the beamline is described in section 2.4.1 and the theoretical background to IXS is discussed in section 2.4.
Due to the rather small sample thickness $d = 500\,\text{nm}$ the sample was measured in grazing incidence geometry. The experiment was performed at room temperature to avoid a possible influence of the complex magnetic ordering. The direction and value of the momentum transfers Q were selected by choosing the scattering angle and the sample orientation in the horizontal scattering plane.

Fig. 4.17 shows the reciprocal space with the paths measured in the IXS experiment. High symmetry points (Γ, K, M) and the reciprocal lattice vectors (q_x, q_y) are indicated. Due to the grazing incidence experimental geometry all measurements are performed with an offset of $q_z \sim 0.5\,\text{nm}^{-1}$.
The comparison of the experimental data with the calculated phonon branches along the measured paths (4.17 a)-f)) are shown in Fig. 4.18 a-f). The measured points along the dispersion relations are plotted with black squares, while the calculated dispersion relations are shown with colored lines. The colors correspond to the intensity and the scale bar shown in Fig. 4.18 d) applies for all plots. Low intensity branches are added as gray lines for completeness. The directions of the measurements are given in reciprocal lattice units hkl. Slight deviations are attributed to the

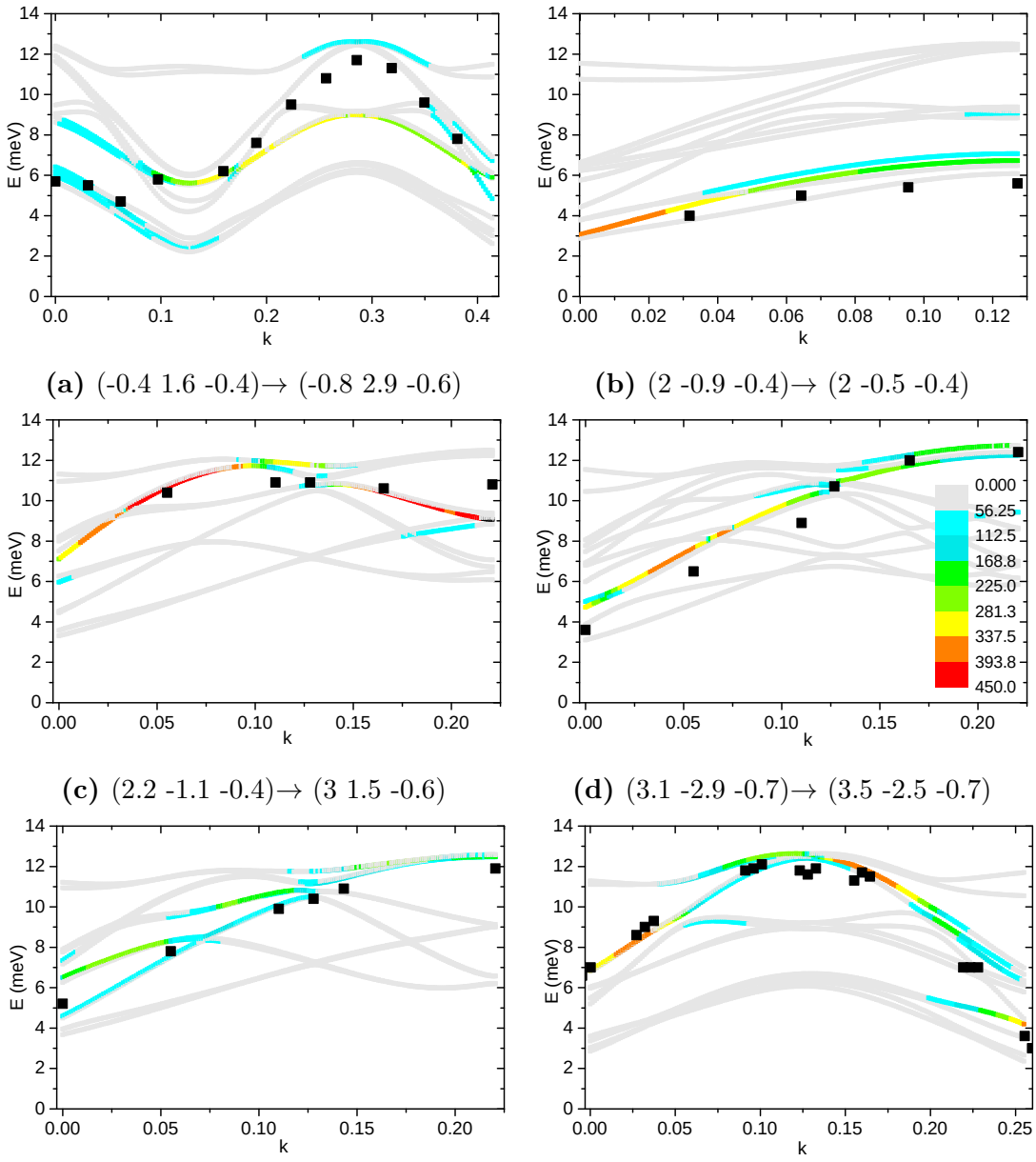

(a) (-0.4 1.6 -0.4)→ (-0.8 2.9 -0.6)

(b) (2 -0.9 -0.4)→ (2 -0.5 -0.4)

(c) (2.2 -1.1 -0.4)→ (3 1.5 -0.6)

(d) (3.1 -2.9 -0.7)→ (3.5 -2.5 -0.7)

(e) (2 -1.9 -0.5)→ (2.5 -1.5 -0.5)

(f) (2.1 -2.1 -0.5)→ (2.9 -2.9 -0.7)

Figure 4.18.: Comparison of the calculated dispersion relations (colored lines) and the measured points (black points) in units of $k = 2/a\sqrt{3}$. The paths in the reciprocal space are given in reciprocal primitive vectors. The scale in d) (intensity in counts) is valid for all spectra. The branches plotted with gray lines have very small intensities and are added for the sake of completeness.

limited energy resolution of about 2 meV of the inelastic spectrometer. A deviation of the experimental points from the calculated branches are found in Fig. 4.18 a). There the experimental points are on the blue shaded branch instead on the yellow shaded branch, which should have a higher intensity. All other plots show a good agreement between the experimental points and the calculated phonon branches.

Comparison of the thermodynamic and elastic properties of *Sm type* and *dhcp* Sm

The values of the total, [$\bar{1}$100] (xy), and [0001](z) projected mean force constant, sound velocity, lattice specific heat, and vibrational entropy of *Sm type* and *dhcp* structure are compared in Fig. 4.19. The values are derived from the measured and *ab initio* calculated phonon DOS for both structures at 111 K. The values for *dhcp* Sm are obtained from the first principles calculated phonon DOS after verification of the phonon dispersion relations by the IXS experiment. In comparison to *Sm type* Sm, *dhcp* Sm exhibits a reduced lattice specific heat and vibrational entropy and an increased mean force constant and sound velocity, Fig. 4.19 (Total).
The in-plane (xy-projection) values coincide for both structures. The differences in the values from the total phonon DOS originate from the differences of thermodynamic values in the out-of-plane direction (z-projection). This is a direct consequence from the different types of plane stacking along the c-direction of both structures.

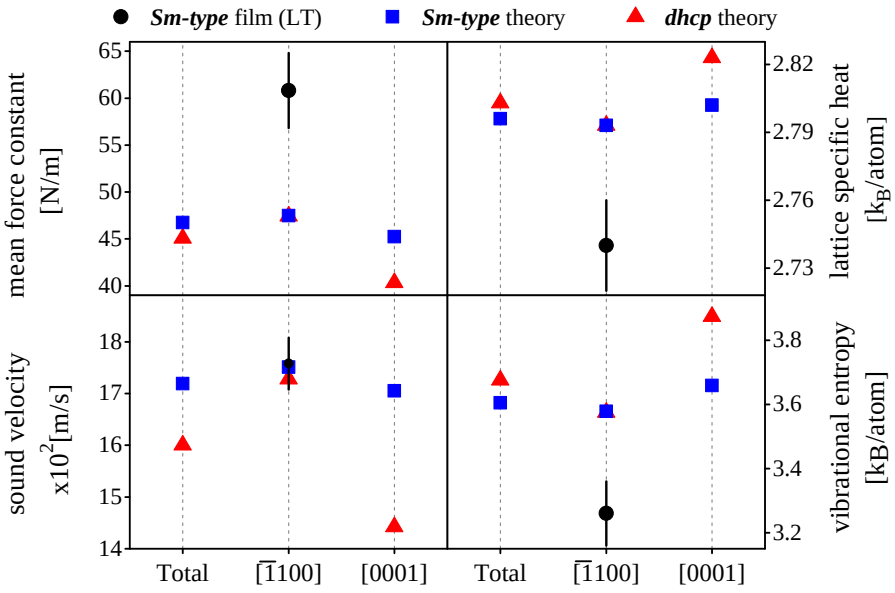

Figure 4.19.: A comparison of the total, [$\bar{1}$100] (xy), and [0001] (z) projected elastic (mean force constants, sound velocity) and thermodynamic (vibrational entropy, lattice specific heat) properties for *Sm type* and *dhcp* Sm derived from the *ab initio* calculated DOS at 111 K. Additionally, the experimental values for the *Sm type* film measured at 111 K are shown.

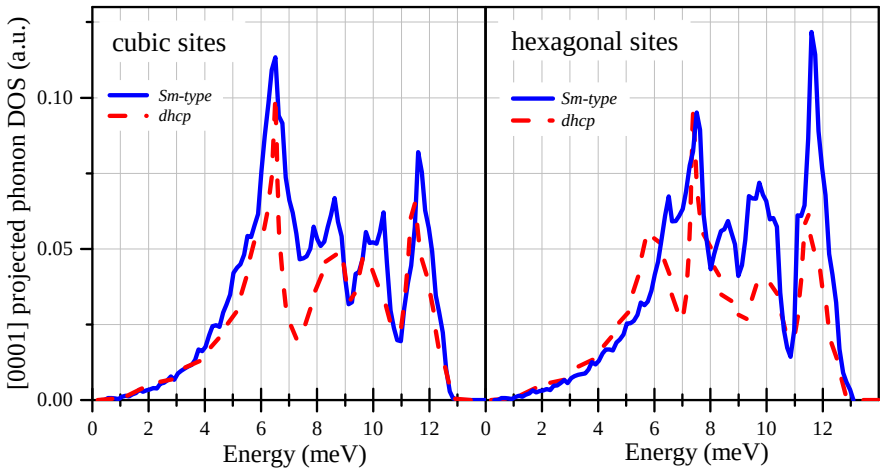

Figure 4.20.: Comparison of the *ab initio* calculated [0001] projected partial DOS of Sm atoms with cubic (left) and hexagonal (right) symmetry in the *Sm type* (solid blue line) and the *dhcp* (dashed red line) unit cells ([111]).

Fig. 4.20 shows a comparison of the [0001] projected phonon DOS of the *Sm type* and *dhcp* Sm.
Sm atoms with cubic symmetry vibrate in a similar manner in both unit cells (Fig. 4.20 left). Fig. 4.20 right reveals that the vibrational anisotropy in the *dhcp* structure arises from differences in the phonon DOS of the hexagonal sites. The [0001] projected values exceed the [$\bar{1}$100] projected values by 8.4% for the vibrational entropy and by 1.1% for the lattice specific heat. The mean force constant and the sound velocity are reduced by 14.1% and 16.1%, respectively. In comparison, the thermoelastic quantities of the *Sm type* structure are almost isotropic.
Difference in the [0001] projected values arise from the layer stacking sequences in *Sm type* (*chhchhchh*...) and *dhcp* (*chch*...) structures. This modifies the site-specific (*h* (hexagonal), *c* (cubic)) vibrational thermodynamic and elastic properties predominantly of the *dhcp* Sm [111].

4.2.3. Conclusions

We demonstrate the growth of a *dhcp* Sm film, directly on the (110)Nb surface. The *dhcp* phase can be stabilized at a substrate temperature of T_S=773 K. The 500 nm thick *dhcp* Sm film was grown and characterized by RHEED and XRD. A contribution of 15% of *Sm type* Sm was found from the [20L] cut in the reciprocal space. The derived lattice constant of *dhcp* Sm was used for the *ab initio* calculation of the lattice dynamics. The phonon dispersion relations are measured by IXS at grazing incidence geometry. The results are in good agreement with the calculated branches.
This allows the determination of the thermodynamic and elastic properties of *dhcp* Sm. The comparison of these values with those of the *Sm type* structure reveals a higher anisotropy along [$\bar{1}$100] (xy), and [0001](z) of the mean force constants,

vibrational entropy and lattice specific heat for *dhcp* Sm with ($c/a = 3.2$) while the values for *Sm type* Sm ($c/a = 7.2$) are rather isotropic. First principles calculations revealed the origin of the anisotropy of the thermodynamic properties to be the vibrational anisotropy in the [0001] projection of the hexagonal sites of the *dhcp* structure, while the Sm atoms with cubic symmetry vibrate in a similar way in both unit cells.

4.3. Neodymium

Introduction

Neodymium belongs to the light lanthanides and exhibits the [Xe]$4f^4 6s^2$ electron configuration. At ambient conditions it crystallizes in the *dhcp* structure with the lattice constants $a = 3.658\,\mathring{A}$ and $c = 11.8\,\mathring{A}$ [125]. Similarly to *dhcp* Sm, the sites of nearly cubic symmetry (A) alternate with sites of nearly hexagonal symmetry (B,C) in a $ABACA\ldots$staking sequence. At a temperature of $T_N = 19.9\,\mathrm{K}$, the hexagonal sites order in an antiferromagnetic, incommensurate sinusoidal order [126]. In the temperature range of $9\,K < T < 19.1\,\mathrm{K}$, the magnetic structure of the hexagonal sites can be well described by a flat spiral structure, which induces a similar spiral order on the cubic sites [127]. This behavior is considered as one of the most complex magnetic structures known through out the periodic table.
Although the thermoelastic properties of Neodymium like the specific heat, thermal expansion and the elastic constants have been investigated in the past [122, 128, 129], the lattice dynamics of this metal is investigated only partly until today.

4.3.1. Sample growth and characterization

The standard method for the growth of thick single crystalline Neodymium crystals is the Birgdman method [130]. There, the sample is recrystallizing after a heat treatment from a polycrystalline bulk material in a crucible. The sample then consists of large, single crystalline grains. These grains can be cut to single crystalline pieces. However, it is also possible to grow thin single crystalline (0001)Nd films by MBE. These layers, for example, are used as template layers for the growth of *dhcp* Sm [18]. We have adopted this approach to produce (0001)Nd films with a sufficiently high thickness for IXS experiments. Following the procedure described in section 3.1.2, the (110)Nb buffer layer was grown on an A-plane Al_2O_3 substrate at a temperature of $T_S = 1173\,\mathrm{K}$. The quality of the (110)Nb surface was proven by RHEED. The images were of similar quality to Fig. 3.6. The electron diffraction patterns exhibit streaks revealing a smooth surface of high quality. After the buffer layer growth, the substrate temperature is reduced to the growth temperature of Nd

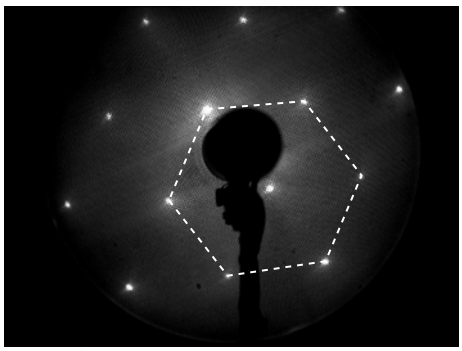

Figure 4.21.: LEED image of the (0001) surface of the 1 μm thick Nd sample. The hexagon indicates the hexagonal symmetry of the reciprocal lattice of Nd.

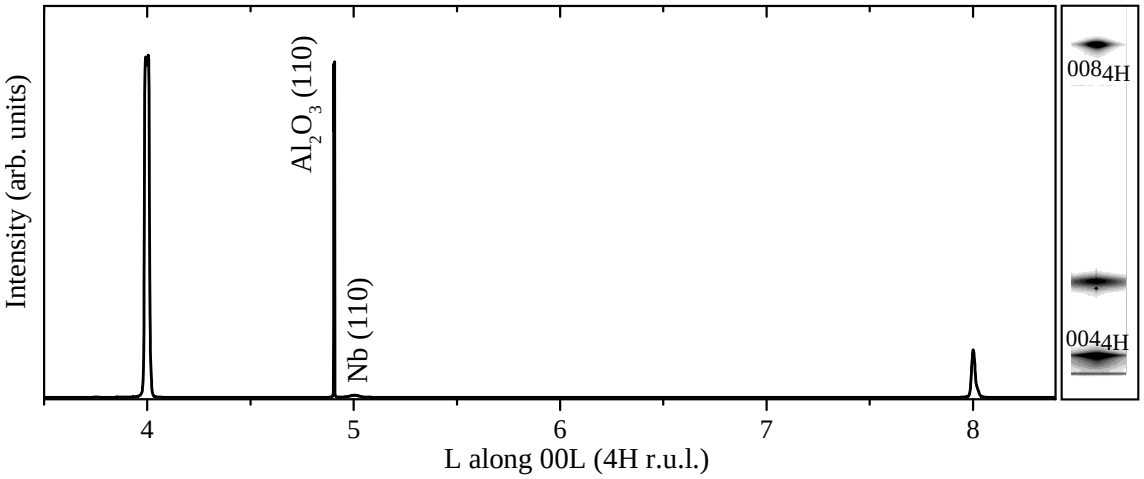

Figure 4.22.: XRD scan on the 1μm thick (0001)Nd film. Left: Cut of the reciprocal space along [00L], in reciprocal unit length units. Right: 2D cut from the plane in reciprocal space around [00L].

$T_S = 773\,\mathrm{K}$. Vacuum outgassed Nd supplied by the Ames Laboratory, was evaporated from a crucible with a rate of $10\,\mathring{A}$/min. The evaporation rate is constantly controlled by a water cooled quartz crystal monitor in the vicinity of the substrate. Under this growth conditions a single crystalline (0001)Nd film, with a thickness $d = 1\,\mu$m was obtained. The low energy electron diffraction (LEED) image of the (0001)Nd surface is shown in Fig. 4.21. The sharp diffraction spots indicate the formation of a smooth, single crystalline surface. The hexagonal symmetry reveal the crystallographic orientations to be (0001)Nd ‖ (110)Nb following the NW orientation relationship. After the investigation by LEED, the sample was covered by a 15 nm thick Nb layer to prevent the reactive Nd film from oxidation.
Ex situ XRD was performed using a Rigaku SmartLab X-ray diffractometer. Fig. 4.22 shows a scan along [00L] and a cut from the reciprocal space in the vicinity of [00L]. The indexed peaks belong to the *dhcp* ($4H$) structure. The not indexed peaks are from the A-plane Al_2O_3 substrate and the (110)Nb buffer layer. The measurements reveal a good crystalline quality of the film and confirm the *dhcp* stacking with the lattice constants of $a = 3.659(5)\,\mathring{A}$, $c = 11.796(5)\,\mathring{A}$. This values are in good agreement to the values $a = 3.6579\,\mathring{A}$ $c = 11.7992\,\mathring{A}$ published by Spedding *et.al* [125].

4.3.2. Lattice dynamics

Similarly to the study of *dhcp* Sm reported in section 4.2 the lattice dynamics of Nd was determined by IXS experiment and *ab inito* calculations adopting the experimental lattice constant [7].

[7] The *ab initio* calculations were performed by the Group of P.Piekarz from the Institute of Nuclear Physics, Polish Academy of Sciences, Krakow using the density functional theory implemented in the VASP program [41]. The full-potential projector-augmented wave method [42] with the generalized-gradient approximation (GGA) was used for the calculation, assuming 14 electrons

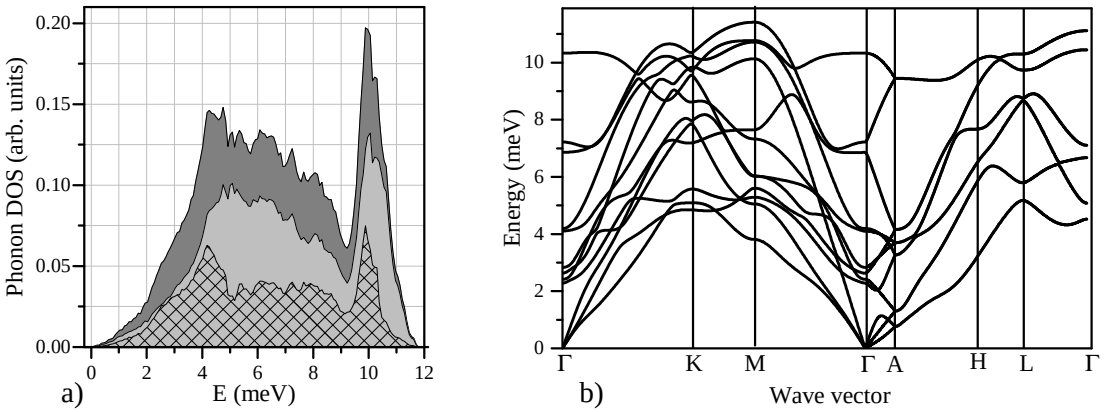

Figure 4.23.: Left: Total (gray area), xy-projected [$\bar{1}$100](light gray area) and z-projected [0001] (grided area) phonon DOS of Nd. Right: Dispersion relation between the high symmetry points Γ, K, M, A, H, L.

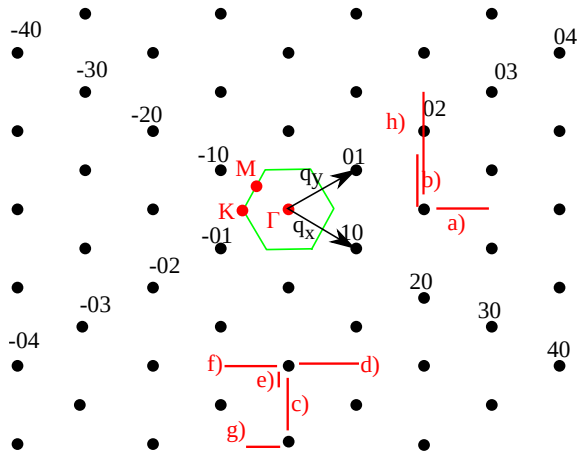

Figure 4.24.: The q_x,q_y-projection in the reciprocal space of the *dhcp* Nd lattice. The measured points are aligned along the red lines with an offset in q_z. The main symmetry points Γ, M, K are shown. The green hexagon represents the q_x,q_y-projection of first Brillouin zone is a guide for the eye.

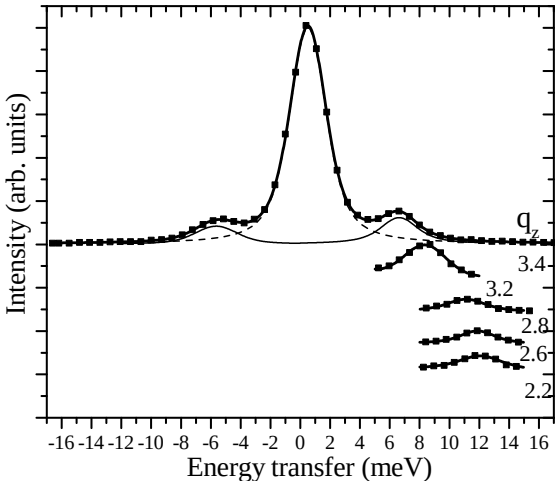

Figure 4.25.: IXS spectra for selected q_z values (in reciprocal lattice vector units). The experimental data (black squares) is shown with the best fit (bold line). The fit of the elastic peak around 0 energy transfer is shown with a black dashed line, the fits of the Stokes and anti-Stokes peaks are shown by thin black lines. The spectra are shifted down for clarity conserving the scale.

Fig. 4.23 a) shows the results of the calculations: total (dark grey), xy-projected [$\bar{1}$100] (light gray) and z-projected [0001] (grid area) phonon DOS. Fig. 4.16 b) shows the calculated dispersion relations between the high symmetry points (Γ, K, M, A, H, L).
Using the calculated dispersion relations as a guideline, the IXS study was performed on the described sample at the beamline ID 28 of the ESRF/Grenoble (section 2.4). Due to the rather thin sample thickness $d = 1\,\mu$m, the experiment was performed in grazing incidence geometry. Therefore, the paths measured in the q_x, q_y-plane of the reciprocal space were not measured along the high symmetry directions but exhibit an offset of $q_z \approx 0.2\,\mathrm{nm}^{-1}$. The experimental paths are shown projected on the q_x, q_y-plane of the reciprocal space in Fig. 4.24. In the q_z direction it was possible to measure along the high symmetry direction $\Gamma - A$. Energy scans at several wave vector transfers, along this direction are displayed in Fig. 4.25. The experimental points are visible as black squares. The spectra were fitted with Lorentzian functions and are shown as black line. The spectra are characterized by a strong elastic peak centered around zero and the Stokes and anti-Stokes peaks that correspond to phonon excitations and annihilation, respectively. For a better visibility only the Stokes part of the spectra is shown for wave vector transfer $q < 3.4$. A branch is visible along the q_z scan direction.

per atom for the valence basis in the configuration $5s^2 5p^6 4f^4 6s^2$. Similar to the calculations for *dhcp* Sm, a collinear ferromagnetic order was assumed. The spin-orbit coupling was not taken into account. For Nd with its *dhcp* structure the space group $P6_3/mmc$, four atoms in the primitive unit cell were assumed for the calculations of the lattice parameters and magnetic moments. The phonon energies were calculated using the PHONON program [45, 46]. A super cell of 32 atoms was assumed.

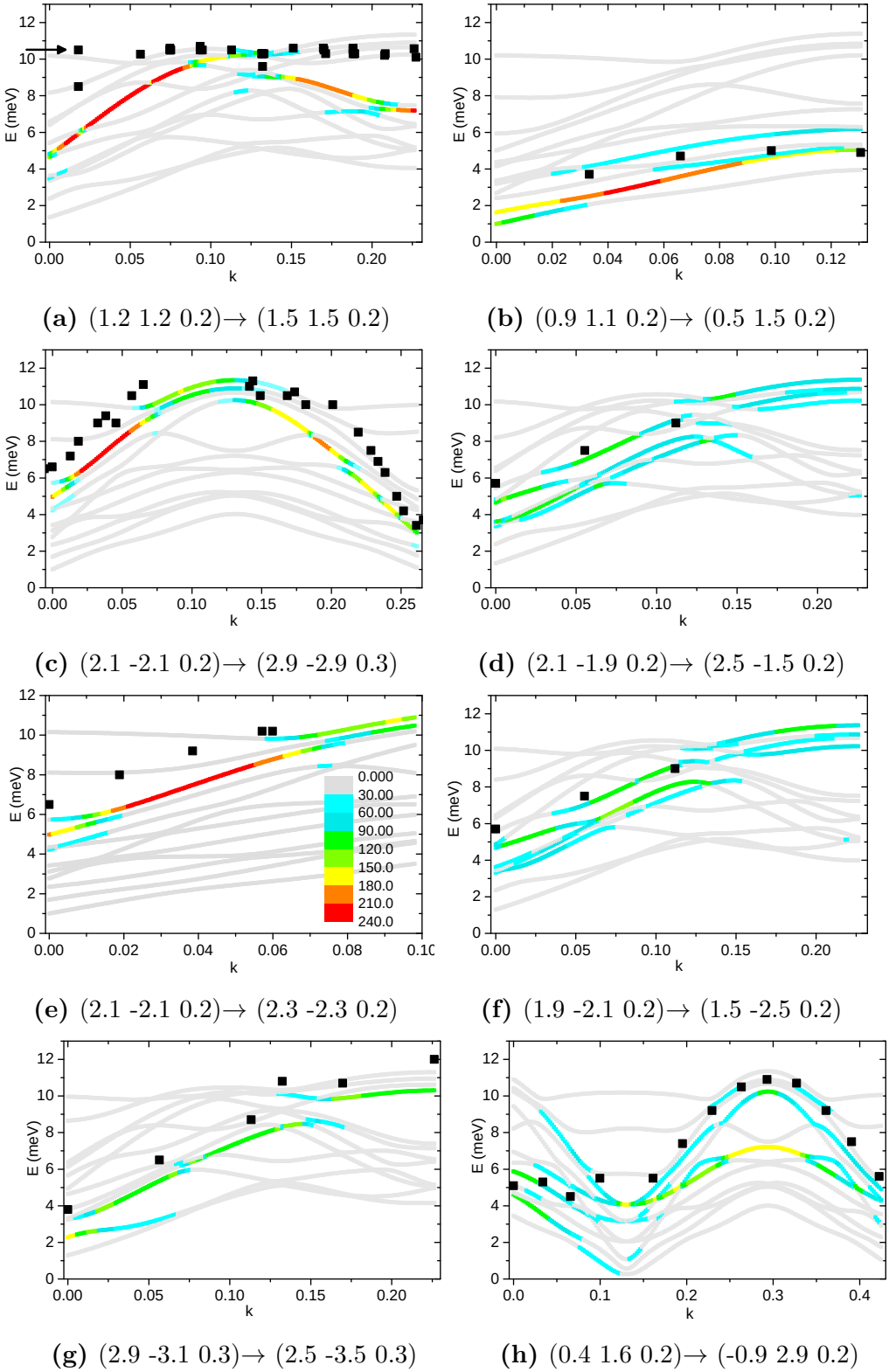

(a) (1.2 1.2 0.2)→ (1.5 1.5 0.2)

(b) (0.9 1.1 0.2)→ (0.5 1.5 0.2)

(c) (2.1 -2.1 0.2)→ (2.9 -2.9 0.3)

(d) (2.1 -1.9 0.2)→ (2.5 -1.5 0.2)

(e) (2.1 -2.1 0.2)→ (2.3 -2.3 0.2)

(f) (1.9 -2.1 0.2)→ (1.5 -2.5 0.2)

(g) (2.9 -3.1 0.3)→ (2.5 -3.5 0.3)

(h) (0.4 1.6 0.2)→ (-0.9 2.9 0.2)

Figure 4.26.: Comparison of the calculated dispersion relations and the measured points in the q_x,q_y-plane with an offset in q_z in units of $k = 2/a\sqrt{3}$. The positions in the reciprocal space (q_x, q_y, q_z) in reciprocal primitive vectors, are shown under the images. The scale in e) (intensity in counts) is valid for all spectra. Branches plotted as gray line have a very small intensity and are added for the sake of completeness.

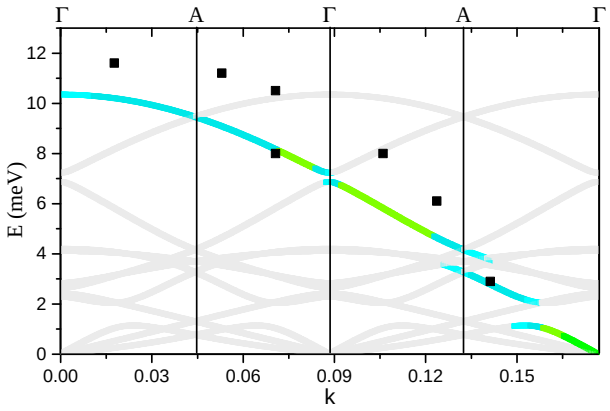

Figure 4.27.: Comparison of the experimental points (black squares) to the calculated phonon branches ($k = 1/c$) (colored branches) in q_z direction (0 0 2)→ (0 0 4). The scale in Fig. 4.26 e) (intensity in counts) is valid.

The experimental data is compared with the calculated phonon branches in Fig. 4.26 a)-h) (directions correspond to the paths in the q_x, q_y plane presented in Fig. 4.24 a)-h)) and additionally in Fig. 4.27 for the q_z direction. The intensity scale shown in Fig. 4.26 e) applies for all calculated dispersion relations. The experimental points of the dispersion relations (black squares) are plotted together with the calculated phonon branches. The branches of high intensity are shown as colored lines, while the low intensity branches are added as gray line for the sake of completeness. In Fig. 4.26 a) a disagreement between the experimental points and the dispersion relation of high intensity is found. Additionally, a splitting of the optical branch in two branches at E=11 meV is visible. The experimental points in the other images Fig. 4.26 b)-h) follow the trend of the high intensity branches, showing a systematic shift to higher energies in comparison to the calculated energies. The experimental points along the q_z (Fig. 4.27) show the most pronounced shift to higher energies. Small deviations of the measured points to the branches of high intensity can be attributed to the limited energy resolution of about 2 meV of the inelastic spectrometer but this alone cannot explain the observed disagreement between theory and experiment. A similar onset of a splitting was observed in the phonon DOS of *Sm type* Sm (Fig. 4.10). This effect is attributed to electronic correlations that are not included in the calculation. The shift of the experimental points to higher energies suggest that the effect of electron-phonon interactions is more pronounced for Nd in comparison to *Sm type* Sm and *dhcp* Sm.

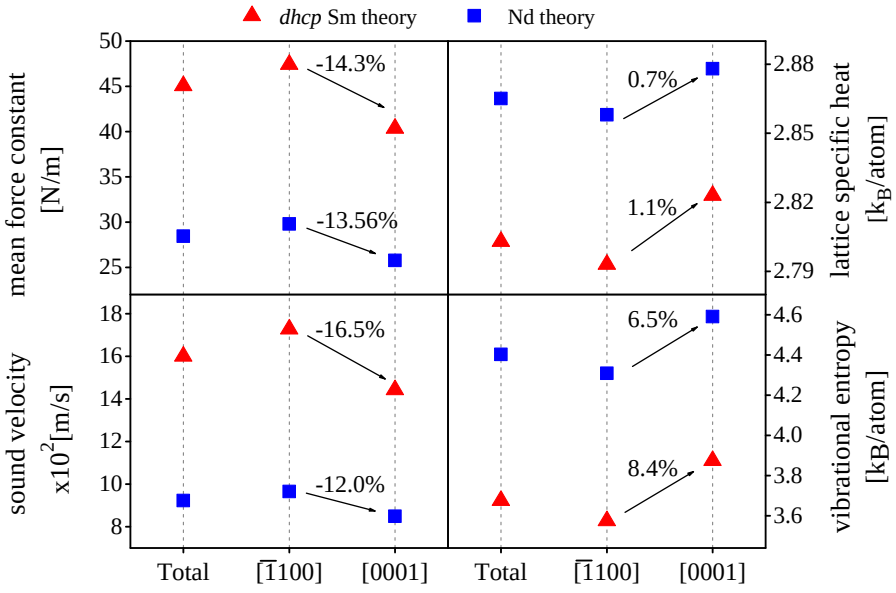

Figure 4.28.: Thermodynamic (lattice specific heat, vibrational entropy) and elastic (sound velocity, mean force constant) properties of *dhcp* Nd (blue squares) compared with the values of *dhcp* Sm (red triangles). All values are calculated from the total, xy-projected ([$\bar{1}$100]) and z-projected ([0001]) phonon DOS at 100 K.

Comparison of the thermoelastic properties of *dhcp* Sm and Nd

Having in mind that the *ab initio* calculations of the phonon dispersions of Nd have to be improved in the future a preliminary estimation of the thermodynamic and elastic properties of Nd, calculated at 100 K from the total and along the directions [$\bar{1}$100] and [0001] projected *ab inito* calculated phonon DOS are shown in Fig. 4.28. The values of *dhcp* Sm are also added to the same image for comparison.
The sound velocity in the z-direction ([0001]) for *dhcp* Sm is by 16.5% and for Nd by 12% smaller compared to the values from the xy-projection ([$\bar{1}$100]). The same behavior is observed for the force constant, the values being 14.3% for *dhcp* Sm and 13.6% for Nd, respectively. A decrease of the lattice specific heat by 1.1% for *dhcp* Sm and 0.7% for Nd exists. The entropy is reduced by 8.4% in *dhcp* Sm and 6.5% in Nd in [0001]. The differences of the values between the [0001] and [$\bar{1}$100] directions arise through the vibrational anisotropy along these directions. Comparing the differences in the values of the thermodynamic properties, the vibrational anisotropy in Nd is less pronounced than in *dhcp* Sm.

4.3.3. Conclusions

A high quality epitaxial (0001)Nd film with a thickness of 1 μm was grown on (110)Nb/Al_2O_3 and characterized by LEED and XRD. No traces from other possible Nd phases are found. The derived lattice constant of Nd is used for the calculation of the dispersion relations.
IXS measurements were performed with the calculated dispersions as a guideline. A comparison between the calculated phonon branches and the experimental points reveals a systematic shift to higher energies of the latter and a splitting of the optical branch. A similar observation of the splitting of the optical branch was found in the phonon DOS of *Sm type* Sm. Electron correlations are not included in the calculations and might be the origin of these effects and indicate the presence of strong electron-phonon interactions in rare earth elements [111]. The *ab inito* calculations of the phonon dispersions have to be optimized in the future. Therefore the thermodynamic and elastic properties of bulk Nd calculated from the present *ab inito* phonon DOS have to be seen as preliminary results on the way to obtain the real thermoelastic properties of this metal.

5. Europium: Lattice dynamics of nano-islands and wire-like nanostructures

The comprehensive understanding of changes in the lattice dynamics at the nanometer length scale requires the precise disentanglement of the influence of many factors such as size, shape, crystal structure, chemical state (oxidation), presence of grain boundaries, surfaces and interfaces. This, however, is a formidable experimental challenge that, as demonstrated below, can be successfully accomplished combining in situ nuclear inelastic scattering with ab initio calculations. This chapter describes the epitaxial growth and structure characterization of Eu nanostructures such as islands, films and wire-like nanostructures on the (110)Nb surface grown at various conditions. Their lattice dynamics is systematically investigated by in situ nuclear inelastic scattering and understood by the help of first-principles phonon calculations.

5.1. Introduction

In contrast to all other rare earth elements that exhibit hexagonal based lattices, Eu crystallizes in a *bcc* structure with a lattice constant $a = 4.5827\,\mathring{A}$ [131]. The reason for the formation of this structure is the electron configuration of the Eu atom $[\mathrm{Xe}]\,4f^7 6s^2$, meaning that the *4f* shell is half-filled. Eu exhibits a divalent character [132] with a $40-50\%$ larger atomic volume in comparison to other rare earth metals [133]. Another exception among the lanthanides is Ytterbium with a fully filled $4f$ orbital and an electron configuration $[\mathrm{Xe}]\,4f^{14}6s^2$, forming a *fcc* lattice. Due to the high atomic volume, both metals are highly compressible but their structures do not fit in the structure sequence exhibited by trivalent lanthanides as a function of external pressure (*hcp* → *Sm-type* → *dhcp*→ *fcc*→ *distorted fcc* [134, 135]). Instead, under high pressure Eu undergoes structural changes: *bcc* → *hcp* → *mixed phase*→ *orthorombic* [136]. At a pressure of 20 GPa, the molar volume of the Eu metal drops even below that of the fully trivalent metals Gd and Tb [134, 135, 137]. However, the assumption that this volume decrease indicates a transition to the trivalent state of Eu above 20 GPa turned out to be wrong. A transition from a divalent to a trivalent state would correspond to a magnetic to nonmagnetic transition ($Eu^{2+}[4f^7(J = 7/2)]$ → $Eu^{3+}[4f^6(J = 0)]$). Studies with modern synchrotron Mössbauer spectroscopy (SMS), X-ray absorption near edge structure (XANES) and X-ray magnetic circular dichroism (XMCD) at pressures up to 92 GPa show that the transition from the divalent to the trivalent state does not take place [138].
Superconductivity has been recently discovered in Eu at pressures above 75 GPa and

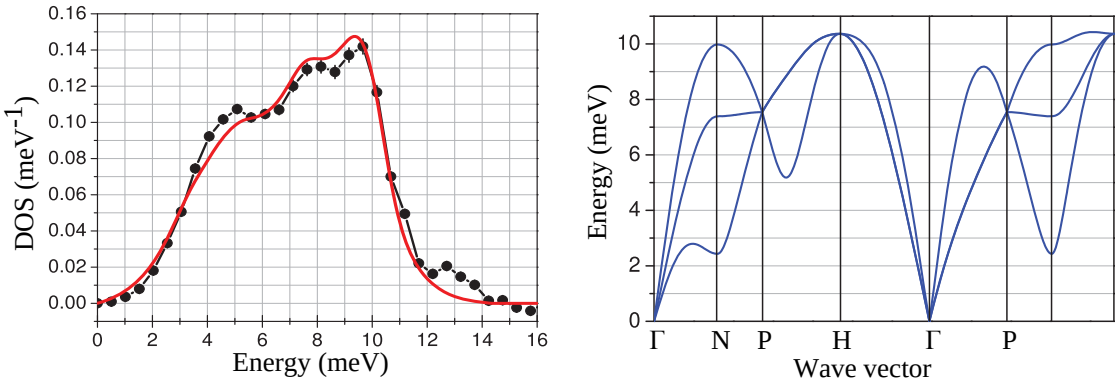

Figure 5.1.: Left: Comparison of the experimental and calculated phonon DOS of *bcc* Eu convoluted with the resolution function. Right: Phonon dispersion relations in the first Brillouin zone with the high symmetry points in units of $2\pi/a$; $\Gamma = (0,0,0)$, N=$(\frac{1}{2},\frac{1}{2},0)$, P=$(\frac{1}{2},\frac{1}{2},\frac{1}{2})$, H=(0,0,1) (images reproduced from Ref. [17]).

at temperatures below 3 K [139]. It has been suspected that the superconducting state of Eu is of the valency 3+ but it is rather in an intermediate valent or divalent state [138].
At ambient pressure Eu is an antiferromagent with the Néel temperature of T_N = 91 K [140]. The magnetic ordering process continues until a saturation appears at around $T = 20$ K.
The lattice dynamics of bulk Eu has been determined by *in situ* nuclear inelastic scattering and first principles calculations [17]. Instead of the complex magnetic structure, a simpler ferromagnetic ground state was assumed for the *ab initio* calculations, as suggested by Turek *et al.* [141]. A valence basis of 17 electrons per atom in the configuration $5s^2 5p^6 4f^7 6s^2$ with 16 atoms per $2 \times 2 \times 2$ supercell was assumed for the calculations. Due to the half filled $4f$ electron shell, the orbital moment was neglected. Fig. 5.1 (left) shows the phonon DOS of a 100 nm thick bulk like Eu film from the experiment (black line) and from *ab inito* calculations (red line). Fig. 5.1 (right) shows the calculated phonon dispersion relations along high symmetry directions of the reciprocal space. Despite the applied approximations the *ab initio* calculations reliable reproduced the experimental phonon DOS (Fig. 5.1).

Epitaxial growth of Eu on (110)Nb: Previous investigations

The growth of RE metals on TM surfaces is described in section 3.1.3. The epitaxial growth of Eu on Nb buffered Al_2O_3 in the native *bcc* structure as well as in a phase with hexagonal symmetry was demonstrated [18]. In the work of Soriano *et al.* Eu was grown at a comparably low substrate temperature $T_S = 423$ K on the oxygen reconstructed (110)Nb surface (grown at $T_S = 1173$ K) on $(11\bar{2}0)\,Al_2O_3$. At these conditions Eu forms a smooth film with a hexagonal symmetry and NW epitaxial relationship with the (110)Nb surface [18]:

$$[\bar{1}10]\text{Nb} \parallel [1\bar{1}00]\text{Eu} \quad \text{and} \quad [001]\text{Nb} \parallel [11\bar{2}0]\text{Eu}\,, \tag{5.1}$$

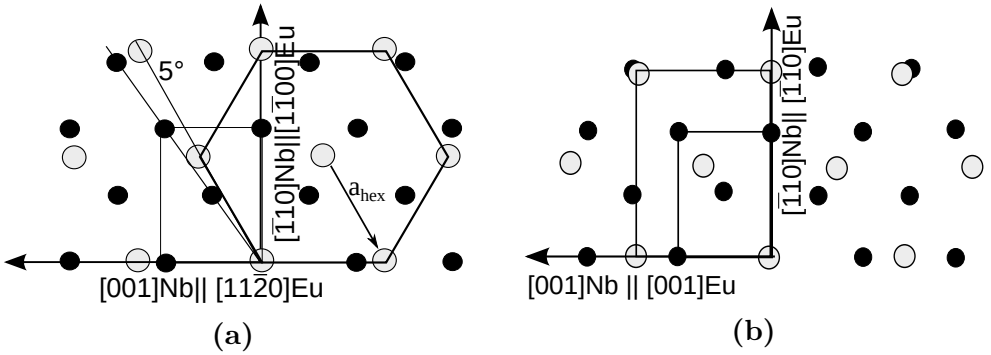

Figure 5.2.: Epitaxial relationships at first stages of Eu growth (gray dots) on a) an due to oxygen diffusion reconstructed (black dots) and b) an (110)Nb surface without oxygen reconstruction [18].

as sketched in Figure. 5.2 a). However, the first stage of the Eu layer growth with a thickness of up to 1.5 nm has not been investigated. The in-plane lattice constant of the structure with the hexagonal symmetry formed on the oxygen reconstructed (110)Nb surface was determined to be $a_{hex} = 4.27\mathring{A}$ (Fig. 5.2 b)) at a thickness of 3 nm [18]. With further deposition of Eu a relaxation to the *bcc* structure takes place. The formation of 6 domains, corresponding to the superposition of two Kurdjumov-Sachs (KS) orientations with respect to the initial hexagonal symmetry are possible with the epitaxial relationships [18]:

$$[\bar{1}2\bar{1}0]\text{Eu} \parallel [\bar{1}11]\text{Eu}, \quad [11\bar{2}0]\text{Eu} \parallel [\bar{1}11]\text{Eu} \quad \text{and} \quad [2\bar{1}\bar{1}0]\text{Eu} \parallel [\bar{1}11]\text{Eu}\,. \tag{5.2}$$

The structure of the intermediate phase that forms before the hexagonal Eu film has not been investigated up to now.

In the case of the deposition of Eu at $T_S = 423\,\text{K}$ on a (110) Nb buffer layer surface without surface reconstruction, *bcc* islands form that coalesce to a film at higher coverages, as reported by Soriano *et al.*. In this case the epitaxial relationship of Eu with respect to the (110) Nb surface is [18]:

$$[\bar{1}10]\text{Nb} \parallel [\bar{1}10]\text{Eu} \quad \text{and} \quad [001]\text{Nb} \parallel [001]\text{Eu}. \tag{5.3}$$

A sketch of the epitaxial relationship is shown in Fig. 5.2 b). In the study of Soriano *et al.*, the surface morphology of the (110)Nb layer grown at $T_S = 423\,\text{K}$ was, however, not investigated [18].
Gorioux et al. reported the growth of Eu islands with the *fcc* symmetry on an oxygen reconstructed O-$c(6 \times 2)$ (110)V (Vanadium) surface at substrate temperature $T_S > 533\,\text{K}$ [20]. The reason for the stabilization of the *fcc* structure, which is unusual for Eu, is proposed to be the formation of EuO at the interface between Eu and the O-$c(6 \times 2)$ reconstructed (110)V surface. Due to the divalent character of EuO and its similarity to metallic Eu, the performed XPS study could not unambiguously prove the formation of an EuO interface.

5.2. Growth of Eu ultra-thin films and nanostructures

Epitaxial growth of Eu on the (110)Nb surface strongly depends on the morphology, the substrate temperature during the growth and the deposition rate. In the following a systematic study of the influence of the buffer layer surface and its temperature on the growth of Eu nanostructures and films is presented.

5.2.1. Nb buffer layer: Growth of smooth and stepped surfaces

After the cleaning procedure applied to the $(11\bar{2}0)$-cut Al_2O_3 substrates, described in section 3.1.2, high purity (99, 9%) Nb (Goodfellow) was deposited with a rate of 1.5 $\AA$/min. The rate was continuously measured with a quartz oscillator placed in the vicinity of the substrate.

(110) Nb buffer layers grown at $T_S = 1173$ K: smooth surface

A 25 nm thick (110) Nb layer was grown on clean $(11\bar{2}0)Al_2O_3$ at a substrate temperature $T_S = 1173$ K. Fig. 5.3 a), b) shows the RHEED images obtained along the $[\bar{1}11]$ and $[\bar{1}10]$ azimuths, respectively. Both images reveal sharp main streaks and the presence of additional weak steaks between them. The additional low intensity streaks indicate the formation of an oxygen induced surface reconstruction. As outlined in section 3.1.2, Nb deposited at substrate temperatures $T_S > 573$ K on A-plane Al_2O_3, forms an oxygen induced reconstruction on the (110)Nb surface. The AFM image (Fig. 5.3 c)) shows the formation of flat terraces with an average length of 90 ± 20 nm and a width of 500 ± 100 nm.

An XPS study was performed on (110)Nb layers grown at different substrate temperatures. The spectra measured on the (110)Nb layer deposited at $T_S = 1173$ K (blue line) and $T_S = 423$ K (red line) are shown in Fig. 5.4. For a better comparability the spectra were normalized to the intensity of the $3p_{\frac{1}{2}}$ core level peaks being one and are shifted up by a constant factor. The plotted binding energy (E_B) range from 530 eV to 340 eV contains the O $1s$ core level peak at $E_B = 531.2$ eV and the Nb $3s$ and $3p$ core level peaks. The $3d$ Nb core level peaks are at the

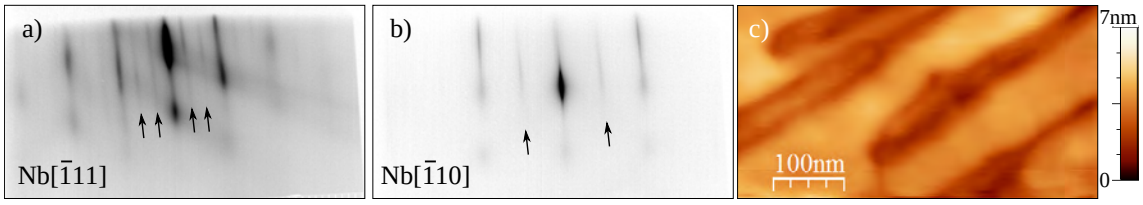

Figure 5.3.: a) and b) RHEED images along the indicated orientations of the (110) Nb buffer layer grown at $T_S = 1173$ K. The intermediate streaks, visible between the mains streaks (black vertical arrows), indicate the formation of an oxygen induced reconstruction. c) The AFM image shows the formation of smooth large terraces [142].

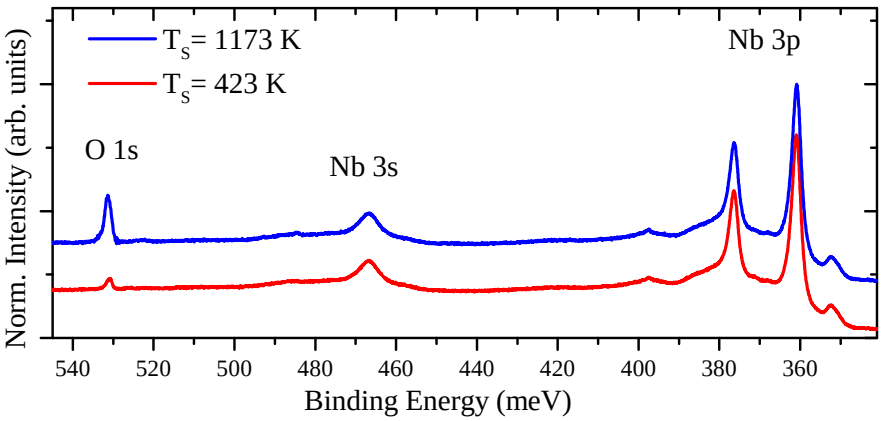

Figure 5.4.: XPS spectra measured from the (110)Nb layer grown on $(11\bar{2}0)Al_2O_3$ at $T_S = 1173\,K$ (blue) and $T_S = 423\,K$ (red).

positions $3d_{\frac{5}{2}}$ $E_B = 202.1\,eV$ and $3d_{\frac{3}{2}}$ $E_B = 205.0\,eV$, (not shown here) and are in agreement with the values published for metallic Nb ($3d_{\frac{5}{2}}$ $E_B = 202.2 \pm 0.2\,eV$ and $3d_{\frac{3}{2}}$ $E_B = 205.1 \pm 0.2\,eV$) [143]. The presence of Nb oxides on the surface would lead to a shift of the $3d$ core level peaks by about 2.5 eV to higher energies for NbO [144, 145], which was not observed.
The method for the estimation of the oxygen content on the surface was introduced in section 3.2.3. A relative oxygen content of $c_O = 19\% \pm 10\%$ compared to Nb was estimated, meaning a ratio of 1:5 of O to Nb atoms. This value is in a good agreement with the reported values of $c_O = 20\%$ for reconstructed Nb surfaces [87].

(110)Nb buffer layers grown at $T_S = 423\,K$: patterned surface

The oxygen diffusion during the Nd deposition is suppressed for substrate temperatures lower than $T_S < 723\,K$ [89]. Therefore, no oxygen induced surface reconstruction is formed in this case. Soriano *et al.* reported a Nb buffer layer grown at $T_S = 1173\,K$ that is overgrown by 15 nm Nb at a substrate temperature of $T_S = 423\,K$ to achieve an oxygen-free surface. Thus, the oxygen reconstructed (110)Nb surface is buried [18]. This approach was used in the present study for obtaining (110) Nb buffer layers without oxygen induced surface reconstruction.

A (110)Nb layer with a thickness $d = 15\,nm$ was grown at $T_S = 1173\,K$ on a clean $(11\bar{2}0)\,Al_2O_3$ substrate, afterwards it was overgrown by 15 nm Nb at a substrate temperature $T_S = 423\,K$. The RHEED and AFM study is presented in Fig. 5.5.
The RHEED images (Fig. 5.5 a), b)) were obtained along the azimuthal directions [001] and $[\bar{1}10]$, respectively. The streaks visible in both directions differ in length and width, indicating a difference of the surface morphology. The streaks are smooth and sharp along $[\bar{1}10]$Nb, indicating the formation of a smooth surface. However in [001] orientation intensity minima along the steaks are visible, suggesting a rougher structure. These results are confirmed by the AFM study revealing a stepped surface morphology with an alignment of the steps along $[\bar{1}10]$Nb and the average dimen-

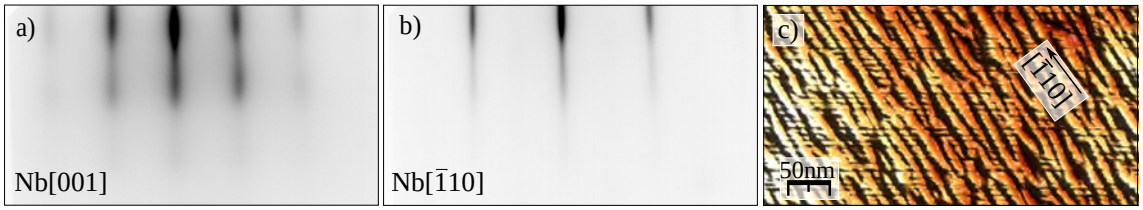

Figure 5.5.: RHEED images from the (110) Nb layer grown at $T_S = 423\,K$ in the azimuthal directions: a) [001] and b)[$\bar{1}$10]. The AFM image of the surface c) reveals the formation of long steps, aligned along [$\bar{1}$10] Nb, with the average dimensions: length $l = 293 \pm 144\,nm$, width $w = 10.1 \pm 2.4\,nm$ and height $h = 0.5 \pm 0.2\,nm$.

sions: length $l = 293 \pm 144\,nm$, width $w = 10.1 \pm 2.4\,nm$ and height $h = 0.5 \pm 0.2\,nm$ (Fig. 5.5 c)).
The XPS analysis of this (110)Nb layer reveals the presence of a small oxygen peak in the spectrum at E_B=530.4±0.2 eV (Fig. 5.4 (red line)). The oxygen content is determined to be $c_O = 4\% \pm 10\%$ in comparison to the Nb content. This amount of oxygen is not sufficient for the formation of an oxygen induced reconstruction, that is also supported by the RHEED study (Fig. 5.5).

5.2.2. Experimental aspects of the Eu growth

99.99 % pure Eu metal (Ames Laboratory) was evaporated from an effusion cell equipped with a boron nitride crucible, with a calibrated evaporation rate of $9.5\,\mathring{A}$/min. The rate was continuously controlled by a quartz oscillator placed in the vicinity of the substrate. The substrate temperature was kept stable during the Eu deposition. After the growth, the sample is cooled down to room temperature (RT) for characterization. The strong influence of the oxygen induced surface reconstruction and the surface morphology of the (110)Nb buffer layer on the epitaxial growth of Eu was investigated in details. In the following the Eu coverage is given in monolayer (ML) of *bcc* (110)Eu planes, which corresponds to a coverage of $1ML = 3.25\,\mathring{A}$.

5.2.3. *fcc* Eu islands

Eu with a nominal coverage of 2, 4, 5, 8 and 10 ML was deposited on the oxygen reconstructed (110)Nb surface at a substrate temperature of $T_S = 533\,K$. Fig. 5.6 summarizes the results from the RHEED and AFM study.
The RHEED images reveal a spotty pattern typical for electron diffraction from 3D islands. A tilting of the diffraction spots appears according to the faceting of the islands [97]. Two different diffraction patterns are observed that alternate every 30° of sample rotation with respect to the incident electron beam. Fig. 5.6 shows the RHEED images along the azimuthal directions [2$\bar{1}\bar{1}$0] and [1$\bar{1}$00]. The 3 fold symmetry together with the $\sqrt{3}$ ratio of the horizontal lattice spacing between the two alternating patterns reveal the hexagonal symmetry of the Eu islands. The [2$\bar{1}\bar{1}$0] azimuth is rotated by 5° towards the [$\bar{1}$11] direction of the (110) Nb film.

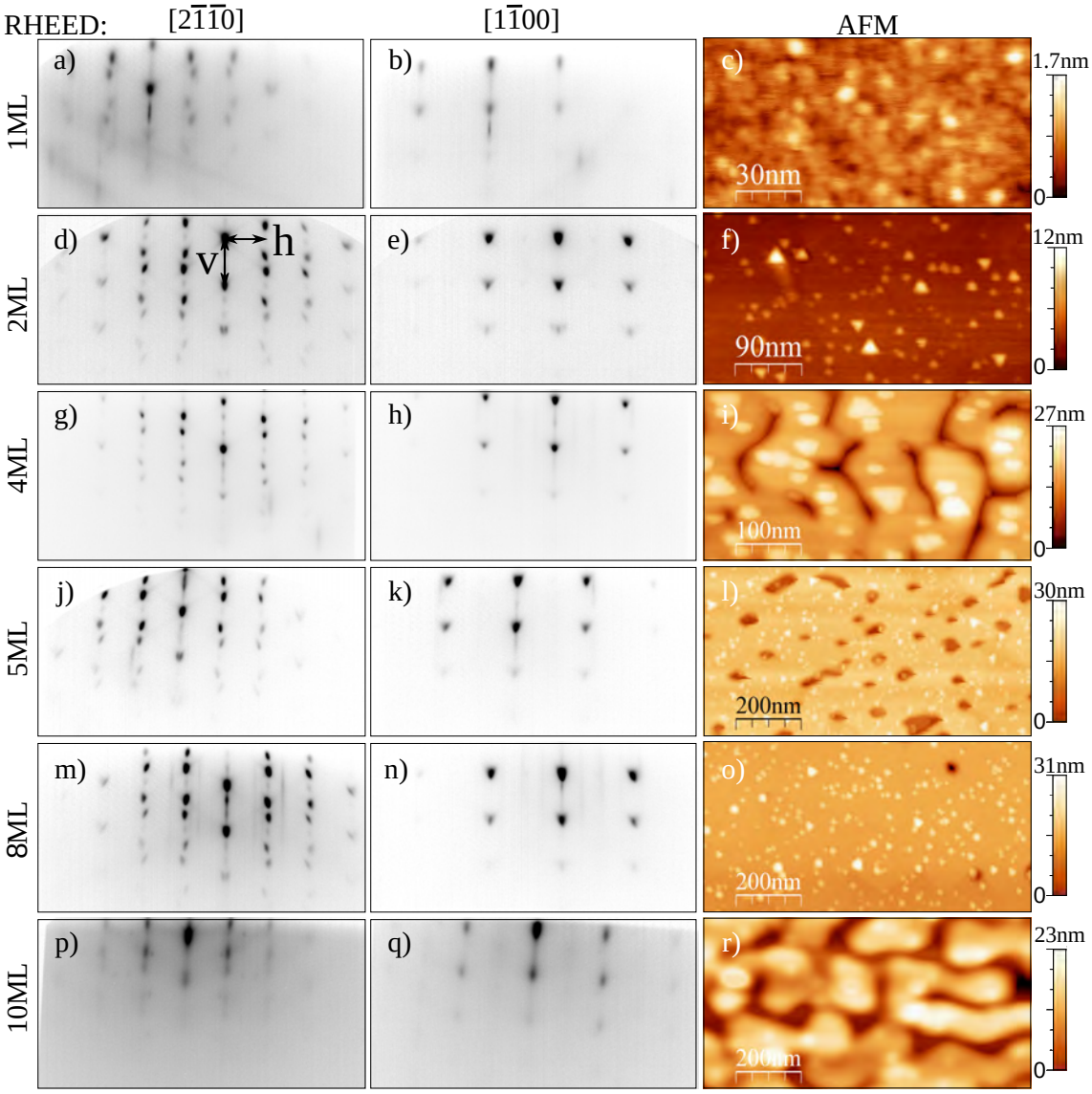

Figure 5.6.: RHEED images along the azimuthal directions [2$\bar{1}\bar{1}$0] and [1$\bar{1}$00] (in hexagonal notation) and AFM images of the samples with nominal Eu coverage of 1, 2, 4, 5, 8 and 10 ML. 1 ML corresponds to an Eu coverages of 3.25 $\AA$. The RHEED patterns reveal the formation of 3D islands. The AFM study shows their truncated pyramidal shape. The tilting of the diffraction spots appears according to the faceting of the truncated tetrahedrons [97]. The background is increased due to the parasitic growth of polycrystalline *bcc* Eu on top and in between the islands [142].

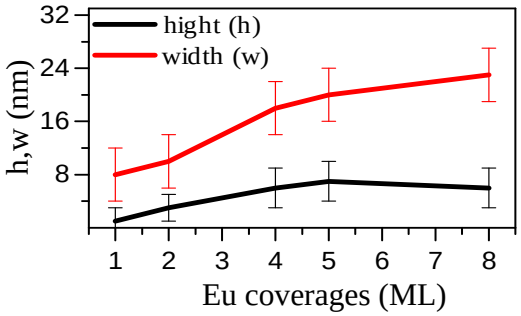

Figure 5.7.: Evolution of the height (h) and width (w) of the islands as a function of the Eu coverage.

Therefore, the Eu islands grow according to the NW orientation relationship on the (110) Nb surface. The RHEED images of the sample with the coverage of 1 ML (Fig. 5.6 a, b)) show relatively weak diffraction spots. With the increase of the Eu coverage sharp diffraction spots are visible (Fig. 5.6 d, e, g, h, j, k)). At a coverage of 8 ML (Fig. 5.6 m, n) the background increases and becomes particularly strong for the coverage of 10 ML (Fig. 5.6 p, q).
The AFM image obtained from the sample covered with 1 ML Eu reveals the formation of small round islands with an average width of $w = 80 \pm 20 \mathring{A}$ and an average height of $h = 8 \pm 5 \mathring{A}$ (Fig. 5.6 c)). However, for the coverage of 2ML triangular shaped islands with the height $h = 100 \pm 30 \mathring{A}$ and width $w = 30 \pm 10 \mathring{A}$ are visible. Some of the islands are rotated by 60° towards the others, following the NW orientation relationship with respect to the Nb buffer layer (Fig. 5.6 f)). With increasing Eu coverage the islands grow laterally as well as in height. The evolution of the average dimensions (average height (h) and width (w)) of the islands as a function of the Eu coverage is plotted in Fig. 5.7.

The increased background in the RHEED images originates from the parasitic growth of *bcc* Eu between and on top of the islands and starts to be pronounced at a coverage of 8 ML. However, the formation of the parasitic *bcc* phase cannot be excluded for smaller coverages. At a coverages of 10 ML large patches most likely of *bcc* Eu are visible in the AFM image that cover the islands (Fig. 5.6 r)).
The systematic AFM study facilitates the interpretation of the electron diffraction patterns, revealing the twinning of the islands (Fig. 5.6 f)). The diffraction pattern has been proven to corresponds to the diffraction pattern from an *fcc* structure. Therefore, in the following the directions will be indexed in the cubic notation with $[2\bar{1}\bar{1}0] \longrightarrow [1\bar{1}0]$ and $[1\bar{1}00] \longrightarrow [11\bar{2}]$, both vectors laying in the *fcc* (111) plane.
The simulated diffraction patterns are shown for the nonequivalent $[1\bar{1}0]$, $[10\bar{1}]$ and equivalent $[11\bar{2}]$, $[\bar{1}2\bar{1}]$ directions, Fig. 5.8 a, b) and Fig. 5.8 d, e), respectively. The diffraction spots are indexed in the cubic notation obeying the selection rules resulting from the structure factor of the *fcc* unit cell [146]. By the superposition of the two diffraction patterns for the nonequivalent directions, the RHEED images along $[1\bar{1}0]$ (hex.$[2\bar{1}\bar{1}0]$), $[11\bar{2}]$ (hex. $[1\bar{1}00]$) and equivalent directions could be reproduced (Fig. 5.8 c, f). The not indexed low intensity diffraction spots originate from double

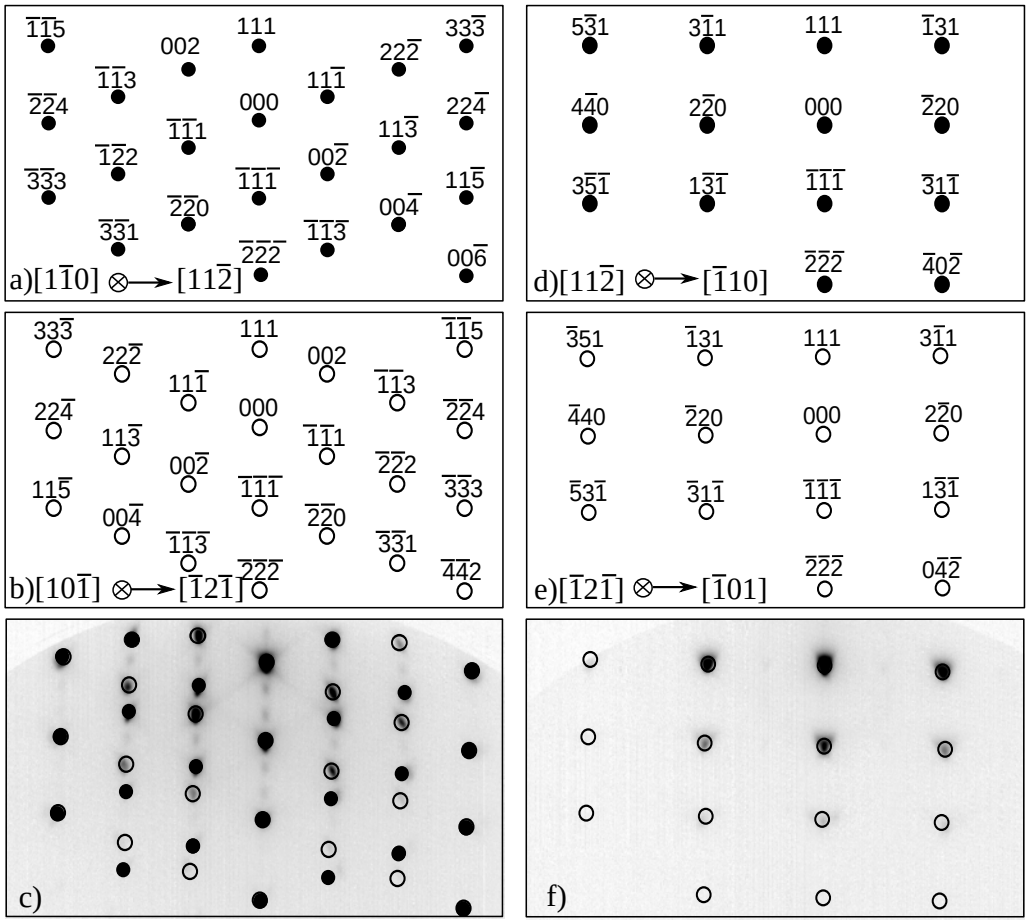

Figure 5.8.: Simulated diffraction pattern of the *fcc* structure along the nonequivalent orientations [1$\bar{1}$0], [10$\bar{1}$] and equivalent directions [11$\bar{2}$], [$\bar{1}$2$\bar{1}$] in the (111) plane. The observed RHEED images in the azimuthal directions c) [1$\bar{1}$0] (hex [2$\bar{1}\bar{1}$0]) and f) [11$\bar{2}$] (hex [1$\bar{1}$00]) in Fig. 5.6 can be reproduced as a superposition of the corresponding diffraction patterns: a)+b) and d)+e), respectively.

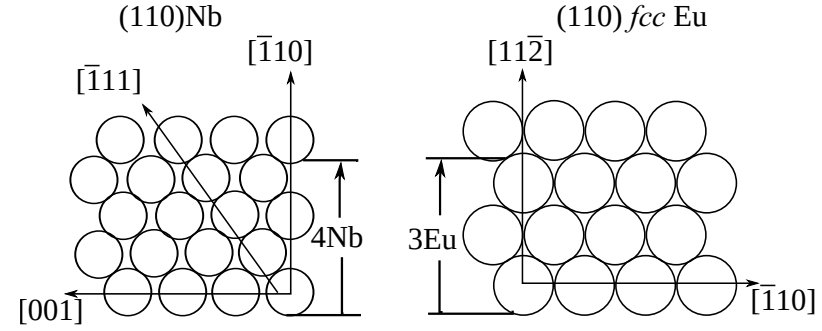

Figure 5.9.: Sketch of the epitaxial relationship between *fcc* (111) Eu and *bcc* (110) Nb, with a 3:4 supercell commensuration of the interatomic distances in the directions [$\bar{1}$10] Nb and [11$\bar{2}$] Eu.

diffraction effects due to the 60° twinning of the islands orientation [147].
The epitaxial relationship between the *fcc* (111)Eu and the *bcc* (110)Nb in the cubic notation is:

$$[\bar{1}10]\text{Nb} \parallel [11\bar{2}]\text{Eu} \quad \text{and} \quad [001]\text{Nb} \parallel [1\bar{1}0]\text{Eu} \tag{5.4}$$

as sketched in Fig. 5.9.

From the RHEED images of smooth surfaces only the in-plane lattice parameters a and b can be derived. In the case of 3D structures, however, due to the transmission of the electrons through the islands the c-parameter and the layer stacking can be identified by comparison with simulated diffraction patterns. The Nb surface lattice parameter was taken as a reference for the derivation of the horizontal lattice spacing h (Fig. 5.6 d). The bulk lattice parameter of Nb is $a_{Nb} = 3.307\mathring{A}$. The horizontal spacing along [001] Nb derived from the RHEED image is $h_{Nb} = a_{Nb}\sqrt{2}/2 = 2.338\,\mathring{A}$. Using this reference, the horizontal lattice spacing between the Eu spots was estimated to be $a_h = 3.6 \pm 0.07\mathring{A}$ (the spacings are indexed with h and v in Fig. 5.6 d)). The derived value implies a 3:4 epitaxial relationship between Eu and Nb. The supercell commensuration along [$\bar{1}$10] Nb ($h_{Nb} = 2.3381\,\mathring{A}$) and [11$\bar{2}$]Eu ($h_{Eu} = 3.1\,\mathring{A}$) is illustrated in Fig. 5.9.
The lattice parameter along the c-axis was estimated by the vertical lattice spacing v along the central diffraction spots in Fig. 5.6 d). The *fcc* structure in the hexagonal basis, with the ABC stacking of (111) planes, is shown in Fig. 5.10. Indicated is the lattice parameter c_v that can be deduced from the RHEED images. The vertical lattice spacing was determined to be $c_v = 3.01 \pm 0.06\,\mathring{A}$ and therefore the lattice parameter c of the *fcc* structure in the hexagonal notation is $c = 9.03\,\mathring{A}$, leading to the ratio $c/a = 2.5$. This ratio is a strong indication for the formation of the *fcc* stacking [148]. The lattice parameter in the cubic description of the *fcc* lattice, is calculated from the horizontal lattice spacing $a_{fcc} = \sqrt{2}a_h = 5.09 \pm 0.09\,\mathring{A}$.
The derived lattice constant and the *fcc* structure of the Eu islands is similar to those of (111)EuO. As it will be proven later in section 5.2.7, the formation of an EuO interface between the oxygen reconstructed (110) Nb surface and the Eu deposit is the reason for the formation of islands with the *fcc* structure, which is unusual for metallic Eu.

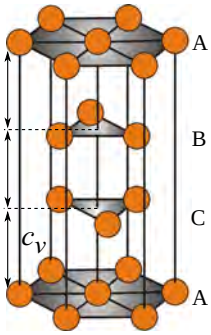

Figure 5.10.: *fcc* crystal structure in the hexagonal basis with the *ABC* stacking of the (111) planes. c_v corresponds to the lattice spacing between the planes.

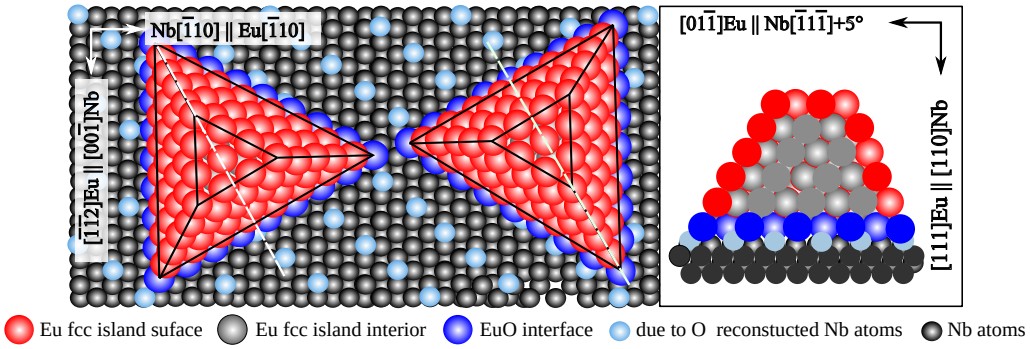

Figure 5.11.: A model of the truncated tetrahedron shaped and 60° twinned islands derived from the results of the RHEED and AFM studies. The main crystallographic orientations are indicated. The white broken line indicates the orientation of the cut shown on the right, displaying the *ABC* stacking of the *fcc* structure.

A model of the *fcc* Eu islands, deduced from the RHEED and the AFM study is shown in Fig. 5.11. The 60° twinning of the orientation of the islands is indicated along with the epitaxial relationships between the (110) Nb surface and the (111)Eu plane. A vertical cut of the island along the white broken lines is also shown. From this cut the Eu atoms belonging to the surface (red), the islands interior (gray), the EuO interface (blue), the due to oxygen reconstructed atoms (light blue) and the Nb atoms (dark gray) are visible.

5.2.4. Ultra-thin Eu films

Eu deposition at $T_S = 423\,K$ on the reconstructed (110) Nb buffer layer leads to the formation of a film with hexagonal symmetry and smooth surface, as reported by Soriano *et al.* [18]. However, the first stages of the growth are not investigated until now.
Fig. 5.12 shows selected RHEED and AFM images from the samples with the Eu coverage of 1 and 7 ML deposited with a rate of 18 $\AA$/min on the oxygen reconstructed

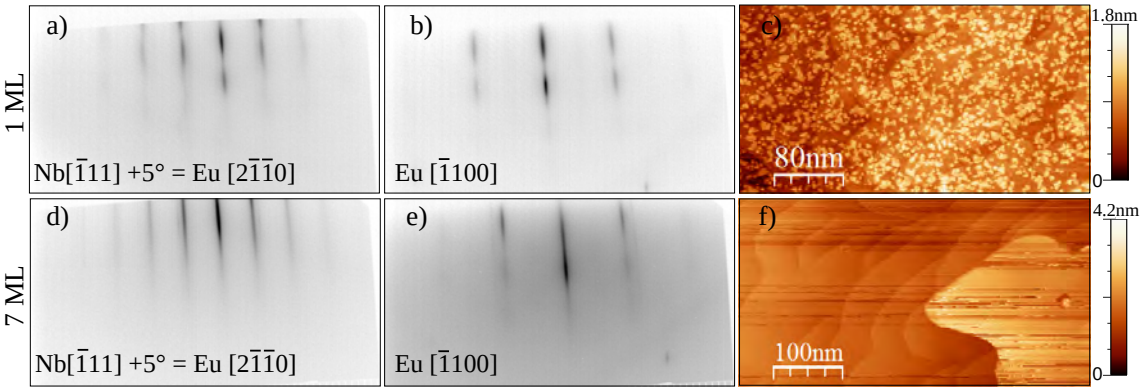

Figure 5.12.: RHEED and AFM images, obtained from Eu films with coverages of 1 and 7 ML, grown at $T_S = 423$ K on the reconstructed (110) Nb surface. The RHEED images are shown along the [2$\bar{1}\bar{1}$0] a), d) and [$\bar{1}$100] b), e) azimuths, respectively. c) and f) show the corresponding AFM images [142].

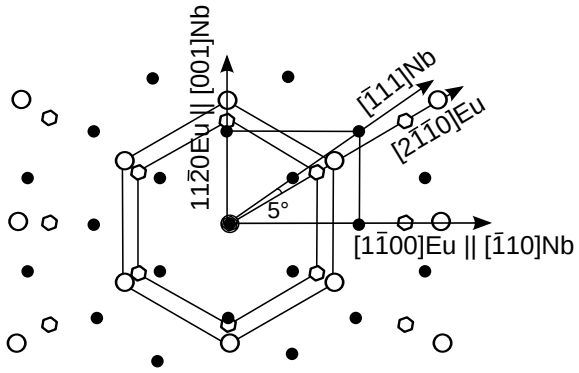

Figure 5.13.: Sketch of the epitaxial relationship between Nb (black circles) and Eu atoms for the coverages of 1 ML (white hexagons) and 7 ML (white circles) based on the measured lattice parameters [142].

(110) Nb surface at a substrate temperature $T_S = 423$ K [18]. The RHEED pattern along [2$\bar{1}\bar{1}$0] and [$\bar{1}$100] azimuths indicate the NW orientation relationship of Eu with respect to the (110) Nb surface. The streaks in the RHEED images of the 1ML covered sample (Fig. 5.12 a), b)) exhibit intensity minima for both orientations, while for 7 ML they are only visible along the [$\bar{1}$100] azimuth (Fig. 5.12 e)). Electron diffraction from single crystalline islands with a high ratio of their lateral width to their height result in a RHEED pattern exhibiting vertical streaks with intensity minima along the vertical streak [97]. A similar pattern is observed for the coverage of 1 ML (Fig. 5.12 a)). This observation is confirmed by the AFM study of the 1 ML covered sample, presented in Fig. 5.12 c), revealing the formation of single crystalline patches/islands with an average width and height of 60 ± 6 Å and 5 ± 2 Å, respectively. The AFM study of the sample with 7 ML Eu coverage, shows that at this coverage already smooth terraces with the width 50 ± 20 nm and length 300 ± 150 nm are formed, corresponding to the intensity distribution without the minima in the RHEED image Fig. 5.12 d).

The horizontal inter streak distance in the RHEED images was used to derive the in-plane lattice parameters of Eu, taking the distance between the (110) Nb surface streaks as a reference, as described in the previous section. For the 1 ML covered sample the in-plane lattice parameter was determined to be $a_{1ML} = 3.65 \pm 0.07\,\mathring{A}$. For 7 ML coverage the in-plane lattice parameter is $a_{7ML} = 4.3 \pm 0.05\,\mathring{A}$ that coincides with the results from Soriano *et al.*, obtained from a sample with an Eu coverages of 9.2 ML($3\,\mathring{A}$).
Fig. 5.13 shows a sketch of the epitaxial relationship between the Nb and Eu atoms for 1 ML and 7 ML coverages. By increasing the Eu coverage, the epitaxial relationship between Nb and Eu atoms is not changing but a relaxation in the nearest neighbor distance takes place. The nature of this intermediate surface structure will be revealed in section 5.2.7. The horizontal streak spacing in the RHEED images was found to be constant for coverages exceeding 7 ML, implying a constant in-plane lattice parameter.
Coverages of Eu above 11 ML lead in all studies to a relaxation from the hexagonal structure with [0001] growth direction, to the *bcc* structure with [110] as growth direction. Two KS orientation relationship with respect to the underlying hexagonal structure are possible. This is in agreement with the results reported by Soriano *et al.* [18].

5.2.5. Wire-like Eu nanostructures

The (110) Nb buffer layer grown at $T_S = 423$ K on the A-plane Al_2O_3 forms a wire-like structured surface shown in Fig. 5.5. Eu was deposited on this buffer layer at a substrate temperature of $T_S = 423$ K. The RHEED and AFM study of the structure and morphology as a function of the Eu coverage is shown in Fig. 5.14. The RHEED images reveal an evolution of the surface morphology with increasing Eu coverage. At a coverage of 2 ML of Eu, the RHEED image exhibits vertical streaks originating from the epitaxial growth of Eu on the buffer layer (Fig. 5.14 a)). The hexagonal notation was chosen because of the 3 fold rotational symmetry and a ratio of $\sqrt{3}$ between the horizontal inter streak distances in the RHEED images along the $[11\bar{2}0]$ and $[1\bar{1}00]$ directions, Fig. 5.14 a), b). The epitaxial relationship deduced from the rotational symmetry of the RHEED images and the horizontal inter streak distance is sketched in Fig. 5.15.
The horizontal spacing between the Nb streaks in the [001] Nb || $[11\bar{2}0]$ Eu direction, corresponds to $h_{Nb} = 2.338\,\mathring{A}$ (marked with horizontal black arrow Fig. 5.14 a). Thus, the horizontal streak spacing of Eu was determined to be $h_{Eu} = 3.60 \pm 0.08\,\mathring{A}$. Therefore, the lattice constant of Eu in hexagonal symmetry is $a_h = 4.1 \pm 0.1\,\mathring{A}$. With increasing Eu coverage the streaks in the RHEED images along $[11\bar{2}0]$ (Fig. 5.14 d, g) disappear while the horizontal streak spacing of Eu is not changing. The streaks in the RHEED images belonging to Eu and Nb are indicated with vertical black arrows (Fig. 5.14). Transmission spots appear at a coverage of 5 ML Eu ($[1\bar{1}00]$ Fig. 5.14 g, h)), indicating the formation of islands while the streaks of the Nb surface are still visible.

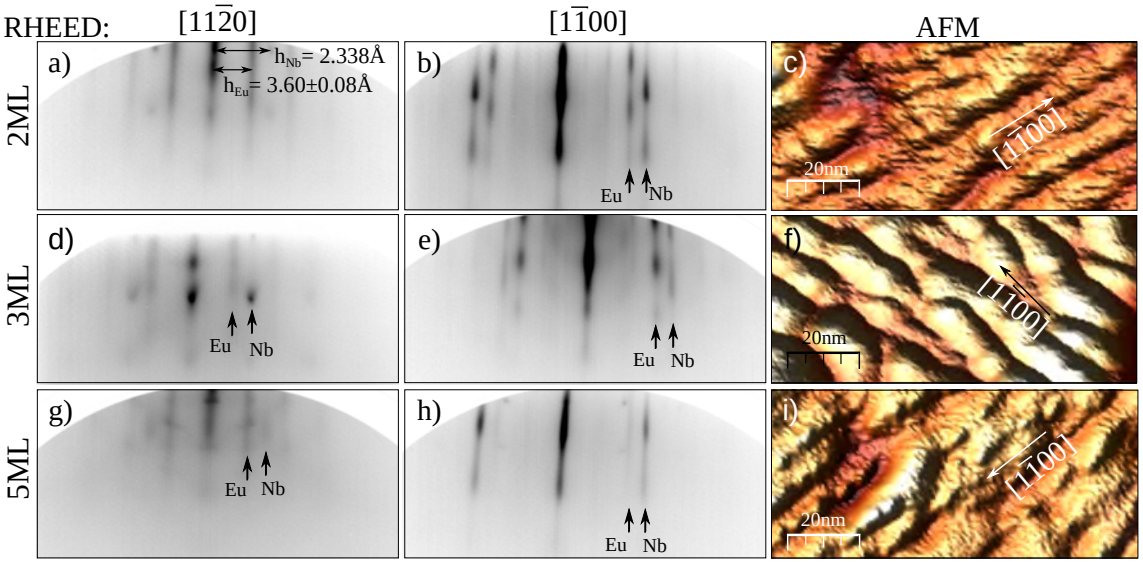

Figure 5.14.: Results from the RHEED and AFM study of samples with an Eu coverage of 2 ML, 3 ML and 5 ML, deposited at a substrate temperature of $T_S = 423$ K, on (110) Nb with a wire-like surface morphology. The RHEED images are obtained along the [11$\bar{2}$0] and [1$\bar{1}$00] directions (in hexagonal notation). Black vertical arrows indicate the position of Eu and Nb streaks in the RHEED images for both directions. In the AFM images the alignment along [1$\bar{1}$00]Eu ∥ [$\bar{1}$10] Nb of the nanostructures are indicated with black and white arrows.

The AFM images reveal the formation of a wire-like structure for all Eu coverages (Fig. 5.14 c, f, i)). The obtained average dimensions are summarized in Table 5.1. In comparison to the steps formed on the (110) Nb buffer layer, the length of the wire-like Eu structures is reduced, while the height remains constant with increasing Eu coverage. For the coverage of 5 ML in addition to the steps islands are visible. The width of the steps increases for 3 ML and decreases again for 5 ML coverage. This behavior can be explained taking the RHEED images into account. The epitaxial growth can not be continued for coverages higher than 3 ML. The strain is released by the formation of islands visible as blurred spots in the RHEED images for 5 ML sample. This conclusion is supported by the increased background of the RHEED images of this sample most likely originating from the formation of polycrystalline *bcc* Eu phase.

	length (nm)	width (nm)	height (nm)
buffer	293 ± 144	12.9 ± 2.4	0.5 ± 0.2
2ML	93 ± 30	8.9 ± 2.2	0.6 ± 0.24
3ML	68.75 ± 28	16.7 ± 4.0	0.65 ± 0.3
5ML	68.2 ± 29	6.9 ± 2.5	0.57 ± 0.26

Table 5.1.: Size evolution of the wire-like structures formed on the surface shown in Fig.5.14 c, f,g), for the Eu coverage of 2, 3 and 5 ML. The corresponding values for the (110) Nb buffer layer (Fig. 5.5 c)) are given for comparison.

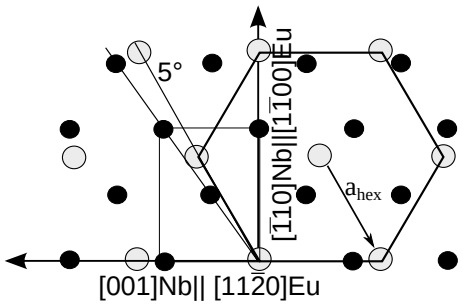

Figure 5.15.: Epitaxial relationship between the oxygen-free (110) Nb surface grown at $T_S = 423\,K$ (black circles) and Eu deposited at $T_S = 423\,K$ (white circles) based on streak spacings and rotational symmetry deduced from the RHEED study. The results indicate a NW orientation relationship of Eu with respect to the Nb surface.

Soriano *et al.* [18] reported the formation of *bcc* Eu islands at the same growth conditions (substrate temperature of $T_S = 423\,K$ on a (110) Nb surface without the oxygen induced reconstruction). A smooth (110) Nb surface was concluded from their RHEED study [18]. These results could not be reproduced in the present study most likely due to a different morphology of the surface. However, the results of the first stages of Eu growth (2 ML coverage) are in agreement with the study of Eu grown at $T_S = 423\,K$ on a (110)V surface without an oxygen reconstruction [20]. There, the formation of a film with hexagonal symmetry is reported. The hexagonal symmetry persists up to a few tens of $\AA$ [20]. The morphology of the (110)V surface was investigated by RHEED. A stepped surface morphology was not reported, most likely because instead of a buffer layer grown on Al_2O_3, a (110)V single crystal was used. The lattice constant of $a = 4.1\AA$ [20] is in agreement to the results of the present study.

5.2.6. XPS study of Eu films and nanostructures

In addition to the RHEED and AFM study, XPS was used for the investigation of the chemical composition of the surfaces of all samples. XPS spectra of samples with a nominal coverage of 4 ML deposited at different growth temperatures on (110) Nb buffer layers (grown at $T_S = 423\,K$ and $T_S = 1173\,K$) are shown in Fig. 5.16. The energy range $E_B = 540 - 350\,eV$ was chosen because it contains O and Nb core levels as well as an Eu Auger line. The spectra are displayed with the intensity of the Nb$3p_{\frac{1}{2}}$ core level peaks normalized to 1. Shown with blue lines (light and dark blue) are the XPS spectra of Eu grown on the (110) Nb surface with an O induced reconstruction ($T_S = 1173\,K$), while dark red and magenta colored spectra correspond to Eu grown on the surface without O induced reconstruction ($T_S = 423\,K$). The substrate temperature during Eu deposition was $T_S = 423\,K$ and $T_S = 533\,K$. Spectra of the clean buffer layers with (blue dashed line) and without (red dashed line) oxygen reconstruction are included for comparison.
The XPS spectra of the clean O reconstructed (110) Nb layer (Fig. 5.16 HT, blue

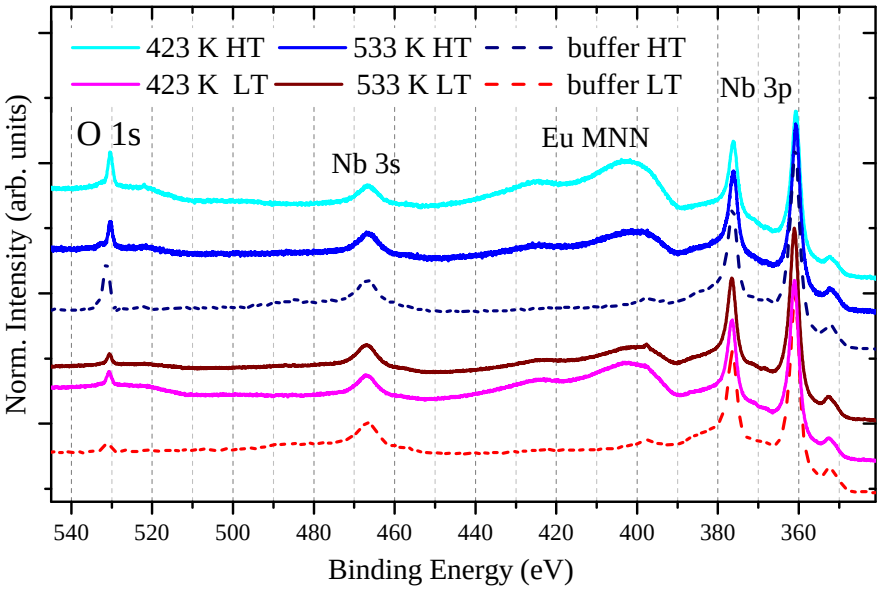

Figure 5.16.: Comparison of XPS spectra from samples with a coverage of 4 ML Eu deposited at 423 K (light blue line) and 533 K (blue line) on an oxygen induced surface reconstruction of Nb (blue dashed line) and on a Nb surface without surface reconstruction (red dashed line) at 423 K (magenta line) and 533 K (dark red line).

dashed line) exhibit the O 1*s* core level peak at the binding energy position of E_B = 531.2 eV. The deposition of either Eu islands (Fig. 5.16 blue line) or Eu film (Fig. 5.16 light blue line) is not changing the ratio between the peak areas of the O 1*s* peak and the Nb 3*p* peaks (within 1%) in comparison to that of the clean Nb surface before Eu deposition. The position of the O 1*s* peak is slightly shifted to E_B = 530.6 eV for the Eu islands (Fig. 5.16 blue shaded lines). The small shift indicates changes in the chemical bonding of O, most likely induced by a chemical reaction with Eu atoms. The positions of the Eu peaks, however, remain unchanged.

No changes of the O 1*s* core level peak at E_B = 531.2eV is observed for the samples grown on buffer layers without surface reconstruction (Fig. 5.16 LT). Peak area and position remain unchanged for both Eu deposition temperatures T_S = 423 K and T_S = 533 K.

The formation of EuO on the O reconstructed (110)V surface has been proposed as the reason for the stabilization of *fcc* Eu islands [20]. However the Eu 4*p* binding energy for metallic Eu and EuO are very similar [149] making them difficult to distinguish.

Fig. 5.17 compares XPS spectra of clean buffer layers and the spectra of two samples with a coverage of 4 ML, grown at T_S = 423 K (film) and T_S = 533 K (islands) in the region of the Eu 4*d* core level peak.

The position of the Eu3+ contribution is reported by Altendorf *et al.* to be at E_B = 143 eV [149]. To visualize the influence of oxides with higher valency than 2+, the spectra of an at air oxidized sample with islands surface morphology (Fig. 5.17 green line) is shown. There, the Eu3+ contribution appears at a binding energy

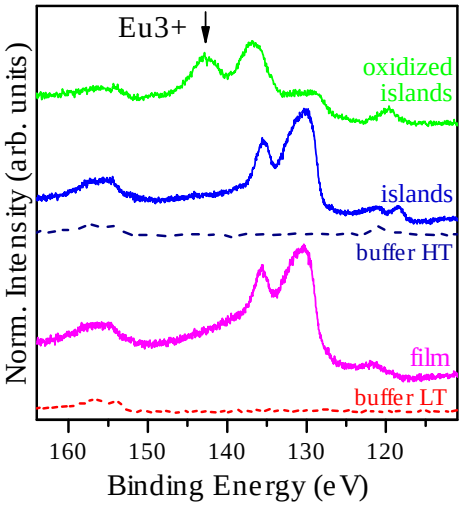

Figure 5.17.: XPS spectra of the Eu 4*d* peak of samples with Eu coverage of 4 ML exhibiting either the islands (blue) or film (magenta) surface morphology. The spectra of the buffer layers with (blue dashed line) and without (red dashed line) the O surface reconstruction are added for comparison. The spectra of an at air oxidized sample with islands (green line) exhibits an Eu3+ contribution that appears at a binding energy of $E_B = 143$eV.

of $E_B = 143$ eV and is dominating the Eu2+ contribution. In the samples grown at $T_S = 423$ K (Fig. 5.17, film) and $T_S = 533$ K (Fig. 5.17, islands) no traces of Eu with the valence of 3+ and therefore, no Eu_2O_3 or higher oxides are formed during the growth process.

5.2.7. Investigation of Eu islands and films by NFS

As it was demonstrated above, it is difficult to distinguish between metallic Eu and EuO from the XPS study and therefore to proof the formation of EuO at the interface between the *fcc* Eu islands and the (110) Nb surface. However, with nuclear forward scattering it is possible to unambiguously confirm the presence of EuO as it is shown in the following.

Experimental details

The samples were prepared in the UHV chamber installed at the beamline ID18 of the ESRF (Fig. 2.11). The growth conditions for the samples established in the UHV-Analysis lab at ANKA, KIT were optimized for this chamber.
Nb metal was evaporated from a rod with 99.9% purity (GoodFellow) by a flux controlled electron beam evaporator with a rate 1.8 Å/min. Vacuum outgassed and to 96% in ^{151}Eu isotopically enriched metallic Eu (Oak Ridge National Laboratory) was evaporated from an effusion cell using a Ta crucible and deposited with a rate of 10 Å/min. The deposition rate was precisely calibrated with a quartz oscillator prior to the growth. The quality of the samples was controlled by RHEED. The NFS

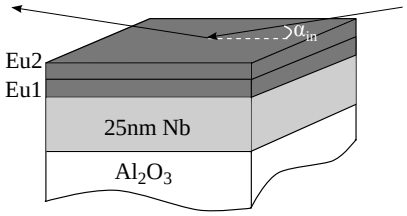

Figure 5.18.: Model of the sample containing the Al_2O_3 substrate, the (110) Nb buffer layer and two Eu layers, which was used to fit the NFS spectra with the CONUSS software [150]. The Eu layers have their own set of hyperfine interaction parameters. α_{in} stands for the incidence angle of the X-rays towards the sample surface.

measurements were performed at the ^{151}Eu resonance energy $E_0 = 21.5412\,\text{keV}$, at grazing incidence scattering geometry. The experimental setup is described in section 2.3.3.

Data analysis

Samples with a nominal coverage of 2, 4, 5 and 8ML were prepared with the growth conditions leading to the formation of *fcc* islands ($T_S = 533\,K$ during Eu deposition on the oxygen reconstructed (110) Nb surface). The NFS experiment was performed *in situ* at a substrate temperature of $T_S = 111\,K$ and at a preasurre of 5×10^{-11} mbar. The analysis of the NFS spectra was done using the CONUSS software [150]. The parameters that define the ^{151}Eu nuclear transition are summarized in Tab. 5.2. A magnetic ordering of the sample constituents is excluded because the magnetic ordering temperature of metallic Eu is $T_{Néel} = 91\,K$ and of EuO it is $T_{Curie} = 69\,K$ [136]. The NFS measurements were performed at a constant sample temperature $T_S = 111\,K$ i.e. above the magnetic ordering temperatures. The case without the magnetic hyperfine splitting of the nuclear states simplifies the NFS spectra to a great extent (Fig. 2.9), because the nuclear states are not degenerated. The penetration depth of X-rays with an energy $E_{^{151}Eu} = 21.5412\,\text{keV}$ [49] is $d_{21.5412keV} = 151.2\,\AA$ at the critical angle for Eu $\alpha_{Eu} = 0.197\,\text{mrad}$. Therefore, by taking the island height into account X-rays are penetrating through the entire island even for the highest Eu coverages. Hence, a simplified model consisting of the layer system Al_2O_3/25 nm Nb/Eu1/Eu2 was assumed for the fit of the NFS spectra. A sketch of this model is shown in Fig. 5.18.
Fig. 5.19 shows the experimental NFS spectra as black circles for the coverages of 2, 4, 5 and 8 ML. The sample with 184 ML (600 $\AA$) Eu coverage is termed bulk. The fits to the NFS data, assuming the model (Fig. 5.18) are shown with red lines.

The spectra of the samples with an Eu coverage of 4, 5 and 8 ML exhibit the presence of a beating with the frequency $f = 15 \pm 1\,\text{ns}$. An onset of the beats with the same frequency is also visible for the sample with 2 ML Eu coverage. However, due to the low count rate the evaluation of the 2 ML spectrum is difficult. As expected the NFS spectrum of the bulk-like sample exhibits a single-

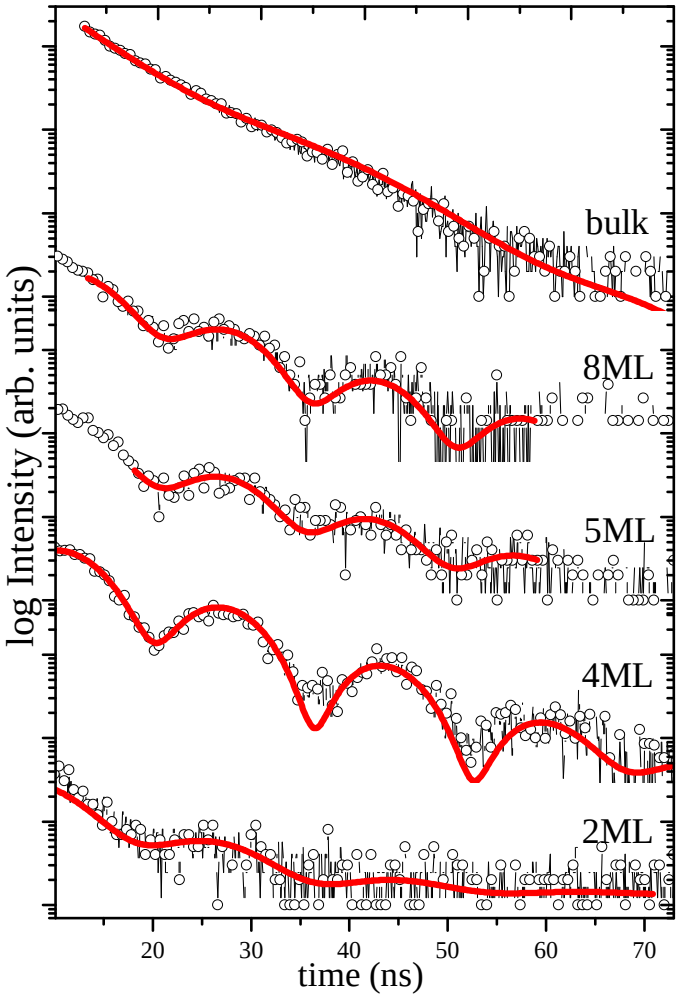

Figure 5.19.: NFS spectra of the *fcc* Eu island samples with a nominal coverage of 2, 4, 5 and 8 ML. The spectrum of a bulk *bcc* Eu sample is shown for comparison.

Table 5.2.: Nuclear properties of ^{151}Eu, used to define the Mössbauer transition in the input files for the CONUSS program [150] (with the nuclear magneton $\mu_N = 5.058 \cdot 10^{-27}$J/T and 1barn= 10^{-28}m^2). The values are taken from [34, 36]. * An enrichment to 96% in ^{151}Eu was assumed for the fit.

^{151}Europium	parameter	value
isotope mass	M	$151\,u$
natural abundance	β_{nat}	47.82*
transition energy	E_0	21531 eV
wavelength	λ_0	$0.5758\,\mathring{A}$
recoil energy	E_R	1.65 meV
lifetime	τ	13.99 ns
halflife	$\tau_{1/2}$	9.5 ns
natural width	Γ_0	47.03 neV
internal conversions coefficient	α	28
nuc. ang. moment	I_g	$^{+}7/2$
	I_e	$^{+}5/2$
resonance cross section	σ_0	242.6 kbarn
electronic cross section	σ_{el}	8.35 kbarn
transition multipole character	$M1 + E2$	M1 dominant
nuc. quadrupole moment	Q_g	0.903 barn
	Q_e	1.28 barn
nuc. magnetic moment	μ_g	$3.472\,\mu_N$
	μe	$2.591\,\mu_N$

line exponential decay. The values of the fit parameters are summarized in Table 5.3.

The influence of the hyperfine interactions at the nucleus on the nuclear energy levels was described in section 2.2.2 and the influence of the hyperfine interaction on the NFS was visualized in Fig. 2.9. The chemical bonding of the O atoms to the Eu atoms leads to a small shift of the nuclear energy levels of ^{151}Eu in EuO in comparison to the energy levels of metallic Eu. The interference of the plane waves emitted during the de-excitation of the excited nuclear levels of ^{151}Eu in the metallic Eu and EuO results in beats that are visible in the NFS spectrum. The frequency of the beating is directly related to the isomer shift (IS). The *IS* is measured in mm/s that originates from Mössbauer spectroscopy and 10 mm/s correspond to a shift of 72.4×10^{-8} eV. The thickness of the first layer Eu1 is $d_{E1} = 6\,\mathring{A}$. The height of the second layer (Eu2) corresponds to the average height of the islands.

Fig. 5.20 shows isomer shifts for several Eu compounds and oxides, visualizing the shift in different directions for the 2+ and 3+ valency. The isomer shift of EuO (valency 2+) is $IS_{Eu-EuO} = -3.1$ mm/s, while in Eu_2O_3 (valency 3+) it is $IS_{Eu-Eu_2O_3} = 7.8$ mm/s [52], both values are expressed relative to metallic Eu.

Table 5.3.: Parameters derived from the fit of the experimental NFS data using the model shown in Fig. 5.18. 10 mm/s corresponds to an isomer shift of 71.8×10^{-8} eV.

	h_{Eu1} (Å)	h_{Eu2} (Å)	α_{in}(mrad)	IS (mm/s)
2ML	6	156	1.999	3.19
4ML	5	159	1.860	3.59
5ML	6	193	1.901	3.65
8ML	6	207	1.839	3.63
bulk	0	600	1.866	-

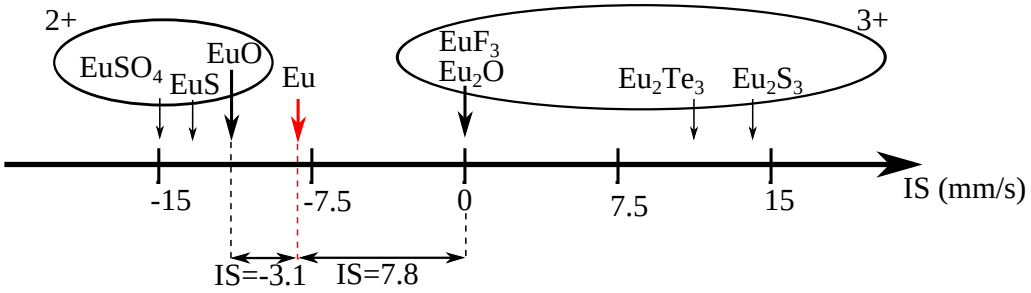

Figure 5.20.: Isomer shifts of various Eu containing compounds for the nuclear excitation at $E_{^{151}Eu} = 21.5412$ keV of ^{151}Eu. The shifts are given relative to EuF_3. The values, taken from the literature [52] visualize the isomer shifts of Eu compounds exhibiting a valency of 2+ and 3+.

The results from the fit of the NFS data unambiguously confirm that EuO is formed at the interface between the metallic *fcc* Eu islands and the due to oxygen diffusion reconstructed (110) Nb surface. Even if the isomer shift revealed from the NFS fits is by $\Delta IS = -0.5$ mm/s higher, in comparison to the reported value of $IS_{EuO-Eu} = -3.1$ mm/s [52], the Eu2+ valency and therefore the formation of EuO is evidenced [136, 151].

Fig. 5.21 shows a comparison of the NFS spectra of two samples prepared at different conditions. Both samples have the same nominal Eu coverage of 10 ML. The substrate temperature during the Eu deposition is $T_S = 423$ K, resulting in a film and $T_S = 533$ K, resulting in *fcc* islands. The growth conditions for the buffer layers ($T_S = 1173$ K) were the same for both samples. A single exponential decay is visible in the spectrum (Fig. 5.21) of the film. Contrary, the sample with *fcc* Eu islands shows a beating corresponding to an isomer shift of $IS = -3.6$ mm/s. The same model was assumed for the fit of the experimental NFS data, as shown in Fig. 5.19. Simulations demonstrated that if EuO would be present in the film, a beating should be visible as for the coverage of 10 ML, which is not observed in Fig. 5.21 a).
Already Gourieux *et al.* suggested that a minimum temperature of 533 K is needed for the formation of EuO and *fcc* Eu islands on the (110)V surface [20]. The results from the NFS experiment shown in Fig. 5.21 proof unambiguously that for the formation of EuO a substrate temperature of 533 K is necessary. This result

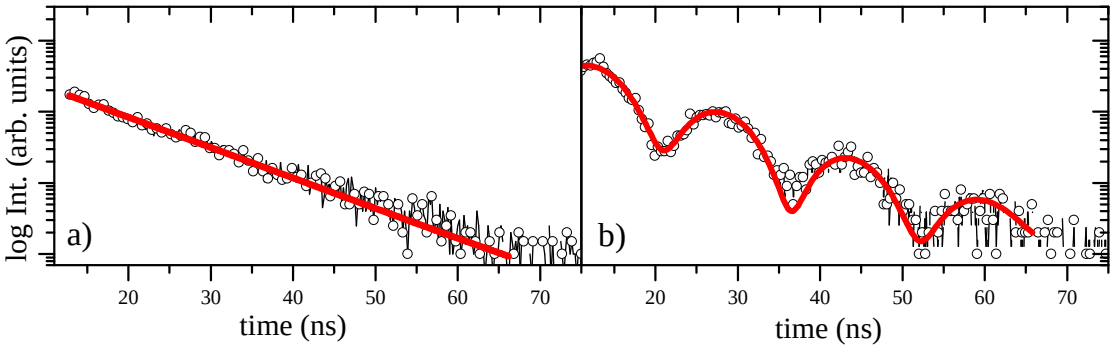

Figure 5.21.: NFS spectra from a nominal Eu coverage of 10 ML forming a) film and b) *fcc* islands. The spectrum of the film shows a single line exponential decay while that of the island shows a beating with one frequency [142].

confirms that the formation of EuO is found to be the origin of the growth and stabilization of the *fcc* Eu islands, as it was suggested in section 5.2.3.

Considering the results from the NFS study the formation of the intermediate phase that appears in the first stages of the Eu growth at a substrate temperature of $T_S = 423\,\mathrm{K}$ on the reconstructed (110) Nb surface can be explained (Fig. 5.12). The relaxation from the lattice constant of $a_{1ML} = 3.65 \pm 0.07\,\mathring{A}$ at a coverage of 1 ML to $a_{7ML} = 4.3 \pm 0.05\,\mathring{A}$ at a coverage of 7 ML cannot be explained by the formation of EuO in the fist layer but has to be explained by the rigid body model, where atoms are treated as rigid spheres. An EuO-type (111)Eu layer stacking is stabilized in the first Eu layers, leading to an epitaxial relationship of 3:4 between the Eu and Nb atoms in the rigid body model. However, a chemical reaction between the Eu and O atoms does not take place at $T_S = 423\,\mathrm{K}$. Due to the missing chemical bonding and the large compressive strain of up to 9.5% in the *fcc* structure in comparison to the *bcc* Eu, this intermediate phase cannot be stabilized for higher Eu coverages. Instead, by increasing the Eu deposit above about $d = 20\,\mathring{A}$ at $T_S = 423\,\mathrm{K}$ [18], the (111) Eu stacking quickly relaxes towards the (0001)Eu film with hexagonal symmetry and the reported lattice constant of $a = 4.27\,\mathring{A}$ [142].

5.3. Lattice dynamics of *fcc* Eu islands

5.3.1. NIS experiment

The *in situ* NIS experiment was performed on samples with the Eu coverage 2, 4, 5 and 8 ML described in the previous section. The samples were kept at $T = 111\,\mathrm{K}$ during the measurement in order to reduce the contributions from multi-phonon excitations that appear as additional background to the single-phonon contribution. The experimental NIS spectra were obtained as a sum over several NIS scans. To exclude the influence of a possible surface contamination during the long measurement time of up to 24h per sample, the summed spectra of the first half of the experiment were compared with the sum of the spectra from the second half,

revealing no detectable differences. Therefore, both sums were used to increase the statistical accuracy. Fig. 5.22 shows the obtained experimental NIS spectra of the investigated samples. All spectra are characterized by the central elastic peak that is proportional to the probability for recoilless absorption/emission of photons, which is the Lamb-Mössbauer factor f_{LM}. The side bands of the NIS spectrum correspond to the creation (positive energy part) and to anihilation (negative energy part) of phonons in the lattice.

From the investigation of the structure with RHEED and AFM, the growth of *fcc* Eu islands and the contribution from parasitic *bcc* Eu growth were demonstrated in section 5.2.3. From the NFS study (section 5.2.7) the formation of EuO at the interface between the *fcc* islands and the due to oxygen diffusion reconstructed (110) Nb surface was evidenced. Therefore, the NIS spectra contain contributions from multiple, chemically different Eu sites.
The total yield of delayed K-fluorescence photons, which form the NIS signal, is proportional to the phonon excitation probability density function (section 2.3.2). In section 2.3.2 the case of a chemically homogenous sample was considered. In the presence of m nonequivalent sites, for example a mixture of pure metal and oxide in the sample, the site-specific phonon excitation probability density function has to be defined. For that purpose Eqn.(2.76) can be written as [152]:

$$S^{(m)}(\vec{k}_0, E) = \frac{1}{2\pi} \int e^{-iEt - \frac{\Gamma_0 t}{2}} F^{(m)}(\vec{k}_0, t) dt = \sum_{n=0} S_n^m(\vec{k}_0, E) \ . \tag{5.5}$$

$F^m(\vec{k}_0, t)$ is the site-specific correlation function and Γ is the natural line width at the nuclear transition energy. Thus, the projected, site-specific phonon DOS can be written similarly to Eqn.(2.89):

$$\tilde{g}^m(E, s) = V_0 \frac{1}{(2\pi)^3} \sum_j \int d\vec{q}\ \delta\Big(E - \hbar\omega_j^m(\vec{q})\Big) \left| s \cdot \vec{e}_j^m(\vec{q}) \right|^2 \ , \tag{5.6}$$

with site-specific polarization vectors $e_j^m(\vec{q})$ along $s = \vec{k}_0/k$, the normalized incident wave vector, V_0 is the volume of the unit cell and the sum runs over the phonon branches j of the site-specific dispersion relations $\hbar\omega_j^m$. The integral over the phonon momentum $\vec{q}$ is within the first Brillouin zone of the mth site.
From NIS measurements alone neither the site-specific phonon DOS nor the f_{LM} factors can be derived for multiple non equivalent sites. This is *only* possible, when the corresponding f_{LM} factors are sufficiently high, so that multiple phonon contributions (n=2,3..., proportional to $1 - f_{LM}$) can be neglected, or in cases where the resonant nuclei are situated in almost identical environments, for example in amorphous materials [152]. Therefore, the extraction of the site-specific phonon DOS can not be done by applying the standard formalism described in section 2.3.2. As it will be shown in the following it is, however, possible to determine the site specific phonon DOS by the help of first principles calculations.

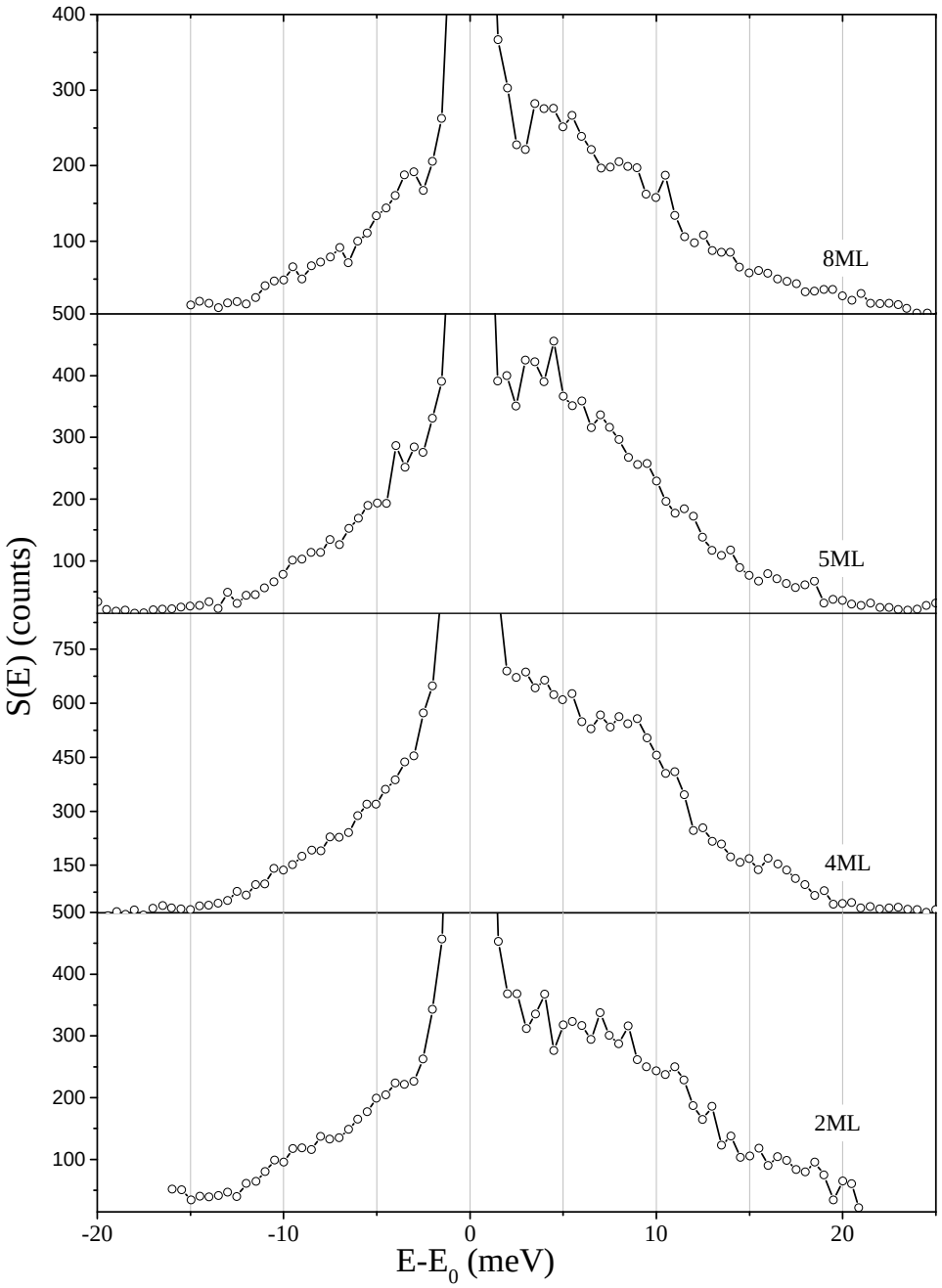

Figure 5.22.: Experimental NIS spectra obtained from the summation of several NIS scans measured at 111 K for samples with the Eu coverage of 2, 4, 5, and 8 ML.

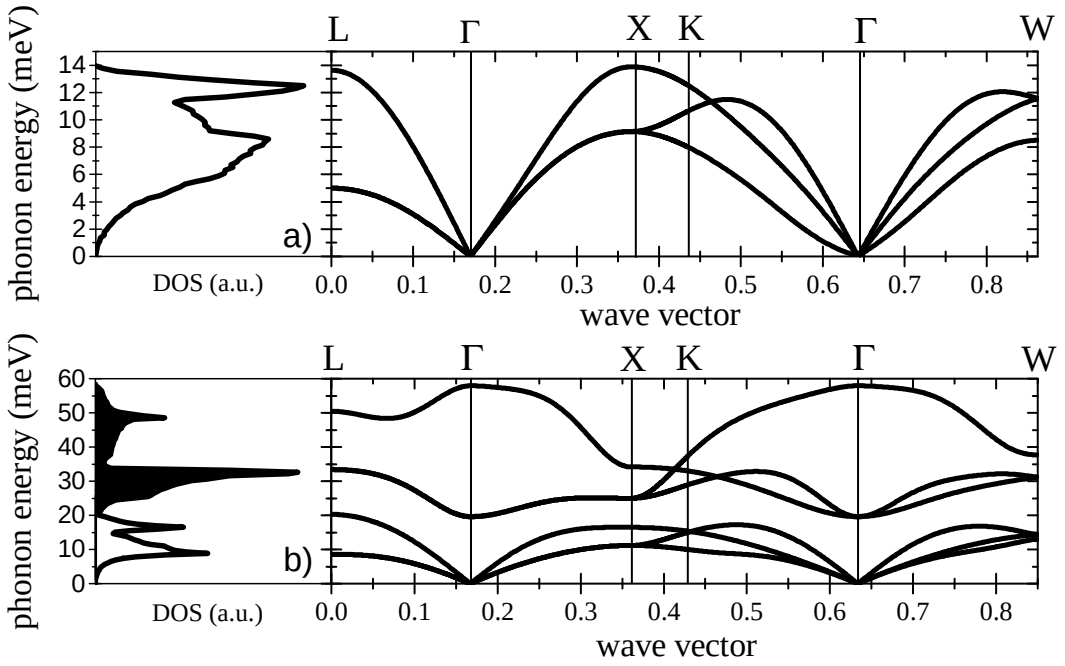

Figure 5.23.: The *ab initio* calculated phonon density of states (left) and phonon dispersion relations (right) along high symmetry directions of a) *fcc* Eu and b) EuO single crystal. The filled black spectra in b) shows the O-partial phonon DOS while the solid line stands for the Eu partial phonon DOS in EuO.

5.3.2. *Ab initio* calculations

The phonon dispersion relations and phonon DOS of *fcc* and EuO were calculated by DTF using the experimentaly derived lattice constants[1]. The results of the calculations are shown in Fig. 5.23. The phonon densities of states are plotted on the left, while the corresponding dispersion relations along the high symmetry directions are shown on the right. The phonon DOS of *fcc* Eu crystal consists of a high-energy longitudinal mode at 12 meV and transverse modes with the maximum at 8 meV (Fig. 5.23 a). The phonon spectrum of EuO includes contributions from Eu (solid line) and O atoms (filled area), extending up to 60 meV Fig. 5.23 b). The Eu-partial DOS is characterized by peaks at 9 meV and 16.5 meV, and a high energy cut-off at 20 meV.

[1] The *ab initio* calculations were performed by the Group of P.Piekarz from the Institute of Nuclear Physics, Polish Academy of Sciences, Krakow using the density functional theory implemented in the VASP program [41]. The ferromagnetic spin order on Eu atoms is assumed in all systems. EuO is a Mott insulator. The strong local Hubbard interaction ($U = 8.3\,\mathrm{eV}$) and Hund's exchange ($J = 0.8\,\mathrm{eV}$) [153] were included within the LDA+U method [154]. The calculated band gap of 1.05 eV between the $4f$ and $5d$ states corresponds to the experimental value of 1.12 eV [155]. The optimized lattice parameter for the EuO crystal ($a = 5.18\,\mathring{A}$) agree with the measured value ($a = 5.14\,\mathring{A}$). The nearest Eu-Eu distance (experimental value ($3.6 = \mathring{A}$)) was fixed by the lattice constant of the *fcc* Eu crystal, that was set to $a = 5.1\,\mathring{A}$.

5.3.3. Phonon DOS

Using the *ab initio* calculated phonon DOS for *bcc* Eu, *fcc* Eu and EuO, the f_{LM} can be calculated from Eqn.(2.84). From the f_{LM} the relative contributions of various orders of phonon excitations can be obtained by [36]:

$$\int S_n^m(E)dE = \frac{(-\ln f_{LM}^m)^n}{n!} \ . \tag{5.7}$$

The values for f_{LM} and the various phonon contributions are summarized in Table 5.4. EuO has the highest f_{LM} implying the lowest contribution of multi-phonon excitations. The f_{LM} of *bcc* Eu is by 48% smaller, therefore the probability for the excitation of multiphonons ($n > 1$) in EuO is negligible, while it is significant up to $n = 3$ for *bcc* Eu. The rather high f_{LM} values of all components enable a quantitative and qualitative evaluation of the NIS spectra. Using Eqn.(2.85) NIS spectra can be calculated from the *ab initio* calculated phonon DOS. Fig. 5.24 shows the inelastic part of the NIS spectra calculated from the *ab initio* phonon DOS of *bcc* Eu, *fcc* Eu and the Eu partial phonon DOS of EuO at 100 K. The black line denotes the $S_n(E)$ (all phonon excitations), while the red line stands for the $S_1(E)$ (single phonon) contribution.
Lipkin's sum rules imply the normalization of the NIS spectra to the recoil energy (E_R) [60]:

$$\int E\ S(E)dE = E_R \ , \tag{5.8}$$

The central elastic peak contributes equally to the positive and negative side of the integral and can be excluded.

It is well known that the features of the phonon DOS of nanocrystalline materials and nanoparticles are broadened in comparison to that of the bulk [156]. This broadening can originate from anharmonic interatomic potentials created by atoms in irregular sites of grain boundaries or strained lattices. It has been demonstrated that these effects can be reliably accounted for by a convolution of the phonon DOS of the bulk counterpart with the damped harmonic oscillator (DHO) function [32, 36, 156]:

$$\mathrm{DHO}_{E'}(E) = \frac{1}{\pi Q E'} \frac{1}{(\frac{E'}{E} - \frac{E}{E'})^2 + \frac{1}{Q^2}}. \tag{5.9}$$

Q is the number of cycles for which the fraction of e^{-1} of the phonons will remain and is the *quality factor* [32]. E is the energy range around the phonon of energy

Table 5.4.: Calculated Lamb-Mössbaer factors f_{LM} at $T = 100$ K and the contributions of the site specific n-phonon terms using Eqn.(5.7).

	f_{LM}	$n=2$	$n=3$	$n=4$
bcc Eu	0.37	0.505	0.169	0.042
fcc Eu	0.47	0.285	0.072	0.013
EuO	0.72	0.063	$7.5E^{-3}$	$6.7E^{-4}$

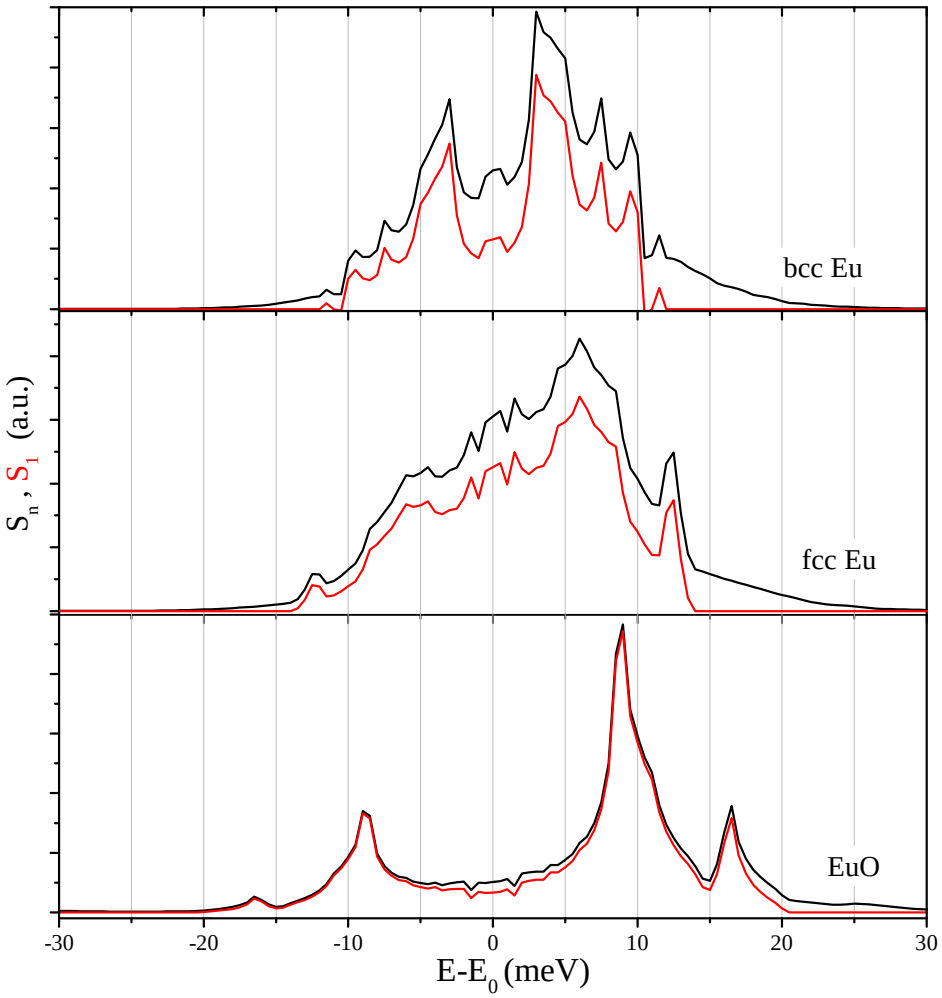

Figure 5.24.: The single phonon (red) and the (total) multiphonon (black) contributions to the NIS spectra of *bcc* Eu, *fcc* Eu and EuO (Eu partial) bulk crystals. The spectra are obtained from the *ab inito* phonon DOS calculated at 100 K.

Table 5.5.: Results from the best fit of Eqn.(5.10) to the experimental data with the *quality factors* Q_m and the partial contributions A_m of *fcc* Eu, *bcc* Eu and EuO being fit parameters.

	A_{fcc}	Q_{fcc}	A_{bcc}	Q_{bcc}	A_{euo}	Q_{euo}
2ML	0.38	8	0.34	4	0.29	8.0
4ML	0.30	8	0.46	4	0.21	7
5ML	0.49	9	0.49	9	0.02	8
8ML	0.34	8	0.65	8		
bulk			1.01	9		

E'. $\mathrm{DHO}_{E'}(E)$ has a shape similar to the Lorentzian function but being zero at zero energy. States at high energies are more effected by the phonon dumping. The following model was used to reproduce the experimental NIS data:

$$S_n(E) = A_{fcc}(S_n^{fcc}(E) * DHO(Q_{fcc})) + A_{bcc}(S_n^{bcc}(E) * DHO(Q_{bcc}))+ A_{EuO}(S_n^{EuO}(E) * DHO(Q_{EuO})). \quad (5.10)$$

The *ab initio* calculated NIS spectra of each site $S_n^m(E)$ is convoluted ($*$) with the $DHO(Q_m)$ characterized with a certain quality factor Q_m. A_m denotes the partial contributions of the sites m *fcc* Eu, *bcc* Eu or EuO. Fig. 5.25 shows the experimental NIS data normalized according to Eqn.(5.8) with the subtracted central part (zero phonon contribution) (open circles) and the resulting fit by Eqn.(5.10) to the spectra (red line). The partial NIS spectra of the sites *fcc* Eu (blue area), *bcc* Eu (light gray area) and EuO (green area) are depicted additionally. The fit does not reproduce the central part perfectly due to artifacts arising from the subtraction of the elastic peak. To minimize the error that is induced by the subtraction procedure on the results, the fits were performed in the range between 3 and 25 meV. Fig. 5.25 reveals a remarkable agreement between the experimental data and the applied model. The values of the fit parameters (partial contributions A_m and quality factors Q) derived from the fits are summarized in Table.5.5. While the quality factor of *fcc* Eu and EuO is almost constant as a function of the Eu coverage, the quality factor of the *bcc* phase is low at a coverage of 2 and 4 ML indicating a low crystalline quality of this phase. With increasing Eu coverage the quality factor is increasing because of the formation of large *bcc* Eu paches, covering the *fcc* islands. The constant quality factor of the *fcc* indicates, that the crystalline quality is not changing with increasing island size as well as after covering them by the *bcc* phase. The constant and rather high value of the quality factor of EuO indicates that independent on the lateral island size and the interface thickness of only 1-2 ML the lattice vibrations of this phase are bulk like.
Based on these results the partial contributions and the total phonon DOS of the *fcc* Eu islands are calculated and presented in Fig. 5.26. The partial contribution of *fcc* Eu (blue area), *bcc* Eu (light gray area) EuO (green area) are depicted additionally. The results from the analysis (Table 5.5) are in agreement with the results from the AFM study of the size evolution of the *fcc* Eu islands. With increasing Eu coverage the contribution of *fcc* Eu is rising. This trend appears due to the increase of the

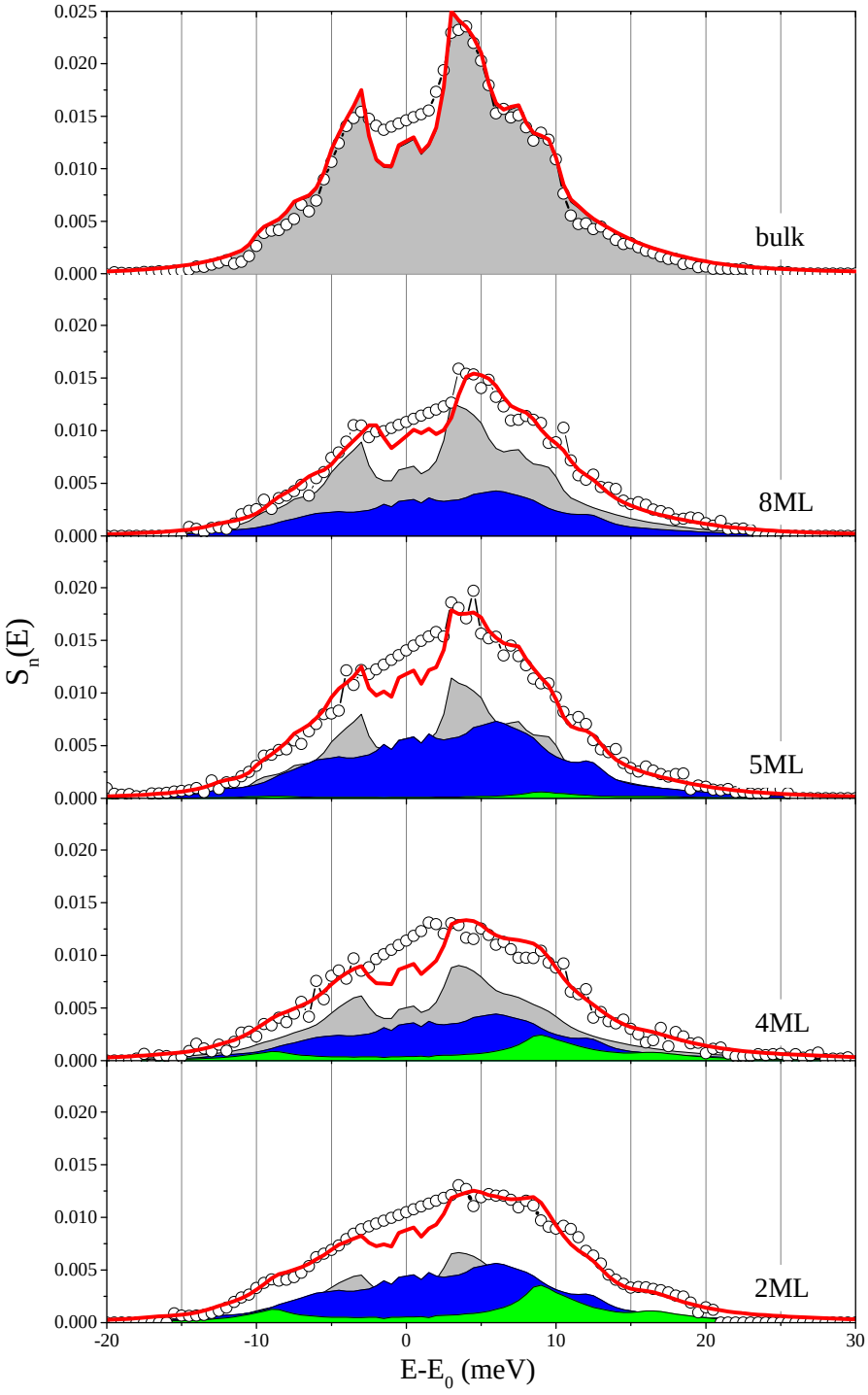

Figure 5.25.: Comparison of the experimental NIS spectra $S_n(E)$ $n \geq 1$ (open circles) and fits (red line), performed applying Eqn.(5.10) with the partial contributions of *fcc* Eu (blue area), *bcc* Eu (light gray area) and EuO (green area). The values of the fit parameters are summarized in Table 5.5.

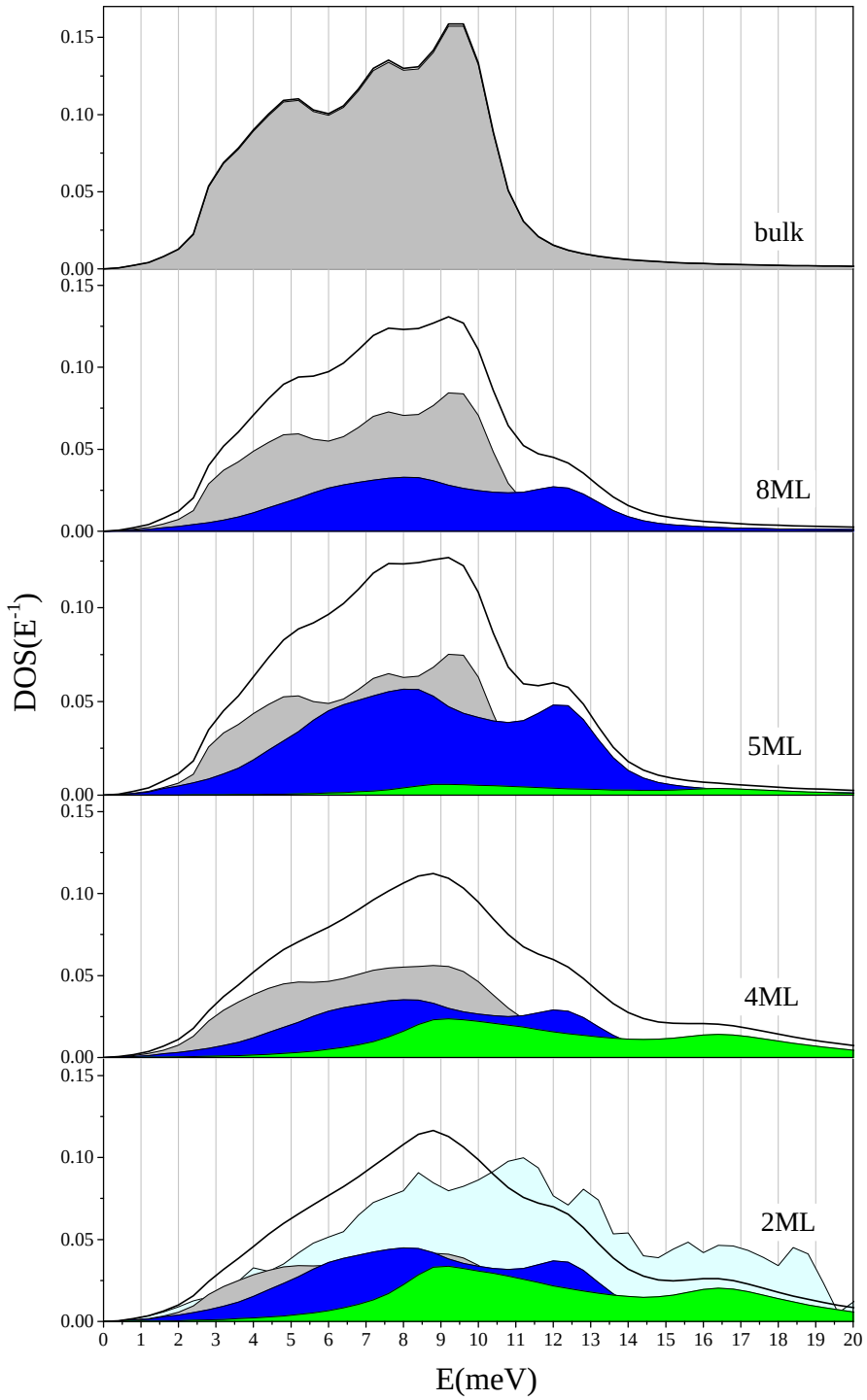

Figure 5.26.: Phonon DOS (black line) recalculated using the fit parameters listed in Table 5.5 for the indicated Eu coverages. The partial contributions of *bcc* Eu (light gray area), *fcc* Eu (blue area) and EuO (green area) are convoluted with the DHO containing the quality factor Q_m and are weighted with the coefficient A_m from Table 5.5. The phonon DOS of the sample with the Eu coverage of 2 ML derived directly from the experimental NIS is shown with light blue area.

island size, which as well explains the highest contribution of EuO in the spectrum of 2 ML Eu coverage. Reaching a critical size at an Eu coverage of 5 ML *fcc* Eu growth does not continue. With higher coverages the growth of polycrystalline *bcc* Eu is burying the islands. It is remarkable that the parasitic growth of *bcc* Eu is already present at a coverage of 2 ML.
Fig. 5.26 shows a comparison of the DOS for 2 ML Eu coverage (light blue area) derived directly from the experimental NIS spectrum and the phonon DOS obtained taking the different partial contribution into account (black line). The remarkable difference between the spectra demonstrates that large errors can be obtained if the presence of various chemical sites of the Mössbauer atom with different f_{LM} values are not taken into account.

5.3.4. Thermodynamic and elastic properties of *fcc* Eu islands

The possibility to qualitatively and quantitatively disentangle various contributions to the NIS spectra of the investigated samples offer a unique opportunity to study the evolution of the thermoelastic properties of the different constituents.
Elastic (force constant, f_{LM}) and thermodynamic (lattice specific heat, vibrational entropy, mean internal energy) properties are summarized in Fig. 5.27. For all coverages and for every Eu phase separately the thermodynamic properties were obtained from the corresponding *ab initio* calculated phonon DOS convoluted with the DHO using the quality factor derived from the fit of the NIS spectra (Table 5.5). The values for *bcc* Eu (gray squares), *fcc* Eu (blue triangles) and EuO (green circles) are shown with symbols. The values of the *ab initio* calculated phonon DOS of *bcc* Eu (black), *fcc* Eu(blue) and EuO (green) are shown with vertical broken lines. The thermodynamic properties of *fcc* Eu and EuO are similar to the bulk properties for all coverages. The largest deviation is visible for *bcc* Eu in samples 2 and 4 ML exhibiting values close to the corresponding values of the *fcc* Eu phase. Another remarkable result from this study is that the thermodynamic properties of the 1-2 ML thick EuO interface remain close to that of the bulk.

5.3.5. Conclusions

The lattice dynamics of the Eu islands with *fcc* symmetry was determined for various Eu coverages by *in situ* nuclear inelastic scattering and by first-principle calculations. A significant reduction of the phonon modes at low energy and an enchantment of the phonon states at high energy is clearly detected by reducing the Eu coverages. This effect is most pronounced for the 2 ML Eu coverage. The observed phenomenon is explained by the contributions of Eu atoms belonging to sites with various crystallographic symmetry (*bcc* and *fcc*) and chemical state (metallic and oxide) to the experimental NIS spectra. These results are qualitatively and quantitatively understood by analysis of the experimental NIS data with a linear combination of weighted contributions from the *ab initio* calculated NIS spectra of the EuO interface, *fcc* interior of the islands and the *bcc* Eu phase, convoluted with the *DHO* function. This approach allowed for an independent determination of the thermo-elastic properties

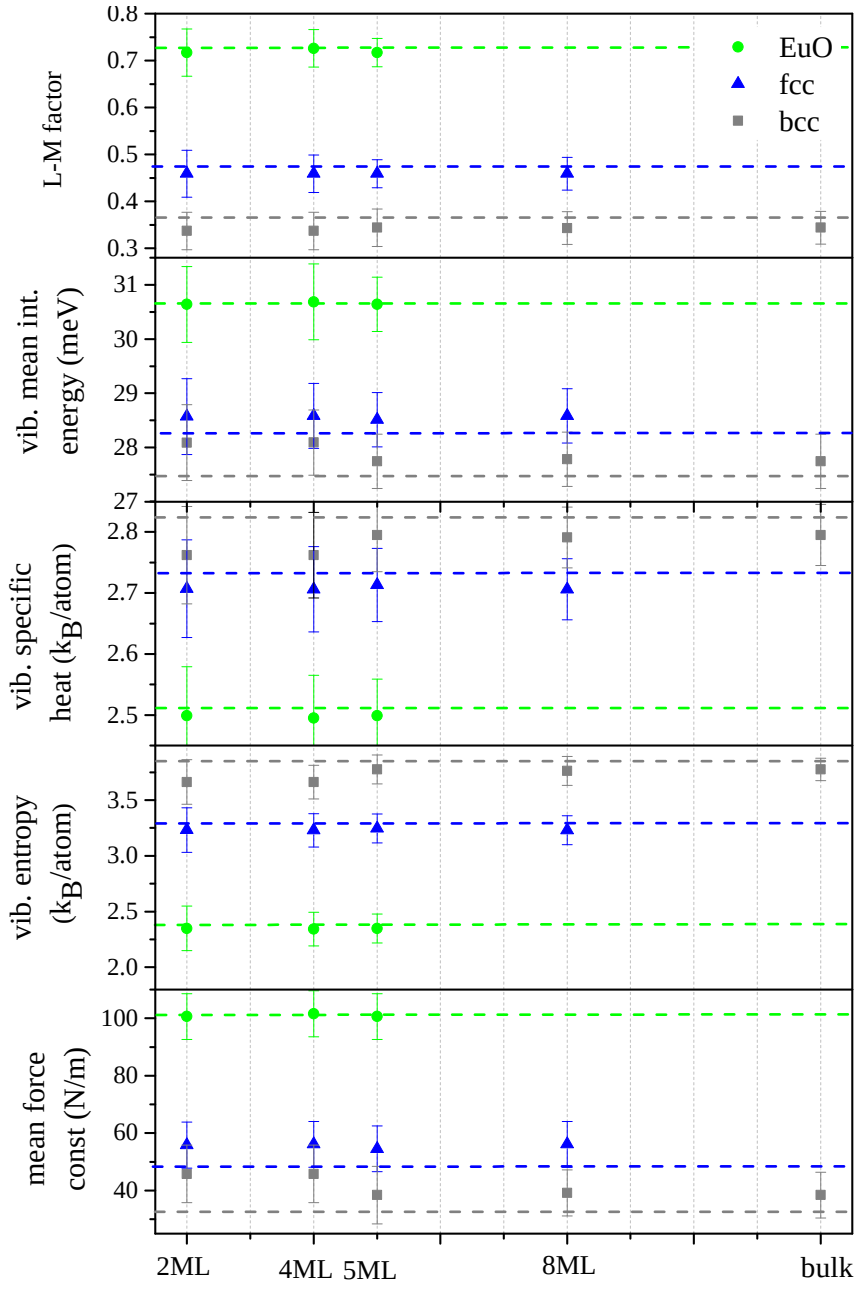

Figure 5.27.: Thermo-elastic properties calculated from the phonon DOS of *fcc* Eu (blue triangle), *bcc* Eu (gray squares) and EuO (green circles) sites, convoluted with the DHO function with the quality factor derived from the fit of the NIS spectra (Table 5.5). Horizontal lines correspond to the thermodynamic properties calculated from the *ab initio* calculated phonon DOS at 100 K.

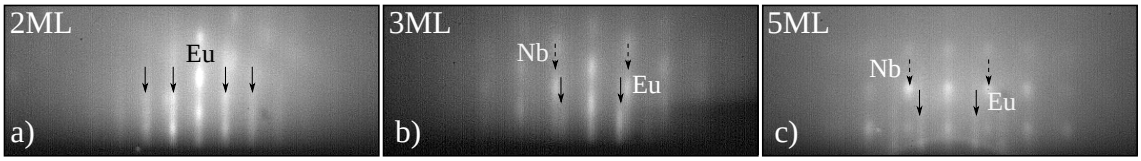

Figure 5.28.: RHEED images along the azimuthal direction [11$\bar{2}$0] for samples with the Eu coverage of 2 and 3 ML and along [$\bar{2}$110] for 5 ML. Streaks and spots belonging to Eu and Nb are indicated with full and dashed arrows, respectively.

of the different constituents of the *fcc* Eu nanoislands. One of the remarkable results from this study is the fact that the lattice dynamics and the thermo-elastic properties of the EuO interface having a thickness between 1 and 2 atomic layers ($3-6\,\mathring{A}$) remain bulk-like. It is demonstrated that the phonon DOS directly derived from the experimentally measured NIS spectrum of a sample containing various chemical states of the Mössbauer-active element leads to a wrong result. A separation of the partial phonon DOS in this case is only possible by using the results from the *ab initio* calculated lattice dynamics of the individual constituents.

5.4. Lattice dynamics of wire-like Eu nanostructures

The formation of a stepped (110) Nb buffer layer on the A-plane Al_2O_3 has been demonstrated in section 5.2.1. Eu, deposited on this surface at a substrate temperature of $T_S = 423\,K$, adopts the surface morphology forming wire-like structures (section 5.2.5). The influence of this surface morphology on the lattice dynamics is discussed in the following.

5.4.1. NIS experiment

Samples with an Eu coverage of 2, 3 and 5 ML (1 ML = $3.25\mathring{A}$) were grown in the UHV system at ID 18 of the ESRF and investigated by RHEED prior to the NIS experiment. Fig. 5.28 shows the RHEED images obtained along the directions [11$\bar{2}$0] for 2 and 3 ML and [2$\bar{1}\bar{1}$0] for 5 ML. In the image of 2 ML coverage vertical streaks are visible, indicating a 2D growth with an epitaxial relationship of Eu to the stepped Nb structure (Fig. 5.28a)). The streaks are less pronounced for the coverage of 3 ML. Spots from the Nb buffer layer are visible for 5 ML coverage (Fig. 5.28 b, c))). Streaks and spots belonging to Eu and Nb are indicated with full and broken arrows, respectively (Fig. 5.28). The lattice constant of $a_h = 4.1 \pm 0.1\,\mathring{A}$ was determined for Eu from the horizontal spacing between the streaks in the RHEED images. The results from this RHEED study are in agreement with the study reported in section 5.2.5 on samples grown in the UHV-analysis Laboratory.

The *in situ* NIS experiment was performed keeping the samples at $T_S = 111\,K$, in order to reduce multiphonon excitations. The simultaneous measurement of NFS

signal was not possible due to the low signal level at the detector. The roughness of the surface leads to a large fraction of diffuse scattering and therefore to a dumping of the reflected intensity in forward direction [36]. The NFS investigations of Eu grown on the reconstructed Nb surface at the growth temperature of $T_S = 423\,\mathrm{K}$ or lower (section 5.2.7), excluded the formation of EuO or higher oxides on the surface (Fig.5.21).
The NIS experiment was performed with the wave vector of the photons parallel to the directions:

$$\vec{k}_0 \,||\, [11\bar{2}0]\mathrm{Eu} \,||\, [001]\mathrm{Nb} \qquad \text{and} \qquad \vec{k}_0 \,||\, [1\bar{1}00]\mathrm{Eu} \,||\, [1\bar{1}0]\mathrm{Nb}$$

5.4.2. Phonon DOS

In the case of a chemically and structurally homogenous sample the phonon DOS can be extracted from the experimental NIS by the procedure described in section 2.3.2 that is implemented in the program DOS [157]. The derived phonon spectra are shown for the measured azimuthal directions $[11\bar{2}0]$ and $[1\bar{1}00]$ in Fig. 5.29 a) and b), respectively.

Fig. 5.29 reveals a systematic shift of the phonon DOS to higher energies and a broadening of the peaks in comparison to that of the *bcc* Eu phonon DOS for all samples and directions. The sample with the coverage of 2 ML exhibits a high energy peak at 16 meV in $[11\bar{2}0]$ direction. This peak is shifted to lower energies, to 14 meV for the $[1\bar{1}00]$ direction. The main peak in $[11\bar{2}0]$ direction is broad and centered around 10 meV. A sharp peak at 8 meV appears in direction $[1\bar{1}00]$. This features are less pronounced for the sample with 3 ML Eu coverage, were a shift to lower energies and broad peaks at 7 meV, 10 meV and 13 meV in the $[11\bar{2}0]$ direction are visible. The phonon DOS exhibits a pronounced vibrational anisotropy for 2 ML and 3 ML Eu coverage that is lifted for the coverage of 5 ML. The phonon spectra of this sample are characterized by two broad peaks at 7 and 10 meV and a high energy tail.
The vanishing of the vibrational anisotropy can be explained by the evolution of the surface morphology with an increase of the Eu coverage, shown in the AFM images in Fig. 5.14. At an Eu coverage of 2 ML, the Nb buffer layer is covered epitaxially. Eu is adopting the morphology of the stepped (110) Nb surface, following the NW orientation relationship of Eu to Nb. Most likely the high aspect ratio of the formed wire-like Eu structure is the reason for the vibrational anisotropy found in this sample. With increasing coverage the surface is changing towards a 3D island-like morphology. This results in the isotropic phonon DOS along both orientations for the coverage of 5 ML (Fig. 5.29).
A common feature of the measured phonon spectra is their shift to higher energy with respect to that of the *bcc* Eu. This behavior is in contradiction to the increased nearest neighbor distance found for the hexagonal structure $a_h = 4.10 \pm 0.1\,\mathring{A}$ of Eu in these samples in comparison to *bcc* Eu with the nearest neighbor distance of $a_{bcc} = 3.97\,\mathring{A}$. However, calculations predicted the formation of *fcc* Eu for an

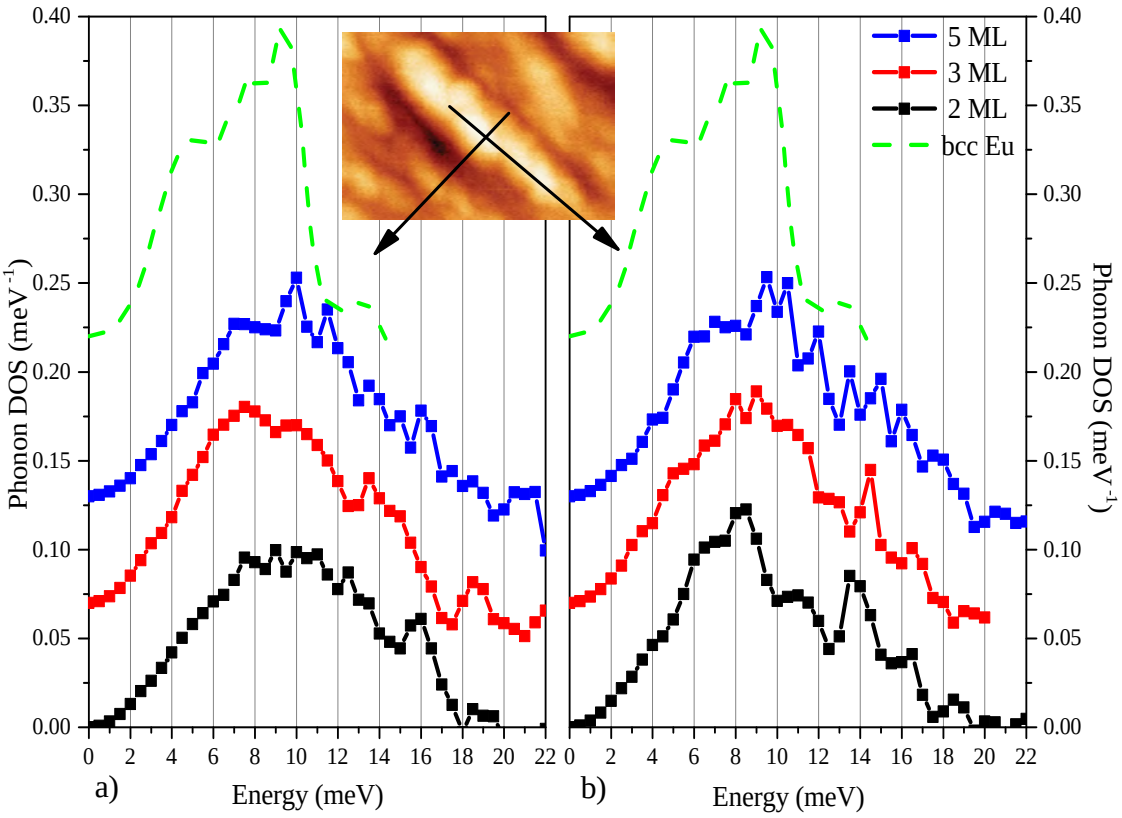

Figure 5.29.: Phonon DOS extracted from the experimental NIS data measured at 100 K, for the samples with the coverage of 2, 3 and 5 ML Eu measured with the wave vector $\vec{k}_0$ along the azimuthal directions a) $[11\bar{2}0]$ and b) $[1\bar{1}00]$. The phonon DOS of *bcc* Eu is added as dashed green line for a comparison. The spectra a shifted up by a constant factor for clarity. An AFM image of the sample with the coverage of 3 ML is shown as inset. The measured directions are indicated with arrows.

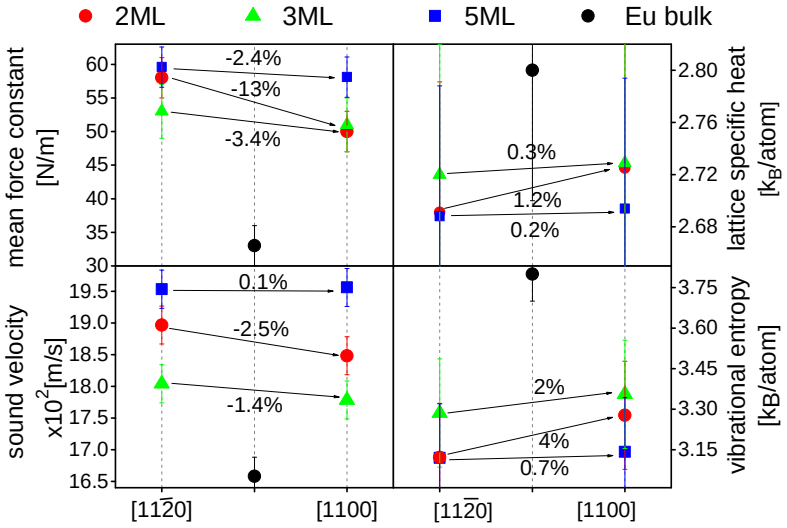

Figure 5.30.: Elastic (sound velocity, force constant) and thermodynamic (lattice specific heat, vibrational entropy) properties for the 2 (red circle), 3 (green triangle) and 5 ML (blue square) Eu covered samples in the directions [11$\bar{2}$0] and [1$\bar{1}$00]. The relative difference between these values is shown. The corresponding values of *bcc* Eu (black circles) (values taken from [17]) are also shown.

increased nearest neighbor distance [158]. In this state Eu is expected to be a semimetal. Semimetals exhibit larger inter-atomic forces, that would imply a shift of the phonon modes to higher energies. The semimetalic state would explain the observed shift of the phonon DOS to higher energies, instead of a shift to lower energies due to an increased nearest-neighbor distance. Since the final phonon energies will be determined by the interplay between lattice compression/expansion and electronic states this hypothesis has to be verified by *ab initio* calculations, which are in progress [159].

5.4.3. Thermodynamic and elastic properties of wire-like Eu nanostructures

The direction projected thermoelastic properties were calculated from the experimentally obtained phonon DOS (Fig. 5.29). Fig. 5.30 shows a comparison of the elastic (sound velocity, force constant) and thermodynamic (lattice specific heat, vibrational entropy) properties projected on the [11$\bar{2}$0] and [1$\bar{1}$00] directions. The values of the 2 ML coverage are shown as red circles, 3 ML with green triangles and 5 ML with blue squares. The value for bulk *bcc* Eu is plotted with black circles for comparison. Sound velocities and mean force constants are increased for all samples while the lattice specific heat and the vibrational entropy are reduced in comparison to the *bcc* Eu values. The behavior of the thermodynamic properties results from the shift of the phonon DOS to higher energies for all samples. For the sample with a coverage of 2 ML the difference between the [11$\bar{2}$0] and [1$\bar{1}$00] directions is clearly visible and is the most pronounced. The force constant and

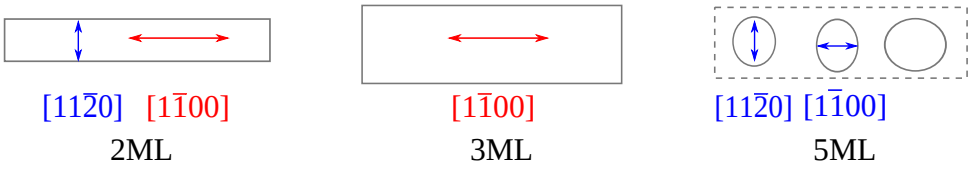

Figure 5.31.: Sketch of the Eu nanostructure formed at an Eu coverage of 2, 3 and 5 ML. In direction [11$\bar{2}$0] the numbers of the thermodynamic properties for 2ML are similar to the numbers of 5ML coverage (blue arrows), while in [1$\bar{1}$00] direction the thermodynamical properties are similar to 3ML coverage in the same direction (red arrows).

the sound velocity are reduced by 13% and 2.5% along [1$\bar{1}$00] in comparison to the [11$\bar{2}$0] direction. Lattice specific heat and vibrational entropy are increased by 1.2% and 4% (Fig. 5.30). The values of the force constant and the sound velocity for 3 ML coverage are reduced by 3.4% and 1.4%, while those of the lattice specific heat and vibrational entropy are increased by 0.3% and 2% (Fig. 5.30). As expected from the phonon DOS the values for 5 ML are almost identical. The values for the 2 ML covered sample in the [11$\bar{2}$0] direction are similar to the values of 5 ML coverage, while in [1$\bar{1}$00] direction the values are similar to that of 3 ML coverage. The evolution of the thermodynamic properties as a function of the Eu coverage can be explained by the changes of the surface morphology obtained from the AFM images in Fig. 5.14 and in Table 5.1. At a coverage of 2 ML Eu grows epitaxially on the long steps formed by the Nb buffer layer, resulting in the formation of a wire-like structures. At a coverage of 3 ML the steps are wider. Due to the epitaxial strain initiated by the lattice missmach this surface morphology cannot persist for higher coverages leading to the formation of islands at 5 ML Eu coverage. Fig. 5.31 shows schematically the evolution of the wire-like structure to an island-like stage at various Eu coverages. The arrows in Fig. 5.31 show the directions of the measurements in [11$\bar{2}$0] and [1$\bar{1}$00], perpendicular and parallel to the steps, respectively. The values of the thermodynamical properties in [11$\bar{2}$0] direction (perpendicular to the steps) for 2 ML coincide with the values for 5 ML, indicated with the blue arrow. In direction [1$\bar{1}$00] (along the steps) the numbers for 2 ML coverage are similar to the values of 3 ML, indicated with red arrow.

5.4.4. Conclusions

The lattice dynamics of high aspect ratio, wire-like Eu nanostructures with Eu coverages of 2, 3, and 5 ML deposited on the oxygen-free stepped (110) Nb surface was investigated by *in situ* nuclear inelastic scattering. A general feature of the phonon DOS obtained from the NIS spectra is a shift to higher energy in comparison to that of the native for Eu *bcc* lattice. In addition, the phonon DOS of the samples with Eu coverage of 2 and 3 ML obtained along the nanowire-like structures differs from those obtained across the wires, revealing the presence of a remarkable vibrational anisotropy. The effect is most pronounced for 2 ML coverage, while at 5 ML the

phonon spectrum is already isotropic. The calculated thermodynamic and elastic properties of the Eu nanostructures from the phonon DOS demonstrate the hardening of the crystal lattice of Eu with respect to the native *bcc* lattice. Although being isotropic, the values of the sample with 5 ML Eu coverage remain dissimilar from those of the *bcc* Eu. The evolution of the thermo-elastic properties is explained by the changes of the surface morphology from a wire-like to a 3D island-like surface by increasing the Eu coverage. A possible explanation of the observed effect in the phonon spectra is a semi metallic nature of the nanostructures. This, however, has to be further investigated and verified by *ab initio* calculations.

6. Summary and Conclusions

The number of technological applications of rare earth metals and their compounds is continuously increasing spanning fields like medicine, energy, nanoelectronics and automobile industry. The efficient use of these materials as well as the design of new lanthanide-based compounds with superior characteristics requires the comprehensive understanding of their elemental physical properties. The lattice dynamics of these materials defines the thermodynamic and elastic properties and is therefore of fundamental importance for the characterization of materials.
Additionally to the exploration of bulk-like rare earth elements, this thesis is tackling the challenge of the investigation of the lattice dynamics of lantanide samples with dimensions on the nano- and subnanometer length scale.

The aim of this thesis was the determination of the lattice dynamics and the thermoelastic properties of bulk-like single-crystalline Sm and Nd films and of Eu-based epitaxial nanostructures by *in situ* nuclear inelastic scattering, inelastic X-ray scattering, and *first-principles* phonon calculations (performed by a collaboration partner). The obtained results can be summarized as follows:

1. A bulk-like single crystalline Sm film with the *Sm type* structure, which is native for this metal, was grown and characterized by X-ray diffraction and low-temperature nuclear forward scattering. The phonon DOS was measured and compared with the results from the *ab initio* phonon calculations. While the low energy part of the phonon DOS coincide, a splitting and a broadening of the high energy peak was observed, which is not found in the calculations.

2. A growth procedure for achieving bulk-like Sm films with the *dhcp* lattice (characteristic for light lanthanides) was elaborated. Phonon dispersion relations were measured on a 500 nm thick *dhcp* Sm film and the results were compared with the results from *ab inito* calculations revealing a shift to higher energies in one branch. All other measured phonon branches coincide with the calculations.

3. A bulk-like single crystalline Nd film with its native *dhcp* lattice was grown and characterized by X-ray and electron diffraction methods. The phonon dispersion relations were measured and compared with results from the *ab initio* theory. The experimental points follow the trend of the calculated phonon branches, however, with a systematic shift to higher energies. This shift is particularly pronounced in the (0001) Nd direction.

4. Eu nano-islands with *fcc* symmetry, which is unusual for this metal, were grown on (110)Nb surfaces with an oxygen induced surface reconstruction.

The growth mechanism was elucidated and the formation of EuO at the Eu/Nb interface at 533 K was unambiguously proven. It was found that at a growth temperature of 423 K, EuO is not formed leading to a relaxation of the Eu deposit to a film with hexagonal symmetry.

5. The lattice dynamics of *fcc* Eu nanoislands was determined for various Eu coverages by *in situ* nuclear inelastic scattering and by *ab initio* calculations. In islands with reduced island sizes a pronounced and systematic shift of the phonon spectrum to higher energies was observed. This abnormal behavior is explained both qualitatively and quantitatively by the co-existence of a metallic Eu phase (*fcc* and *bcc*) and an EuO interface. The partial phonon spectra of the constituents were reliably disentangled. The thermodynamic and elastic properties of the *fcc* Eu nanoislands were determined. Remarkably, the properties of the ultra-thin EuO interface remain very close to that of the bulk.

6. High aspect ratio wire-like Eu nanostructures were grown on the stepped (110)Nb surface without an oxygen induced surface reconstruction. Their crystal structure and surface morphology was determined. The phonon DOS was measured across and along the main axis of the wires, revealing the presence of a pronounced vibrational anisotropy at an Eu coverage of 2 ML. This anisotropy decreases with increasing Eu coverage and vanishes completely at a coverage of 5 ML. An additional observation is a shift of the phonon DOS to higher energies compared to that of the native *bcc* phase. A possible explanation of this effect based on the semi-metallic nature of these nanostructures is suggested that has to be verified by the on-going calculations.

The experimental and theoretical results described in this thesis shed new light on the lattice dynamics of the bulk rare earth metals. The comparison between experiment and theory clearly demonstrates that although the phonon dispersion relations and the phonon DOS could be reliably predicted by the *ab initio* calculations at low energy, a clear and systematic discrepancy with the experiment is visible for high-energy phonon branches. This effect is particularly strong for phonon branches with polarization vectors parallel to the [0001] crystal direction. Similar results have been reported (unpublished) by other research groups for Gd. These observations call for a systematic theoretical study of the lattice dynamics of the $4f$ elements and a comparison with the available experimental data. Despite the determination of the lattice dynamics of Sm and Nd reported here, the phonon properties of some of the pure rare earth metals remain unknown yet.

The results obtained on the lattice dynamics of the Eu nanostructures can be considered as a step towards phonon engineering on the nanometer length scale. At the first place, the results demonstrate for the first time a successful decomposition of the phonon spectrum in to its constituents (*bcc* Eu metal, *fcc* Eu metal and EuO) by nuclear inelastic scattering. This opens the way for the investigation of the lattice dynamics of hybrid nanostructures with complex character. Secondly, the results on the wire-like Eu structures reveal the presence of anisotropy in the

atomic vibrations related not only to the crystallographic structure but also arising from the anisotropy of the surface morphology. Although these results are still far from practical applications, they demonstrate that a full control over the heat and sound propagation by lattice dynamics engineering can possibly be realized in the future by specially designed nano-assemblies.

Glossary

AFM	atomic force microscopy
bcc	body centered cubic
dhcp	double hexagonal close packed
DHO	damped harmonic oscillator
DOS	density of states
fcc	face centered cubic
hcp	hexagonal close packed
IXS	inelastic X-ray scattering
LEED	low energy electron diffraction
MBE	molecular beam epitxy
ML	mono layer
NIS	nuclear inelastic scattering
NFS	nuclear forward scattering
NRS	nuclear resonant scattering
RE	rare earth
RHEED	reflection high energy electron diffraction
SOC	spin-orbit coupling
SR	synchrotron radiation
TM	transition metals

UHV ultra-high vacuum

XPS X-ray photoelectron spectroscopy

Bibliography

[1] Martin Maldovan. Sound and heat revolutions in phononics. *Nature*, 503:209–217, Nov 2013.

[2] Virender K. [Hrsg.] Sharma, editor. *Mössbauer spectroscopy : Applications in chemistry, biology, and nanotechnology*. Wiley, Hoboken, NJ, 2013.

[3] N.Nücker. *Proceedings of the international conference on lattice dynamics (Paris, September 5-9, 1978)*. Flammarion, Paris, 1978.

[4] C. Stassis, C. K. Loong, and J. Zarestky. Phonon dispersion curves of fcc La. *Phys. Rev. B*, 26:5426–5432, Nov 1982.

[5] C. Stassis, G. S. Smith, B. N. Harmon, K.-M. Ho, and Y. Chen. Lattice dynamics of the metastable fcc phase of lanthanum. *Phys. Rev. B*, 31:6298–6304, May 1985.

[6] F. Güthoff, W. Petry, C. Stassis, A. Heiming, B. Hennion, C. Herzig, and J. Trampenau. Phonon dispersion of bcc La. *Phys. Rev. B*, 47:2563–2572, Feb 1993.

[7] C. Stassis, T. Gould, O. D. McMasters, K. A. Gschneidner, and R. M. Nicklow. Lattice and spin dynamics of γ-Ce. *Phys. Rev. B*, 19:5746–5753, Jun 1979.

[8] C. Stassis, C. K. Loong, C. Theisen, and R. M. Nicklow. Lattice dynamics of fcc Yb. *Phys. Rev. B*, 26:4106–4110, Oct 1982.

[9] J. C. Glyden Houmann and R. M. Nicklow. Lattice dynamics of terbium. *Phys. Rev. B*, 1:3943–3952, May 1970.

[10] R. M. Nicklow, N. Wakabayashi, and P. R. Vijayaraghavan. Lattice dynamics of holmium. *Phys. Rev. B*, 3:1229–1234, Feb 1971.

[11] X.-W. Wang, Y. Chen, C. Stassis, B.N. Harmon, K.-M. Ho, and W. Weber. Anomalous low-temperature lattice dynamics of fcc lanthanum. *Physica B+C*, 135(1–3):477 – 481, 1985.

[12] R. Ramji Rao and C.S. Menon. Lattice dynamics, third order elastic constants and thermal expansion of gadolinium. *Journal of Physics and Chemistry of Solids*, 35(3):425–432, 1974.

[13] R. Ramji Rao and C.S. Menon. Dispersion relations and lattice thermal expansion of dysprosium. *Journal of Physics and Chemistry of Solids*, 34(11):1879–1886, 1973.

[14] R. R. Rao and A. Ramanand. Lattice dynamics, thermal expansion and bulk modulus of erbium. *Acta Crystallographica Section A*, 33(1):146–150, 1977.

[15] J. C. Upadhyaya and A. O. E. Animalu. Microscopic theory of the lattice dynamics of hcp rare-earth metals. *Phys. Rev. B*, 15:1867–1876, Feb 1977.

[16] Yifang Ouyang, Xiaoma Tao, Fanjiang Zeng, Hongmei Chen, Yong Du, Yuanping Feng, and Yuehui He. First-principles calculations of elastic and thermophysical properties of Al, Mg and rare earth lanthanide elements. *Physica B: Condensed Matter*, 404(16):2299 – 2304, 2009.

[17] Svetoslav Stankov, Przemysław Piekarz, Andrzej M. Oleś, Krzysztof Parlinski, and Rudolf Rüffer. Lattice dynamics of Eu from nuclear inelastic scattering and first-principles calculations. *Phys. Rev. B*, 78:180301, Nov 2008.

[18] S. Soriano, K. Dumesnil, C. Dufour, and D. Pierre. Epitaxial growth of europium on (110) Nb and (0001)Y. *Journal of Crystal Growth*, 265(3–4):582–591, 2004.

[19] C. G. Olson, X. Wu, Z-L. Chen, and D. W. Lynch. New metastable nonmetallic phase of europium. *Phys. Rev. Lett.*, 74:992–995, Feb 1995.

[20] T. Gourieux, S. Fréchard, F. Dulot, J. Eugène, B. Kierren, and D. Malterre. Influence of chemisorbed oxygen on the growth of europium phases on V(110). *Phys. Rev. B*, 62:7502–7509, 2000.

[21] J. Kołaczkiewicz and E. Bauer. The adsorption of Eu, Gd and Tb on the W(110) surface. *Surface Science*, 175(3):487 –507, 1986.

[22] Max Born and Kun Huang. *Dynamical theory of crystal lattices*. The international series of monographs on physics. Clarendon Pr., Oxford [u.a.], 1954.

[23] A. A. Maradudin. Dynamical properties of solids, 1974.

[24] Yi-Long Chen and De-Ping Yang. *Mössbauer Effect in Lattice Dynamics*. WILEY-VCV Verlag, 2007.

[25] B. G. Dick and A. W. Overhauser. Theory of the dielectric constants of alkali halide crystals. *Phys. Rev.*, 112:90–103, Oct 1958.

[26] Y. Fujii, N. A. Lurie, R. Pynn, and G. Shirane. Inelastic neutron scattering from solid ^{36}Ar. *Phys. Rev. B*, 10:3647–3659, Oct 1974.

[27] Werner Weber. Adiabatic bond charge model for the phonons in diamond, Si, Ge, and α-Sn. *Phys. Rev. B*, 15:4789–4803, May 1977.

[28] J. Tersoff. New empirical model for the structural properties of silicon. *Phys. Rev. Lett.*, 56:632–635, Feb 1986.

[29] Gyaneshwar P. Srivastava. *The physics of phonons*. Hilger, Bristol [u.a.], 1990.

[30] William Cochran. *The dynamics of atoms in crystals*. The structures and properties of solids ; 3. Arnold, London, 1st publ. edition, 1973.

[31] Charles Kittel. *Einführung in die Festkörperphysik*. Oldenbourg, München, 14 edition, 2006.

[32] Brent Fultz. Vibrational thermodynamics of materials. *Progress in Materials Science*, 55:247–352, 2010.

[33] Charles Kittel and Herbert Kroemer. *Thermodynamik*. Oldenbourg, MÃ¼nchen, 5., erw. aufl. edition, 2001.

[34] D. Barb. *Grundlagen und Anwendungen der Mössbauerspektroskopie*. Ed. Acad. Republicii Socialiste Romania, Bucuresti, 1980.

[35] Michael Y. Hu, Wolfgang Sturhahn, Thomas S. Toellner, Philip D. Mannheim, Dennis E. Brown, Jiyong Zhao, and E. Ercan Alp. Measuring velocity of sound with nuclear resonant inelastic X-ray scattering. *Phys. Rev. B*, 67:094304, Mar 2003.

[36] Ralf Röhlsberger. *Nuclear Condensed Matter Physics with Synchrotron Radiation*. Springer, Berlin, 2007.

[37] V. G. Kohn, A. I. Chumakov, and R. Rüffer. Nuclear resonant inelastic absorption of synchrotron radiation in an anisotropic single crystal. *Phys. Rev. B*, 58:8437–8444, Oct 1998.

[38] J. C. Slater. Wave functions in a periodic potential. *Phys. Rev.*, 51:846–851, May 1937.

[39] Paul M. Marcus. Variational methods in the computation of energy bands. *International Journal of Quantum Chemistry*, 1(S1):567–588, 1967.

[40] D. R. Hamann, M. Schlüter, and C. Chiang. Norm-conserving pseudopotentials. *Phys. Rev. Lett.*, 43:1494–1497, Nov 1979.

[41] G. Kresse and J. Furthmüller. Efficiency of ab-initio total energy calculations for metals and semiconductors using a plane-wave basis set. *Computational Materials Science*, 6(1):15 – 50, 1996.

[42] P. E. Blöchl. Projector augmented-wave method. *Phys. Rev. B*, 50:17953–17979, Dec 1994.

[43] H. Hellmann. *Einführung in die Quantenchemie*. Franz Deuticke, Leibzig, 1937.

[44] R. P. Feynman. Forces in molecules. *Phys. Rev.*, 56:340–343, Aug 1939.

[45] K. Parlinski. Software PHONON. 2011.

[46] K. Parlinski, Z. Q. Li, and Y. Kawazoe. First-principles determination of the soft mode in cubic ZrO_2. *Phys. Rev. Lett.*, 78:4063–4066, May 1997.

[47] Rudolf L. Mössbauer. Kernresonanzfluoreszenz von Gammastrahlung in Ir^{191}. *Zeitschrift für Physik*, 151(2):124–143, 1958.

[48] Amos de Shalit and Herman Feshbach. *Theoretical nuclear physics*. Wiley, New York, 1974.

[49] I. Sergueev, H.-C. Wille, R. P. Hermann, D. Bessas, Yu. V. Shvyd'ko, M. Zajac, and R. Rüffer. Milli-electronvolt monochromatization of hard X-rays with a sapphire backscattering monochromator. *Journal of Synchrotron Radiation*, 18(5):802–810, Sep 2011.

[50] Wolfgang Sturhahn. Nuclear resonant spectroscopy. *Journal of Physics: Condensed Matter*, 16(5):S497, 2004.

[51] D. A. Shirley. Application and interpretation of isomer shifts. *Rev. Mod. Phys.*, 36:339–351, 1964.

[52] P. Brix, S. Hüfner, P. Kienle, and D. Quitmann. Isomer shift on Eu^{151}. *Physics Letters*, 13(2):140 – 142, 1964.

[53] G.K. Shenoy and B.D. Dunlap. Method for the analysis of pure quadrupole spectra in nuclear gamma-ray resonance. *Nuclea Instruments and Methods*, 71:285–291, 1969.

[54] M.H. Cohen. Nuclear quadrupole spectra in solids. *Physical Review*, 96(5):1278, 1954.

[55] Alfred Q.R. Baron. Detectors for nuclear resonant scattering experiments. *Hyperfine Interactions*, 125(1– 4):29–42, 2000.

[56] E. E. Alp, W Sturhahn, and T. S. Toellner. Lattice dynamics and inelastic nuclear resonant X-ray scattering. *Journal of Physics. Condensed Matter*, 13(34):7645, 2001.

[57] M.A. Andreeva, S.M. Irkaev, and V.G. Semenov. Secondary radiation emission at Mössbauer total external reflection. *Hyperfine Interactions*, 97-98(1):605–623, 1996.

[58] M. A. Andreeva and B. Lindgren. Nuclear resonant spectroscopy at bragg reflections from periodic multilayers: Basic effects and applications. *Phys. Rev. B*, 72:125422, Sep 2005.

[59] Harry J. Lipkin. Mössbauer sum rules for use with synchrotron sources. *Phys. Rev. B*, 52:10073–10079, Oct 1995.

[60] Harry J. Lipkin. Some simple features of the Mössbauer effect. *Annals of Physics*, 9(2):332–339, 1960.

[61] Svetoslav Stankov, Rudolf Rüffer, Marcel Sladecek, Marcus Rennhofer, Bogdan Sepiol, Gero Vogl, Nika Spiridis, Tomasz Slezak, and Jozef Korecki. An ultrahigh vacuum system for in situ studies of thin films and nanostructures by nuclear resonance scattering of synchrotron radiation. *Review of Scientific Instruments*, 79(4):045108, 2008.

[62] S. Stankov, R. Röhlsberger, T. Ślęzak, M. Sladecek, B. Sepiol, G. Vogl, A. I. Chumakov, R. Rüffer, N. Spiridis, J. Łażewski, K. Parliński, and J. Korecki. Phonons in iron: From the bulk to an epitaxial monolayer. *Phys. Rev. Lett.*, 99:185501, Oct 2007.

[63] Rudolf Rüffer and Aleksandr I. Chumakov. Nuclear resonance beamline at ESRF. *Hyperfine Interactions*, 97–98(1):589–604, 1996.

[64] ESRF. http://www.esrf.eu/usersandscience/experiments/dynextrcond/id18, 2014.

[65] Tetsuya Ishikawa, Yoshitaka Yoda, Koichi Izumi, Carlos Kenichi Suzuki, Xiao Wei Zhang, Masami Ando, and Seishi Kikuta. Construction of a precision diffractometer for nuclear bragg scattering at the photon factory. *Review of Scientific Instruments*, 63(1):1015–1018, 1992.

[66] Paul Kirpatrick and A.V. Baez. Formation of optical images by X-rays. *J. Opt. Soc. Am.*, 38(9):766–773, Sep 1948.

[67] Thomas Roth. *Development and Applications of the nuclear lighthouse effect at high energies and at grazing incidence*. PhD thesis, Universität Rostock, 2005.

[68] Michael Krisch and Francesco Sette. *Inelastic X-Ray Scattering from Phonons*, volume 108 of *Topics in Applied Physics*. Springer Berlin Heidelberg, 2007.

[69] E. Burkel. Inelastic X-ray scattering with high energy resolution - a new method for investigations of condensed matter. *Physica B: Condensed Matter*, 180–181:840–842, 1992.

[70] ESRF. http://www.esrf.eu/usersandscience/experiments/dynextrcond/id28, 2014.

[71] A Snigirev, V. Kohn, I. Snigireva, and B. Lengeler. A compound refractive lens for focusing high-energy X-rays. *Nature*, 384:49–51, 1996.

[72] John R. Arthur. Molecular beam epitaxy. *Surface Science*, 500(1–3):189–217, 2002.

[73] Marian A. Herman and Helmut Sitter. *Molecular beam epitaxy : Fundamentals and current status*. Springer series in materials science ; 7. Springer, Berlin [u.a.], 2., rev. and upd. ed. edition, 1996.

[74] Werner Kern John L. Vossen. *Thin film processes*, volume 2. Academic Press Inc, New York, 1991.

[75] S. D. Barrett. *The structure of rare-earth metal surfaces*. Imperial College Press, London, 2001.

[76] C.E.C. Wood. Physics of thin films. *Physics of thin films*, 11:39, 1980.

[77] J. Lewis, D. Schwarzenbach, and H. D. Flack. Electric field gradients and charge density in corundum, α-Al_2O_3. *Acta Crystallographica Section A*, 38(5):733–739, 1982.

[78] J. Kwo, M. Hong, and S. Nakahara. Growth of rare-earth single crystals by molecular beam epitaxy: The epitaxial relationship between hcp rare earth and bcc niobium. *Applied Physics Letters*, 49(6):319–321, 1986.

[79] A. Stenborg, J. N. Andersen, O. Björneholm, A. Nilsson, and N. Mårtensson. Valence-transition-induced 5×5 surface reconstruction of Sm(0001). *Phys. Rev. Lett.*, 63:187–190, Jul 1989.

[80] A.R. Wildes, J. Mayer, and K. Theis-Bröhl. The growth and structure of epitaxial niobium on sapphire. *Thin Solid Films*, 401(1–2):7–34, 2001.

[81] Max Hansen and Kurt Anderko. *Constitution of binary alloys*. McGraw-Hill, New York, 1958.

[82] C. Dufour, K. Dumesnil, S. Soriano, D. Pierre, Ch. Senet, and Ph. Mangin. Epitaxial growth of dhcp samarium: single crystal films and Sm/Nd superlattices. *Journal of Crystal Growth*, 234(2–3):447 – 453, 2002.

[83] C. Dufour, K. Dumesnil, S. Soriano, Ph. Mangin, P. J. Brown, A. Stunault, and N. Bernhoeft. Magnetic structures in a dhcp samarium film. *Phys. Rev. B*, 66:094428, Sep 2002.

[84] V. Oderno, C. Dufour, K. Dumesnil, A. Mougin, Ph. Mangin, and G. Marchal. Hexagonal surface structure during the first stages of niobium growth on sapphire $(11\bar{2}0)$. *Philosophical Magazine Letters*, 78(5):419–426, 1998.

[85] G. L. Zhou and C. P. Flynn. Fingered morphology of niobium (110) grown by molecular-beam epitaxy. *Phys. Rev. B*, 59:7860–7867, 1999.

[86] S. W. Bonham and C. P. Flynn. Control of heteroepitaxial stacking by substrate miscut. *Phys. Rev. B*, 58:10875–10882, 1998.

[87] C. Sürgers and H. Löhneysen. Effect of oxygen segregation on the surface structure of single-crystalline niobium films on sapphire. *Applied Physics A*, 54(4):350–354, 1992.

[88] D.L. Adams and H.B. Nielsen. The preparation and surface structure of clean V(110). *Surface Science*, 107(1):305–320, 1981.

[89] Christoph Sürgers, Maya Schöck, and Hilbert v. Löhneysen. Oxygen-induced surface structure of NbO. *Surface Science*, 471(1–3):209–218, 2001.

[90] H. Li, D. Tian, J. Quinn, Y. S. Li, S. C. Wu, and F. Jona. Structural and electronic properties of ultrathin films of Gd, Tb, Dy, Ho, and Er. *Phys. Rev. B*, 45:3853–3856, Feb 1992.

[91] E. Vescovo and C. Carbone. Oxidation of epitaxial Ce films. *Phys. Rev. B*, 53:4142–4147, Feb 1996.

[92] A. Stenborg, J. N. Andersen, O. Björneholm, A. Nilsson, and N. Mårtensson. Valence-transition-induced 5×5 surface reconstruction of Sm(0001). *Phys. Rev. Lett.*, 63:187–190, Jul 1989.

[93] K.Y. Yang, Hitoshi Homma, and Ivan K. Schuller. Epitaxial film growth and metastable phases of single crystal Dy by molecular beam epitaxy. *Journal of Applied Physics*, 63(8):4066–4068, 1988.

[94] B. Kierren, T. Gourieux, F. Bertran, and G. Krill. Epitaxy of Ce and Ce oxides on V(110). *Phys. Rev. B*, 49:1976–1980, Jan 1994.

[95] L. A. Bruce and H. Jaeger. Geometric factors in f.c.c. and b.c.c. metal-on-metal epitaxy III. the alignments of (111) f.c.c.-(110) b.c.c. epitaxed metal pairs. *Philosophical Magazine A*, 38(2):223–240, 1978.

[96] NT-MDT. http://www.ntmdt.com/, 2014.

[97] Zhong Lin Wang. *Reflection Electron Microscopy and Spectroscopy for Surface Analysis*. Cambridge University Press, 1996.

[98] J. M. Van Hove, C. S. Lent, P. R. Pukite, and P. I. Cohen. Damped oscillations in reflection high energy electron diffraction during GaAs MBE. *Journal of Vacuum Science & Technology B: Microelectronics and Nanometer Structures*, 1(3):741–746, 1983.

[99] David [Hrsg.] Briggs, editor. *Practical surface analysis*, volume Auger and X-ray photoelectron spectroscopy. Wiley, Chichester, 2 edition, 1990.

[100] J.J. Yeh and I. Lindau. Atomic subshell photoionization cross sections and asymmetry parameters: $1 \ll Z \ll 103$. *Atomic Data and Nuclear Data Tables*, 32(1):1–155, 1985.

[101] M. P. Seah and W. A. Dench. Quantitative electron spectroscopy of surfaces: A standard data base for electron inelastic mean free paths in solids. *Surface and Interface Analysis*, 1(1):2–11, 1979.

[102] A. W. Overhauser. Crystal structure of lithium at 4.2 K. *Phys. Rev. Lett.*, 53:64–65, Jul 1984.

[103] R. Berliner, O. Fajen, H. G. Smith, and R. L. Hitterman. Neutron powder-diffraction studies of lithium, sodium, and potassium metal. *Phys. Rev. B*, 40:12086–12097, Dec 1989.

[104] F. H. Ellinger and W. H. Zachariasen. The crystal structure of samarium metal and of samarium monoxide. *Journal of the American Chemical Society*, 75(22):5650–5652, 1953.

[105] A. H. Daane, D. H. Dennison, and F. H. Spedding. The preparation of samarium and ytterbium metals. *Journal of the American Chemical Society*, 75(9):2272–2273, 1953.

[106] W. C. Koehler and R. M. Moon. Magnetic structures of samarium. *Phys. Rev. Lett.*, 29:1468–1472, Nov 1972.

[107] R. M. Moon and W. C. Koehler. Magnetic scattering amplitudes of samarium. *AIP Conference Proceedings*, 10(1):1314–1318, 1973.

[108] A. Barla, J.-P. Sanchez, J. Derr, B. Salce, G. Lapertot, J. Flouquet, B. P. Doyle, O. Leupold, R. Rüffer, M. M. Abd-Elmeguid, and R. Lengsdorf. Valence and magnetic instabilities in Sm compounds at high pressures. *Journal of Physics: Condensed Matter*, 17(11):S837, 2005.

[109] K. Dumesnil, C. Dufour, Ph. Mangin, M. Hennion, and P. J. Brown. Crystal and magnetic structures of sm epitaxial thin films and Sm/Y superlattices. *Phys. Rev. B*, 60:10743–10746, Oct 1999.

[110] A. Barla, J. P. Sanchez, Y. Haga, G. Lapertot, B. P. Doyle, O. Leupold, R. Rüffer, M. M. Abd-Elmeguid, R. Lengsdorf, and J. Flouquet. Pressure-induced magnetic order in golden SmS. *Phys. Rev. Lett.*, 92:066401, Feb 2004.

[111] O. Bauder, P. Piekarz, A. Barla, I. Sergueev, R. Rüffer, J. Łażewski, T. Baumbach, K. Parlinski, and S. Stankov. Lattice dynamics of the rare-earth element samarium. *Phys. Rev. B*, 88:224303, Dec 2013.

[112] Albert C. Thompson and Douglas Vaughan, editors. *X-ray Data Booklet*. Lawrence Berkeley National Laboratory's, 2011.

[113] Gunther K. Wertheim. *Mössbauer Effect: Principles and Applications*. Academic Press, 1964.

[114] S. Ofer and I. Nowik. Magnetic and quadrupole moments of the 22 keV state of ^{149}Sm. *Nuclear Physics A*, 93(3):689 – 691, 1967.

[115] Robert J. [Hrsg.] Elliott, editor. *Magnetic properties of rare earth metals*. Plenum Pr., London, 1972.

[116] A. I. Chumakov, R. Rüffer, O. Leupold, A. Barla, H. Thiess, J. M. Gil, H. V. Alberto, R. C. Vilão, N. Ayres de Campos, V. G. Kohn, M. Gerken, and M. Lucht. Nuclear inelastic scattering with ^{161}Dy. *Phys. Rev. B*, 63:172301, Apr 2001.

[117] J. K. Alstad, R. V. Colvin, S. Legvold, and F. H. Spedding. Electrical resistivity of lanthanum, praseodymium, neodymium, and samarium. *Phys. Rev.*, 121:1637–1639, Mar 1961.

[118] F.J. Jelinek, E.D. Hill, and B.C. Gerstein. Initial susceptibility investigation of magnetic transitions in several rare earth metals: Thermal hysteresis in ferromagnetic transitions. *Journal of Physics and Chemistry of Solids*, 26(9):1475 – 1488, 1965.

[119] M. Griffel, R. E. Skochdopole, and F. H. Spedding. Heat capacity of dysprosium from 15 to 300K. *The Journal of Chemical Physics*, 25(1):75–79, 1956.

[120] Lois M. Roberts. The atomic heat of samarium from 2 to 20 K. *Proceedings of the Physical Society. Section B*, 70(4):434, 1957.

[121] L. D. Jennings, Emma D. Hill, and F. H. Spedding. Heat capacity of samarium from 13 to 350K. *The Journal of Chemical Physics*, 31(5):1240–1243, 1959.

[122] M. Rosen. Elastic moduli and ultrasonic attenuation of praseodymium, neodymium, and samarium from 4.2 to 300K. *Phys. Rev.*, 180:540–544, Apr 1969.

[123] B.R. Coles. Transitions from the samarium structure to hexagonal structures. *Journal of the Less Common Metals*, 77(1):153–155, 1981.

[124] N.L. Shi and D. Fort. Preparation of samarium in the double hexagonal close packed form. *Journal of the Less Common Metals*, 113(2):21 – 23, 1985.

[125] F. H. Spedding, A. H. Daane, and K. W. Herrmann. The crystal structures and lattice parameters of high-purity scandium, yttrium and the rare earth metals. *Acta Crystallographica*, 9(7):559–563, 1956.

[126] R. M. Moon, J. W. Cable, and W. C. Koehler. Magnetic structure of neodymium. *Journal of Applied Physics*, 35(3):1041–1042, 1964.

[127] Per-Anker Lindgård. Magnetic distorted spiral structure of Nd at 10 K. *Journal of Physics: Condensed Matter*, 19(28):286202, 2007.

[128] A. C. Anderson, B. Holmström, M. Krusius, and G. R. Pickett. Calorimetric investigation of the hyperfine interactions in metallic Nd, Sm, and Dy. *Phys. Rev.*, 183:546–552, Jul 1969.

[129] R. Ramji Rao and A. Ramanand. Thermal and elastic properties of rare-earth metals. *physica status solidi (b)*, 122(1):11–27, 1984.

[130] D. R. Behrendt, S. Legvold, and F. H. Spedding. Magnetic properties of neodymium single crystals. *Phys. Rev.*, 106:723–725, 1957.

[131] W.B. Pearson, P. Villars, and L.D. Calvert. *Pearson's handbook of crystallographic data for intermetallic phases.* American Society for Metals, 1985.

[132] J. C. Duthie and D. G. Pettifor. Correlation between d-band occupancy and crystal structure in the rare earths. *Phys. Rev. Lett.*, 38:564–567, 1977.

[133] P. Strange, A. Svane, W.M. Temmerman, Z. Szotek, and H. Winters. Understanding the valency of rare earths from first-principles theory. *Nature*, 399:756–758, June 1999.

[134] A. Jayaraman. Fusion curve of europium and fcc-bcc transformation in ytterbium at high pressures. *Phys. Rev.*, 135:A1056–A1059, Aug 1964.

[135] W.B. Holzapfel. Structural systematics of $4f$ and $5f$ elements under pressure. *Journal of Alloys and Compounds*, 223(2):170–173, 1995.

[136] W. Bi, Y. Meng, R. S. Kumar, A. L. Cornelius, W. W. Tipton, R. G. Hennig, Y. Zhang, C. Chen, and J. S. Schilling. Pressure-induced structural transitions in europium to 92 GPa. *Phys. Rev. B*, 83:104106, Mar 2011.

[137] Börje Johansson and Anders Rosengren. Generalized phase diagram for the rare-earth elements: Calculations and correlations of bulk properties. *Phys. Rev. B*, 11:2836–2857, Apr 1975.

[138] W. Bi, N. M. Souza-Neto, D. Haskel, G. Fabbris, E. E. Alp, J. Zhao, R. G. Hennig, M. M. Abd-Elmeguid, Y. Meng, R. W. McCallum, K. Dennis, and J. S. Schilling. Synchrotron X-ray spectroscopy studies of valence and magnetic state in europium metal to extreme pressures. *Phys. Rev. B*, 85:205134, May 2012.

[139] M. Debessai, T. Matsuoka, J. J. Hamlin, J. S. Schilling, and K. Shimizu. Pressure-induced superconducting state of europium metal at low temperatures. *Phys. Rev. Lett.*, 102:197002, May 2009.

[140] N. G. Nereson, C. E. Olsen, and G. P. Arnold. Magnetic structure of europium. *Phys. Rev.*, 135:A176–A180, Jul 1964.

[141] I. Turek, J. Kudrnovský, M. Diviš, P. Franek, G. Bihlmayer, and S. Blügel. First-principles study of the electronic structure and exchange interactions in bcc europium. *Phys. Rev. B*, 68:224431, Dec 2003.

[142] O. Bauder, A. Seiler, S. Ibrahimkutty, D.G. Merkel, B. Krause, R. Rü ffer, T. Baumbach, and S. Stankov. Temperature dependent epitaxial growth regimes of europium on the oxygen-induced c(6×2) reconstructed (110)Nb surface. *Journal of Crystal Growth*, 400:61–66, 2014.

[143] I. Arfaoui, J. Cousty, and C. Guillot. A model of the $NbO_{x\approx 1}$ nanocrystals tiling a Nb(110) surface annealed in UHV. *Surface Science*, 557(1–3):119–128, 2004.

[144] E.E. Latta and M. Ronay. Catalytic oxidation of niobium by rare earths. *Journal of Vacuum Science & Technology A*, 4(3):1626–1630, 1986.

[145] O Hellwig. *Oxidation of Epitaxial Nb(110) Films: Oxygen Dissolution and Oxide Formation*. PhD thesis, Fakultät für Physik und Astronomie an der Ruhr-Universität Bochum, 2000.

[146] Jens Als-Nielsen and Des McMorrow. *Elements of modern X-ray physics*. Wiley, Oxford, 2. edition, 2011.

[147] D. W. Pashley and M. J. Stowell. Electron microscopy and diffraction of twinned structures in evaporated films of gold. *Philosophical Magazine*, 8(94):1605–1632, 1963.

[148] N.G. Szwacki and T. Szwacka. *Basic Elements of Crystallography*. Pan Stanford, 2010.

[149] S. G. Altendorf, A. Efimenko, V. Oliana, H. Kierspel, A. D. Rata, and L. H. Tjeng. Oxygen off-stoichiometry and phase separation in EuO thin films. *Phys. Rev. B*, 84:155442, Oct 2011.

[150] W. Sturhahn. CONUSS and PHOENIX: Evaluation of nuclear resonant scattering data. *Hyperfine Interactions*, 125(1-4):149–172, 2000.

[151] N. M. Souza-Neto, J. Zhao, E. E. Alp, G. Shen, S. V. Sinogeikin, G. Lapertot, and D. Haskel. Reentrant valence transition in EuO at high pressures: Beyond the bond-valence model. *Phys. Rev. Lett.*, 109:026403, Jul 2012.

[152] Michael Y. Hu, Thomas S. Toellner, Nicolas Dauphas, E. Ercan Alp, and Jiyong Zhao. Moments in nuclear resonant inelastic x-ray scattering and their applications. *Phys. Rev. B*, 87:064301, Feb 2013.

[153] N. J. C. Ingle and I. S. Elfimov. Influence of epitaxial strain on the ferromagnetic semiconductor EuO: First-principles calculations. *Phys. Rev. B*, 77:121202, Mar 2008.

[154] Vladimir I. Anisimov, Jan Zaanen, and Ole K. Andersen. Band theory and Mott insulators: Hubbard U instead of Stoner I. *Phys. Rev. B*, 44:943–954, Jul 1991.

[155] G. Güntherodt, P. Wachter, and D.M. Imboden. Energy level scheme and the effect of magnetic order on the optical transitions in europium chalcogenides. *Physik der kondensierten Materie*, 12(4):292–310, 1971.

[156] S. Stankov, Y. Z. Yue, M. Miglierini, B. Sepiol, I. Sergueev, A. I. Chumakov, L. Hu, P. Svec, and R. Rüffer. Vibrational properties of nanograins and interfaces in nanocrystalline materials. *Phys. Rev. Lett.*, 100:235503, Jun 2008.

[157] V.G. Kohn and A.I. Chumakov. DOS: Evaluation of phonon density of states from nuclear resonant inelastic absorption. *Hyperfine Interactions*, 125(1-4):205–221, 2000.

[158] Hans L. Skriver. Crystal structure from one-electron theory. *Phys. Rev. B*, 31:1909–1923, Feb 1985.

[159] P.Piekarz. private communication. 2014.

Acknowledgments

Many people influenced and supported me in many ways and therefore contributed to a great extent to the success of this thesis:

First of all, I am grateful to my professor Tilo Baumbach for his support and for giving me the possibility to perform my work at the institute.

I would like to thank my reviewer, Prof. Wulfhekel for finding time to read and evaluate my work.

I'm very grateful to Dr. S. Stankov who gave me the opportunity to work in his Helmholtz young investigator group 'Nanodynamics'. He was always there ready to share his knowledge and to support the preparations and the measurements. His enthusiasm and experience contribute to a huge extend to the success of all experiments. I was impressed by the calmness and optimism he was able to keep during all possible kinds of catastrophes that are inescapable when working with UHV systems at a synchrotron. I especially thank him for his patience to help me reading this work.

The experimental results acquired in this thesis were compared with calculations done by Dr. Przemyslaw Piekarz. Thank you for such an essential support to my work.

Many thanks to the actual and former members of the *Nanodynamics* group Anja Seiler, Ramu Pardip, Julia Hengster and Shyjumon Ibrahimkutty for the help at the UHV-Laboratory and the discussions. I will always remember the fun we had during preparations and beam times.

I would like to thank all people working at the UHV Laboratoy. Bärbel Krause: I could profit form her experience with the AFM and XPS. Hans Gräfe: For his help with all kind of technical problems with the UHV system and Annette Weißhard: She was always ready to glue new AFM tips (and I needed a lot of them).

Many thanks to Rudolf Rüffer, Aleksandr Chumakov and the beamline staff of the beamline ID 18 at the ESRF for the help during the beam times and the nights you spend at the beamline trying to squeeze out as many photons as possible. It was always a pleasure to work with you.

This thesis would have not been able without the hidden work and support from

whole ANKA/IPS/LAS colleagues and the administration. Thank you!

I would like to thank Venera and Lothar Weinhard who made my work at KIT brighter and helped me through the time when I wrote this thesis.

I am very grateful to my husband Erik Waller who is supporting everything I'm doing and always reminding me about the important things in life.

Meinen Eltern, meinem Bruder und meiner Familie möchte ich für ihren Glauben an mich, ihre Zuversicht und alles was sie für mich getan haben danken.

Erklärung

Hiermit erkläre ich, dass ich die vorliegende Arbeit selbstständig angefertigt und keine anderen als die angegebenen Quellen und Hilfsmittel verwendet habe.

Karlsruhe, 20.01.2014

Olga Waller (geb. Bauder)